Development of Mechanical Technologies for Sensing and Visualizing Deformations in Structures

Zhang, Haihua

(Degree)
博士（工学）

(Date of Degree)
2017-03-25

(Date of Publication)
2019-03-25

(Resource Type)
doctoral thesis

(Report Number)
甲第6914号

(URL)
https://hdl.handle.net/20.500.14094/D1006914

Doctoral Dissertation

Development of Mechanical Technologies for Sensing and Visualizing Deformations in Structures

（構造物の変形をセンシング・可視化するためのメカニカルな手法の開発）

January 2017

Graduate School of Engineering
Kobe University

Haihua ZHANG

ACKNOWLEDGEMENTS

I would like to express my sincere gratitude to my advisor Prof. Akutagawa Shinichi, for his support of my Ph.D. study and research in Kobe University. He has enriched me with his great insight, integrity and determination. I appreciate all his contributions to my research work, including the enlightening ideas, his time and funding. He has provided me with a good example as an excellent scholar during my Ph.D. pursuit

Thanks to the members of On-Site Visualization (OSV) research group for their wonderful collaborations. They are Dr. Izumi Chitoshi, Tsujimura Koji, Aono Yasuhisa, Harano Yuji and Iwata Akihisa. I am grateful for their support to make the sensors, conduct the field experiments and further my research with their constructive suggestions. I would particularly single out Dr. Izumi, who has helped me a lot with my research. I'm grateful for the valuable guidance from his pioneering research work in OSV.

Thanks also to Kondo Katsuhiro, Nakanishi Satomi and Murase Teruhiro from the Department of Civil Engineering of Kobe Univ., for their excellent collaborations and assistance with the laboratory experiments in my research. In addition, I would like to thank Otsuki Masato, Yoshizawa Yasuo, Yoshida Hideki, Nakatsuji Hidenori and Yamato Yuichi, the members of the Machine Shop of Kobe Univ. They were always ready to help me when I needed to make some modification of the sensors by operating the unfamiliar machines.

I thank the past and present members of Akutagawa Laboratory: Terashima Masashi, Tada, Masatoshi, Kido tomohiro, Tamiya shu, Tomiyasu Hitomi, Fujimoto Maki, Yoshiki Tomomichi, Sukihara, Kohei, Murakoshi Ken, Ito Ryosuke, etc. There is a source of friendship and collaboration as well in this group. They make me not feel lonely. I would like to acknowledge Yanagihara kumiko, the secretory of the laboratory, who has been continuously helping me with the research work for the past five years.

My sincere thanks also go to Hashimoto Tadashi, the director of Geo-Research Institute, who has been always willing to help me since I got enrolled in Kobe Univ. He provides me with so many opportunities to know about the advanced technologies in the field of Geotechnical Engineering in Japan. I am so grateful to Prof. Nakai teruo, Dr. Ueda Yasuhiro, Arimoto Hirotake, Dr. Liu Yujian and Dr. Konda Takahiro, for their warmhearted sharing their experiences and skills with me.

My special thanks should belong to Associate Prof. Ma Xianfeng, my advisor when I was a master student in Tongji University, China. He had enlightened me in the first step of research. His recommendation to pursuit a Ph.D. in Japan opened a new window for me to know the world. I am appreciated for his encouragement and support during the tough times in the past few years.

For this thesis, besides my advisor, I would like to thank the other members of examination committee: Prof. Shibuya Satoru and Prof. Morikawa Hidenori, for their helpful comments and valuable suggestions to improve the thesis.

I would also like to thank my parents for all their love, patience and encouragement. They are always there waiting for me. Finally, I want to thank my friends. Their support and encouragement make me keep on going and going.

I can’t have completed my thesis successfully without the help from all of them. Thank you very much!

ZHANG Haihua

Kobe University
January 19, 2017

ABSTRACT

In order to improve the safety management during construction, a new scheme called On-Site Visualization (OSV) is proposed to sense the deformation, inclination etc. of structures and to present the measured results visually in real-time. Two issues have been often raised from construction field that the light-emitting instruments are too expensive, and the professional experiences are required for maintenance of the equipment.

Based on the concept of OSV, the research focusing on development of simple mechanical methods for monitoring the deformation is carried out. The deformations are usually described by the displacements which can be measured directly between two discrete points of the structure. Generally, the basic mechanical rotational system and optical principle are incorporated in the research to transform and magnify the measured displacement. Four representative methods are introduced to monitor the displacement with the accuracy in millimeter-scale, 0.1 mm-scale or much smaller respectively.

Chapter 3 introduces a mechanical method to visualize the relative displacement between two points. Firstly, the displacement is detected by the aramid thread connecting to two measured points. Then, the pulley is mobilized to rotate by the thread which goes throng the groove of pulley. It is a transform from linear displacement to the movement of rotation. There is a triangle flag attached on one side of the pulley so that they would have the identical rotations induced by the displacement. As a result, the displacement can be visualized by rotation of the flag, whose value can be read from the reference scales. The diameter of pulley determines the sensitivity of the monitoring of displacement. The laboratory tests and field experiments show the feasibility of the method to monitor the displacement.

In Chapter 4, an optical method is proposed to visualize small displacement far away from the observed object (remote monitoring). Firstly, the displacement is transformed to the rotational angle by a pinion-rack system. Secondly, the rotational angle can be visualized by the shift of the color stripes reflected from a rectangular mirror. Hence, by establishing the relationship between the displacement and angle, the displacement can be visualized by the images reflected from the mirror. The accuracy of visualization is determined by the pinion-rack system. And the precision of visualization is related to the distance between the mirror and observer (close to reference stripes) and the width of the stripes. The laboratory experiments were carried out to verify the feasibility of this method. The results show that the small displacement can be visualized clearly by this optical method.

Chapter 5 presents a simple method to monitor the thermal deformation, which is different from the load-induced deformation. A thin steel bar is sandwiched between two same beams. One beam is fixed at both ends. The other is fixed at only one end, allowing it to stretch freely. When the environment temperature increases, the elongation of free beam would be larger than that of the beam with two ends fixed. Hence, the thin bar sandwiched between the two beams is mobilized to rotate. The difference of the elongation (thermal deformation) is therefore visualized by the rotation of thin bar. The magnitude of the deformation can be read from the reference scales. The feasibility of this method to monitor the thermal deformation is verified by the laboratory experiments. This method is possible to be applied to monitor the thermal stress of the struts in the foundation pit construction during the summer.

In Chapter 6, a mechanical method is proposed to visualize the direction of principal strain of structures after deformation. It is assumed that a circular ring in the structure is deformed to elliptical under the condition of homogeneous deformation. The major axis of the ellipse indicates the principal strain. The monitoring sensor is made up of an extendable rod and a circular ring. Each end of the rod has a pulley. The ring has the rail track for the pulley to roll on the inner surface. Therefore, the extendable rod is able to rotate along the rail track inside the ring. When the ring is deformed to be an ellipse, the balance of rod is broken so that the rod is mobilized to rotate by unbalanced moment. The rod is able to regain the balance only when it stops at the major axis of the new ellipse after deforming. So the direction of principal strain is visualized by the status of the rod. It can be found that the method is able to sense the regional deformation, different from the conventional measurement of deformation between two points. The mechanism of this method is described in details. And the influence factors are discussed. The uniaxial compression tests were carried out to verify the feasibility of the sensor for visualization of the direction of principal strain. The sensitivity of the sensor was also investigated at the same time. It shows that the sensor can works effectively to visualize the direction of principal strain as expected.

Finally, the conclusions of the thesis are drawn and the future work is introduced briefly.

TABLE OF CONTENTS

LIST OF TABLES

LIST OF FIGURES

CHAPTER 1: INTRODUCTION

1.1 Background

Underground facilities, such as water and sewage transport, oil storage and metro, have developed greatly for decades in many countries, especially in Japan. Underground construction is somewhat different from that on the ground since its geological environment is difficult to investigate and the working condition is changeable often. Deformation monitoring is an indispensable item carried out during construction. As shown in Table 1.1, various kinds of deformation measurements (labelled in gray paint) are included in most of the monitoring plans for underground constructions[1]. It plays an important role for safety management of underground constructions. Firstly, deformation measurements are able to give an intuitive understanding of the performance of structures during construction, in association with other measurements like stress monitoring. Furthermore, the parameters of tunneling using New Austrian Tunneling Method (NATM) are optimized depending largely on the measured results of deformation during the excavation, which relates to total cost of the construction[2,3]. Deformation measurements are also used to examine the results of the theoretical and numerical analysis, which contributes significantly to the improvement of the ability to estimate the external loads and choose proper analytical models.

Table 1.1 Typical items of measurement in underground constructions

Underground constructions	**Typical items of measurement**			
Foundation pit excavation	Axil force of Struts	Deformation of diaphragm wall	Settlement of ground	Groundwater level change
Shield tunneling	Convergence of ring	Movement of joints	Rotations of ring	Soil pressure in the chamber
NATM tunneling	Convergence	Rebound of convert slab	Stress of rock bolts	Stress of steel ribs

Measurement involves two significant aspects. One is to provide the engineers with useful tools for measuring (collecting the information of deformation). The other is to compute the measured data for displaying (disseminating the information). In a common sense, the most measured results are prepared for the engineers or the project managers, who are responsible for assessing the levels of risk during construction. In case of an emergency, if necessary, the alarm would be sent out to the construction workers in the workplace.

Actually the workers are prone to be exposed directly to the potential risks during construction. They are in need of special safety care from equipment to management in order for the accomplishment of construction. Although the advances in measurement technologies for constructions have make the monitoring work easier and more convenient, it is found those instruments are mostly concentrating on collecting and analyzing the information for the technicians. The real-time measurement also focuses on the first aspect as information collection. One limitation is that the workers on the field could not be efficiently informed of the dangerous conditions. In some situations, a delay of just one second in warning could lead to apparently different consequences, particularly, in relation to the lives of the workers. It is necessary to consider the participation of workers in the monitoring work of construction projects. There is a need to have the monitoring instruments sharing the safety information with both the engineers and workers at the construction site.

The cost of measurement is another issue to be considered in practice[4]. It is ideal to complete a high-quality construction project at low cost. The construction managers have to execute the cost control, of course, including the cost of measurement. As for the tunnel construction in particular, because the length of tunnel is much longer than the dimension of its cross section, it is impossible to measure the deformations at all the cross sections along the tunnel. The measured points or locations are usually chosen at the control sections based on the numerical analysis results, and the experts' experience as well. Due to the unusual changes in the geological condition, there might be some under-estimates of the deformations at some cross sections, where deformations should be monitored but ignored at the planning stage of construction. Therefore, it is necessary to develop new monitoring approaches that take care of the difficulties in practice.

1.2 Development of On-Site Visualization

A new monitoring scheme called "On-Site Visualization" (OSV for short) has been proposed by Akutagawa S. in order to improve the levels of measurement during constructions since 2006. It aims to 1) sense the deformation, the inclination, or the strain in structures, and 2) visualize the measured results in real-time as different colors of light or other signs which can be visually identified by the people at the construction sites[5-7]. OSV is supposed to address the presentative issues of measurement raised in the previous section.

As shown in Fig. 1.1, the monitoring procedure of OSV is different from that of

conventional monitoring methods. For conventional monitoring methods, it takes several steps to accomplish a measurement task. Generally, the information like deformation, inclination, temperature, etc. is collected by the sensors set up at the designed points of structures. Then the measured results are processed by the computers (or data loggers) and the final report is analyzed by the professionals. At last, the safety condition of construction would be announced to the workers or engineers at the sites according to the warning levels.

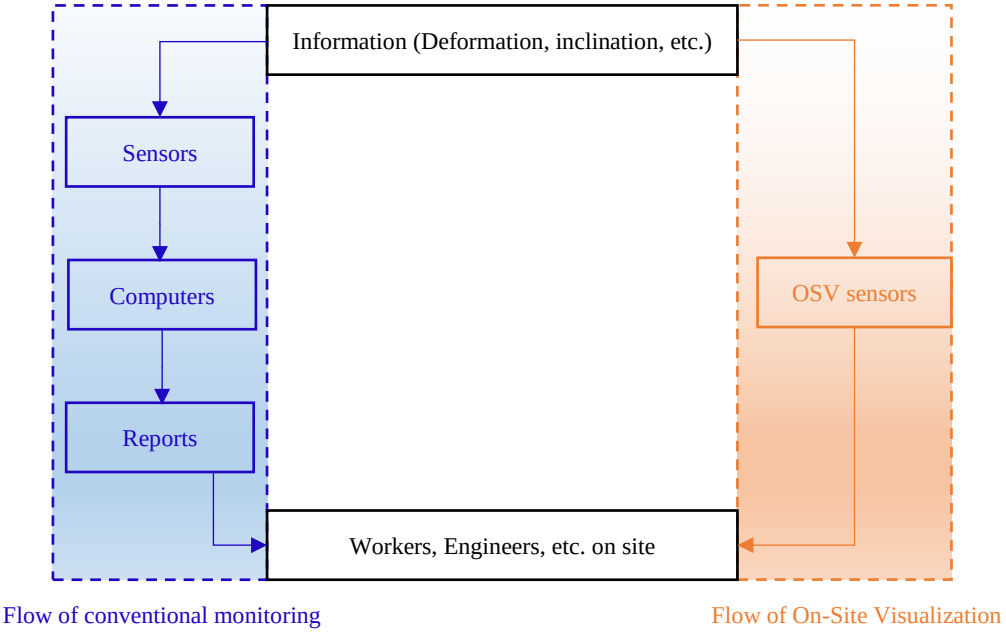

Figure 1.1 Monitoring procedures of conventional measuring methods and OSV

In contrast, the OSV sensors are able to show the indication of measured information in real-time to the workers and engineers directly. The function of data processing and alerting is integrated with the measuring system in the OSV sensors. This is the most significant advantage of OSV which contributes to save the workers' time to escape in reaction to the emergency at the construction sites.

Furthermore, OSV helps to raise the workers' awareness of safety during construction, especially in the developing countries with many untrained workers. The safety training and education activities associated with OSV are usually performed in advance for the workers and engineers. Therefore, the safety management of construction could be improved through the application of OSV sensors and the corresponding safety training for the workers.

After more than 10 years of persistent research and exploration, a series of sensors based on OSV has been developed and applied in the monitoring of construction sites in Japan and abroad. In 2010 On-Site Visualization Consortium was founded in Kobe, including the members from the government, general contractor, company, consultant, research institute, manufactures and so on. In 2015, C. Izumi was the first to be awarded the doctoral degree from Kobe University for his pioneering research in the field of OSV[4]. Generally, the development of OSV can be summarized as 3 phases by far as shown in Fig. 1.2[8].

1.2.1 Phase 1st of OSV

The electric units are widely utilized in the OSV sensors to monitor the structures and the measured results are shown in real-time as different colors of the light from Light Emitting Diodes (LED). For example, the Light Emitting Deformation Sensor (LEDS) is developed to visualize the deformations as different colors of LEDs. The color scheme is defined as follows: dark blue (0~2mm), light blue (2~4mm), green (4~6mm), yellow (6~8mm) and red (8~10mm). Light Emitting Converter (LEC) is designed to convert the electrical signals of normal devices into different colors of light. It is a compact data processor with the function of real-time visualization. The normal measurement devices can be most of electric ones used in the conventional monitoring, such as the strain gauge, the displacement meter, inclinometer, etc. Hence, it is possible to utilize LEC to visualize various items of measurement by just connecting the LEC to the sensors with different functions. Another representative device is the Light Emitting Inclination Sensor (LEIS) which is to visualize the inclination with the accuracy of 0.01 degree.

These sensors had been tested and applied at several construction sites and proved to function well for safety management[4,9]. Meanwhile, the concept of On-Site Visualization got gradually familiar to the civil engineers, construction managers and the civilians as well. Some of them kindly offered pertinent suggestions on the improvement of OSV sensors, which makes the ongoing upgrade in the devices more efficient.

Since the electric units are used as the main components, the cost of OSV sensors is not lower than that of the conventional measuring devices. The issue of cost, which would be a constraint on wider application of OSV sensors, should be dealt with in the following device development.

1.2.2 Phase 2nd of OSV

In the second phase, the analog sensors were developed to measure and visualize the deformations in real-time using plastic optical fibers (POF). When the white light shines on different color filters respectively, the selected color of light is allowed accordingly to pass through, which is used in the OSV sensor as the analogue signal of deformation. The Ground Deformation Sensor (GDS) is designed to visualize the movement of ground by the shift of colors of light, which is transmitted through different color filters. The sheet of color filters, which has the identical movement as the ground, is arranged to pass through the gap between two plastic optical fibers (the propagation medium of light) in alignment. A white light source is set up at one end of optical fiber. Thus the deformation of ground can be visible as different colors of light emitted at the other end of optical fiber. This device is possible to be applied to visualize the ground movement ahead of tunnel face during excavation. Its sensitivity is determined by the width of each color filter.

At the same time, Light State Sensing System (LS^3) is proposed to detect the subtle movement of granular materials like the sand particle[10,11]. It works the similar way like GDS. The key feature lies in the use of plastic optical fiber by transforming the movement into the digital signals of light intensity. Two optical fibers, both with the diameter of 1mm, are used to read the local movement at a point. The first fiber is used to send out the light, and the second fiber is to receive the light reflected by the particles nearby. The reflected light can then be recorded by using the photo diode. If the movement of soil particles happens, the intensity of reflected light would change accordingly.

Since these two methods use the visible light as the key signal transmitter, it makes the measurement immune to the interference of the electric and magnetic fields. Furthermore, because plastic optical fibers can be cut and have great tolerance to bending while transmitting the light, there would be much freedom to perform the measured point instrumentation as needed, regardless of the shape of fiber alignment.

1.2.3 Phase 3rd of OSV

The cost of measurement is always a non-negligible factor when choosing suitable monitoring methods during construction. The electric units are utilized in the OSV sensors during the first phase, which makes the manufacture cost at a high level. Thus the mechanical methods are introduced to visualize the deformation or the inclination in real-time without using electricity. This idea is very interesting but full of challenges. The measurement technologies have evolved greatly from simple to complex over the past few decades. Various devices work based on the simple mechanical structures, which

were invented by our ancestors thousands of years ago, like the wheel. Now we try to review the wisdom of the ancients and hope to get the new inspirations for OSV. This thesis mainly focuses on the development of the mechanical sensors for deformation monitoring based on On-Site Visualization.

Because of the mechanical structures in the design, the cost of manufacture can be controlled at a relatively low level and the maintenance cost is also low. Another feature is that the sensors are able to function without electricity.

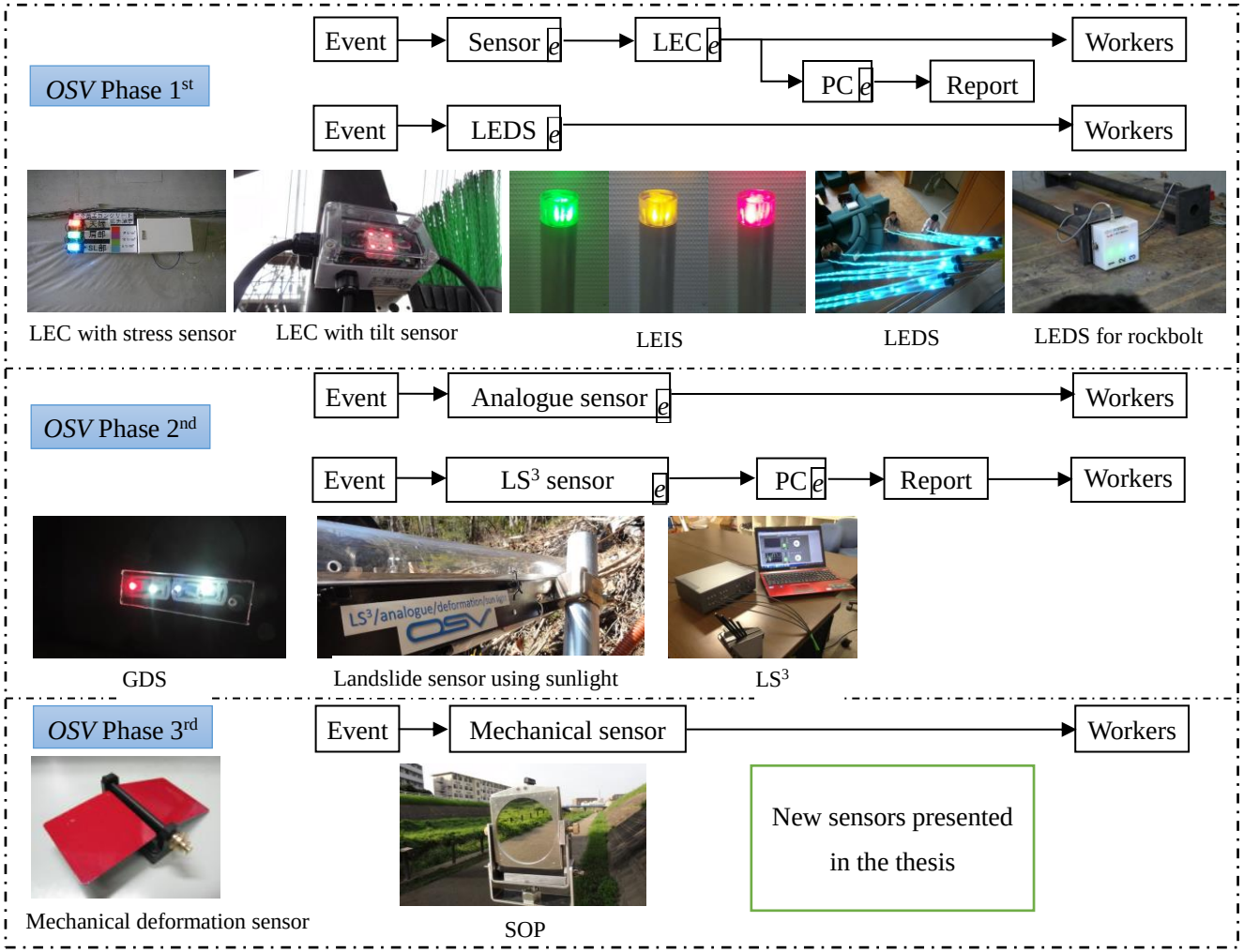

Note:

***LEC**: Light Emitting Converter;*

***LEIS:** Light Emitting Inclination Sensor;*

***LEDS**: Light Emitting Deformation Sensor;*

***GDS:** Ground Deformation Sensor*

***LS³**: Light State Sensing System;*

***SOP**: Single Observation Point;*

***OSV**: On-Site Visualization;*

e: If a device uses electricity, "e" is shown in the box.

Figure 1.2 Development of OSV

1.3 Literature Review

There are various types of measurement techniques concentrating on how to detect the deformations in structures, whereas the devices based on specific On-Site Visualization are rarely to be found. Hence, the representative techniques on the generalized concept of visualization for deformations are introduced to show the state-of-the-art in measurement. The comparison of different methods for deformation measurement is shown in Table 1.2. These methods are suitable for different requirement of measurement in practice.

1.3.1 Taping[12]

A tape measure is the portable device for quantifying the distance between objects with an acceptable accuracy. It might be the oldest and simplest way to use taping in the distance survey or deformation measurement. The distance can be read directly from the tape at the construction sites. Taping, of course, has its limitations to cause errors. The length of the steel tape may vary because of the effect of change in temperature. The steel tape not supported along the entire length would sag in the form of a catenary due to its self-weight. The correction has to be applied on a precise measurement, accounting for all the related error sources. Moreover, since the taping is a manual approach to measurement, the work should be carried out at a certain frequency during construction by the skilled engineers.

1.3.2 Bubble levels

Bubble levels are commonly used to indicate the horizontal level or the inclination induced by deformation. There are basically two types of bubble levels. One is the tubular level, the other is the circular one. The bubble resting in the center, the highest point, shows a perfect horizontal plane where the level is placed. The reading of the bubble indicates to what extent the surface is parallel to the standard horizontal plane (water level). In some senses, it is thought to be a natural visualization of deformation by identifying the bubble's positon.

A plumb bob (weight) is suspended freely from a string and often used as a vertical reference line during construction. It can be also utilized as a simple tool for the visualization of inclination due to deformation.

1.3.3 Total station instruments[12-14]

Total station instruments are widely used to measure the distance and angle in the survey. They are electro-optical instruments, consisting of the electronic distance measuring unit (laser technology) and angle measuring unit (theodolite). The measured data are processed by the internal computer in real-time and displayed on the screen. These data are recorded in the memory at the same time. The deformation measurement can also be performed by total station instruments using the prism reflectors set up on the structures. They are capable of accurate measurement of deformation automatically, thereby providing reliable standard for construction feedback, though the equipment cost is relatively high. Combined with the wireless communication technology, it would be much easier for the engineers to use total station instruments to measure the deformation in structure.

1.3.4 Digital Imaging Correlation[15,16]

Digital Imaging Correlation (DIC) technique is an optical method employed in the full-field deformation measurement. It was proposed originally by Peters and Ranson in the 1980s. By tracking and matching gray intensity between the reference and deformed images of the object, DIC is capable of measure and calculate the overall surface displacement and strain vectors under incremental loadings in a non-contact way. In the recent years, DIC has been improved and optimized greatly by many researchers, with the development of digital camera and computer technology. Now DIC is widely applied in the two-dimensional (2D) and three-dimensional (3D) measurement in a large range size of scale (10^{-9}~10^{2}m), from the inspection of very small cracking strain in mental to deformation measurement of large civil engineering structures.

DIC has several other advantages for measurement, such as simple equipment setup, no need of laser source, high precision, insensitive to rigid motion, applicable in and outside the laboratory, etc. The deformation of the object can be visualized by the colored contour map. Some new DIC systems are developed and tested for real-time deformation measurement, since it usually takes time to carry out the post processing of the images by the conventional DIC. There are some major limitations with DIC for accurate measurement. The performance of DIC depends greatly on the quality of the digital image of structures, which might be affected easily by the light source in the outside environment. The other factors, such as the changes in the structure surface due to weathering, ought to be considered and accessed in the result analysis.

1.3.5 Strain gauges

Electrical strain gauge is a popular and powerful device to measure the strain (minor deformation) at a point under the loading in civil engineering[17]. Its electrical resistance, which can then be measured, varies with the length, thereby providing an accurate measurement of local strain of the object. The electrical signals are processed by personal computer and displayed in the form of graph on the screen. Normally, the cables are necessary to connect the gauges with the data loggers or the computers, which might be not preferred at the construction sites. And it is sometimes possible to cut the cables by mistake by the operating machineries. The temperature effect should be compensated properly for an accurate measurement, particularly in the outdoor environment.

Traditional strain gauge is widely used to monitor the local information of the structure, such as the strain at a point at one direction. On the other hand, the optical fiber is alternatively applied to measurement the strains along the fiber alignment based on Fiber Bragg Grating (FBG) principle[18-19]. A FBG is a periodic modification of the refractive index in the core of optical fiber. The periodic refractive change can reflect a particular wavelength of light, so called the Bragg condition. The reflected light signals change with change in the spacing of periodic gratings, which is caused by the strain or environment temperature.

The strain and wavelength of reflected light can be expressed as:

$$\Delta\lambda_b/\lambda_b = 0.78\varepsilon \tag{1.1}$$

where λ_b is the Bragg wavelength, $\Delta\lambda_b$ is Bragg wavelength shift, and ε is the strain.

FBG strain sensors have many advantages, including low power transmission, high sensitivity, immunity to electromagnetic interference and radiation, etc. The measured data can be analyzed by the computer and displayed on the screen in real-time. Although the cost of the processing equipment is relatively high, FBG sensors are gradually used for strain measurement in the long-term health monitoring of infrastructures and other industries.

Table 1.2 Comparison of different methods for measurement

Methods	Accuracy	Real-time	Cost	Contact	Mechanism	Automatic
Tape extensometers	±0.2mm/10~15m	No	Low	Yes	Mechanical	Manual
Bubble levels	1 °	No	Low	Yes	Mechanical	Manual
Total stations instrument	±2.5mm/100m	Yes	High	Remote	Optical	Automatic
Digital Imaging Correlation	1 pixel	Yes	High	Remote	Optical	Automatic

Electrical strain gauges	5με	Yes	Low	Yes	Electrical	Automatic
FBG strain sensors	20με	Yes	High	Yes	Optical	Automatic

1.4 Objective and Scope

The objective of the present research is to develop mechanical technologies for deformation measurement based on the concept of On-Site Visualization, in order for a better safety management of construction.

To pursue this purpose, the basic types of deformation in structures is investigated so that the requirement of measurement for each kind of deformation is extracted. The representative mechanical structures for measuring deformation are proposed. The mechanical methods are not limited to the literature definition, but to refer to the methods which are free from electricity. Therefore, in this thesis, the mechanical methods include the pure mechanical methods and the optical techniques. The mechanical techniques are capable of a large range of deformation of from the order of centimeters to the strain level. The fundamental experiments were conducted to verify the proposed technologies, which show acceptable performance during measurement and visualization of deformation in structures.

1.5 Thesis Outline

The thesis is organized into 7 chapters. Chapter 2 investigates the fundamentals of deformation and introduces the basic mechanical structures for visualization of different deformation. Chapter 3 proposes a pulley-type method for sensing and visualizing the relative displacement between two arbitrary points in structures. Chapter 4 introduces an optical method for visualization of small relative displacement. Chapter 5 gives a very simple method to monitor the minor deformation caused by such as the change in temperature. Chapters 3 and 4 propose the methods to measure the relative displacement between two points. Chapter 5 introduces a method to visualize the deformation along a length. Further in Chapter 6, a mechanical method is proposed to monitor the deformation within a local area, so that the direction of principal strain is visualized. They are arranged from the displacement measurement between two points, to displacement along a length, to the deformation in a domain. Finally, Chapter 7 summarizes the thesis and provides recommendations for further research. The organization of the thesis is shown in Fig. 1.3.

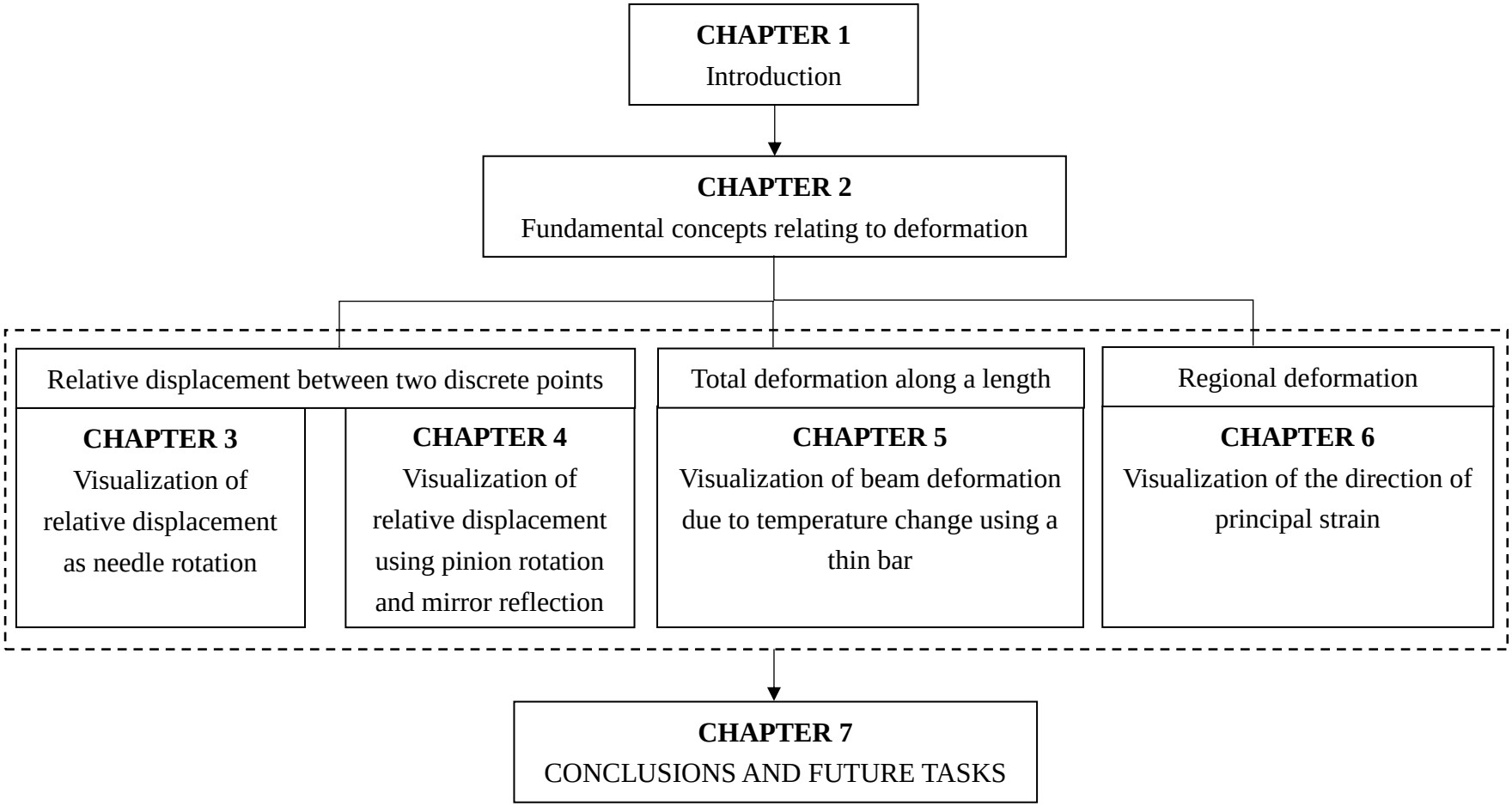

Figure 1.3 Organization of the thesis

Reference of Chapter 1

1. Standard specifications for tunneling -2006: Open cut, *JSCE*, 2006 (In Japanese)
2. Standard specifications for tunneling -2006: New Austrian Tunneling Method, *JSCE*, 2006 (In Japanese)
3. Investigation, design and construction for New Austrian Tunneling Method, *The Japanese Geotechnical society*, 2007
4. Izumi C.: Application and performance evaluation of On-Site Visualization for safety monitoring in overseas project, *Doctoral dissertation*, Kobe University, 2015
5. Akutagawa S.: On Site Visualization as a new paradigm for field measurement in rock engineering, *Proc. of the 6th Asian Rock Mechanics Symposium*, India, New Delhi, pp.34-45, 2010
6. Akutagawa S., Minami Y., Haba T., Hiroshima T. and Nozawa T.: A new method for visualizing stresses in rock support measures by using a light emitting sensor, *Proc. of the 9th ISRM Congress*, China, Beijing, pp.403-407, 2011
7. Akutagawa S., Zhang H., Terashima M. and Tsujimura K.: Measurement and real-time visual presentation of the ground deformation ahead of mountain tunnel face using optical fibers, *Proc. of Sinorock Symposium for the 3rd International Society for Rock Mechanics*, China, Shanghai, pp.759-762, 2013
8. Zhang Haihua, Akutagawa Shinichi, Aono Yasuhisa and Tsujimura Koji: A mechanical method for deformation measurement and visualization in tunnel construction, *Journal of Japan Society of Civil Engineers*, Ser. F1 (Tunnel Engineering), Vol.72, pp.1-12, 2016
9. Izumi C., Akutagawa S. and Son Ho Thanh: Risk management and new technologies in Hanoi Metro Line 2, Proceedings of the international workshop on the risk management in urban underground construction, Hanoi, Vietnam, pp.667-674, 2013
10. Akutagawa S., Nishio A., and Matsumoto Y., Machijima Y.: A new method for reading local deformation of granular material by using light, *Proceedings for the 48th US Rock / Geomechanics Symposium, Minneapolis*, pp.7723, 2014.
11. Akutagawa S., Machijima Y., katayama T.: A new method for interpreting changes in arbitrary engineering quantities by using optical fiber, *9th International Symposium on Field measurements in Geomechanics*, Sydney, Australia, pp.439-452, 2015
12. Wolf Paul R. and Ghilani Charles D.: Elementary surveying: An introduction to Geomatics (10e), *Prentice Hall*, 2002
13. Luo Yanbin, Chen Jianxun, Xi Weizheng, Zhao Pengyu, Qiao Xiong, Deng Xianghui and Liu Qin: Analysis of tunnel displacement accuracy with total station,

Measurement, Vol.83 pp.29–37, 2016

14. Kavvadas M: Monitoring ground deformation in tunnelling: current practice in transportation tunnels, *Eng Geol,* Vol.79(1–2), pp93–113, 2005
15. Peters W., Ranson W., Digital imaging techniques in experimental stress analysis, *Opt. Eng.* Vol.21, pp.427–431, 1982
16. Chu W.F.R.T.C., Sutton M. A., et al.: Applications of digital-image correlation techniques to experimental mechanics, *Exp. Mech.* 25 pp.232–245,1985
17. Vaughan John: Application of *B* & *K* equipment to strain measurements, Brüel & Kjaer, 1975
18. Kersey Alan D., Davis Michael A., Patrick Heather J., LeBlanc Michel and Koo K. P.: Fiber Grating Sensors, *Journal of Lightwave Technology*, Vol.15(8), pp.1442-1463, 1997
19. Hill Kenneth O. and Meltz Gerald: Fiber Bragg Grating technology fundamentals and overview, *Journal of Lightwave Technology*, Vol. 15(8), pp. 1263-1276, 1997

CHAPTER 2: FUNDAMENTAL CONCEPTS RELATING TO DEFORMATION

2.1 Preliminaries

Generally in continuum mechanics, deformation is explained as a change in usual shape or volume subjected to mechanical loading. In order to construct the framework for studying deformation, deformation gradient is introduced to describe the local progressive deformation quantitatively by comparing the difference between the current configuration and the reference configuration. The deformation gradient implies the deformation can be obtained by any combination of rigid body rotation and pure stretch using the polar decomposition[[1,2]].

The body of interest is composed of a set of particles (material point without any mass), which occupy the position in the configuration. It is mainly focused on the geometric change of the body's surface in three dimensional space. Therefore, the actual geometric measurement can be performed on the positon occupied by a particle to evaluate the deformation of a body. The term of displacement (vector) of a point, which relates the deformed configuration to the reference configuration, is often used in the measurement of deformation. The displacement can be explained as the change in positon of the object. Nowadays, Digital Image Correlation (DIC) technique has the ability to describe the overall surface changes in shape of the object (displacement vectors field) in practice[[3]].

Furthermore, the strain is derived from the differential of displacement, as a function of the position (coordinate) of material particle, to explore the constitutive property of the material[[2]]. Strain generally refers to the changes in lengths of lines or the changes in the angle of two intersectional lines[[4]]. The constitutive relation between stress and strain provides a good tool to study the deformation response of material under the loading. Strain can also act as a basic index, so-called critical strain in rock engineering, to assess the failure of the rock material[[5]]. Hence, the allowable deformation values of different kinds of rock are pre-determined according to the critical strains for the safety management of construction.

2.2 Classification of Basic Deformations

The deformations are usually depicted as different forms in civil engineering, such as the deflection of beam, the settlement of ground, the convergence of tunnel, the sliding of slope and so on. They are the results of external forces, such as bending, compression, tension and shear, or other stimuli like heating etc. Basic types of deformation are summarized in two dimensions as follows: rigid body displacement, rigid body rotation, simple shear, pure shear and stretch[6].

2.2.1 Rigid body displacement

Rigid body displacement (translation) is a movement of an object without any change in shape. As shown in Fig.2.1, arbitrary point i(X_i,Y_i) of the object is displaced to i'(x_i,y_i), the displacement $\bar{u}$ is expressed as:

$$\bar{u}_i = \bar{x}_i - \bar{X}_i \tag{2.1}$$

where $\bar{u}_i = [a, b]^T$, $\bar{x}_i = [x_i, y_i]^T$, and $\bar{X}_i = [X_i, Y_i]^T$ are the vectors related to points i and i'.

At the same time, another point j has the displacement $\bar{u}_j$ equal to $\bar{u}_i$. Moreover, the distance between i and j remains the same while the orientation from i to j doesn't change during the motion. We could have deformation gradient $F=I$, I is the 2×2 unit matrix.

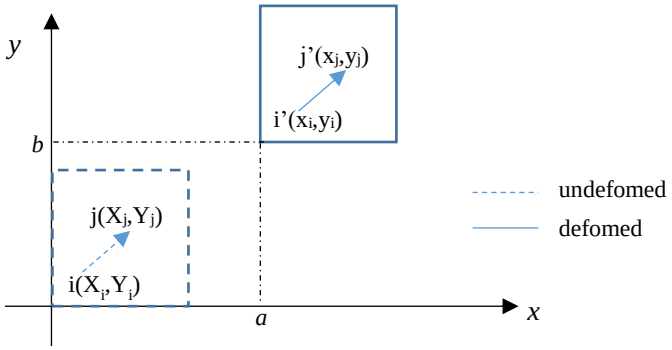

Figure 2.1 Rigid body displacement

2.2.2 Rigid body rotation

Rigid body rotation is another movement of an object without any change in shape. The body rotates about a point (or axis) either in the object or outside the object. Hence, the displacement of any points in the body might differ from each other during this kind of motion. As shown in Fig.2.2, the point i is displaced to point i' by rotation. We will have:

$$\bar{x}_i = R\bar{X}_i \tag{2.2}$$

where $R = \begin{bmatrix} \cos\alpha & -\sin\alpha \\ \sin\alpha & \cos\alpha \end{bmatrix}$ and α is the rotational angle in the counterclockwise direction. In such a case, the deformation gradient F=R.

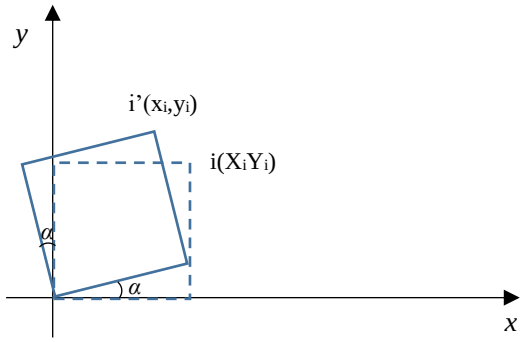

Figure 2.2 Rigid body rotation

Both the rigid body displacement and rotation cause no deformation, thereby having no contribution to the strain of the object. As for rigid body displacement, it is difficult to identify the deformation just by the displacement measurement of a single point. It is better to measure the relative displacements of any two points in the object to figure out whether the deformation of the object occurs. While for rigid body rotation, though most of the points in the object have different displacements, the relative displacement between two points can still be used to analyze the deformation. If the relative displacements between two arbitrary points in the object maintain zero, it shows that there is no deformation of the object. Determination of pairs of measured points in the object in practice should be careful, which might lead to a contrary conclusion of the deformation.

2.2.3 Pure shear (distortion)

The pure shear can be described as the homogenous flattening change in shape but causing no change in volume of the object. As shown in Fig.2.3, the position vector at deformed point i' is expressed as:

$$\bar{x}_i = A\bar{X}_i \tag{2.3}$$

where $A = \begin{bmatrix} 1 & a \\ a & 1 \end{bmatrix}$, a<1. The deformation gradient F=A. In the case of pure shear, the

displacements of the points in the object are not same.

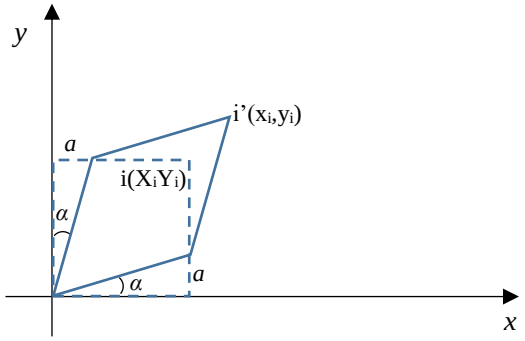

Figure 2.3 Pure shear

2.2.4 Simple shear (with rotation)

Simple shear refers to a deformation with one direction that does not change the length while others rotate relative to it. It can be found that simple shear involves a rotation about a point. As shown in Fig.2.4, the positon vector at the displaced point i' can be expressed as:

$$\bar{x}_i = A\bar{X}_i \tag{2.4}$$

where $A = \begin{bmatrix} 1 & a \\ 0 & 1 \end{bmatrix}$, a<1. The deformation gradient F=A.

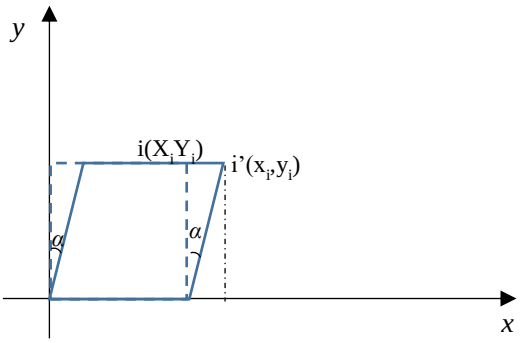

Figure 2.4 Simple shear

The simple shear and pure shear usually exist together during the deformation. It should be noted that the order of the two kinds of shear could give different results of final strain ellipsoid.

2.2.5 Stretch

There are usually two types of stretch: one is stretch with no volume change, the other is the stretch with volume change. As shown in Fig.2.5 (a), the position vector at displaced point i' can be written as:

$$\bar{x}_i = A\bar{X}_i \tag{2.5}$$

where $A = \begin{bmatrix} a & 0 \\ 0 & 1/a \end{bmatrix}$. The deformation gradient *F=A*, while $|A| = 1$. In this case, the pure shear occurs. It is a common kind of deformation in structure due to pure pulling or pushing.

Fig.2.5 (b) shows the stretch (dilation) with volume change. We have:

$$x_i = A'X_i \tag{2.6}$$

where $A' = \begin{bmatrix} a & 0 \\ 0 & b \end{bmatrix}$. The deformation gradient *F=A'*, while $|A'| > 1$ demonstrating a positive change in volume, and $|A'| < 1$ demonstrating a negative change in volume.

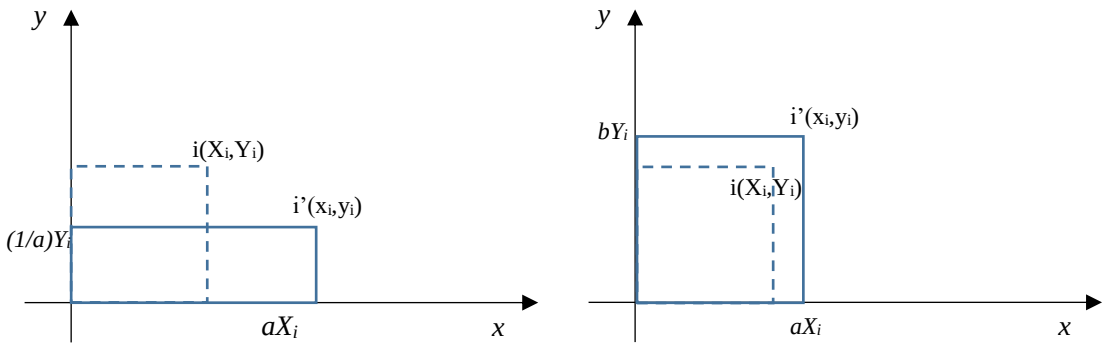

(a) No volume change (b) Volume change

Figure 2.5 Stretch

The deformation usually involves the above five basic types, either a typical one or a combination of some of those. The affiliation relationship of basic types of deformation is summarized in Fig.2.6. It is found that in practice the displacement measurement enables us to describe the deformation quantitatively, in terms of volume change and net rotation.

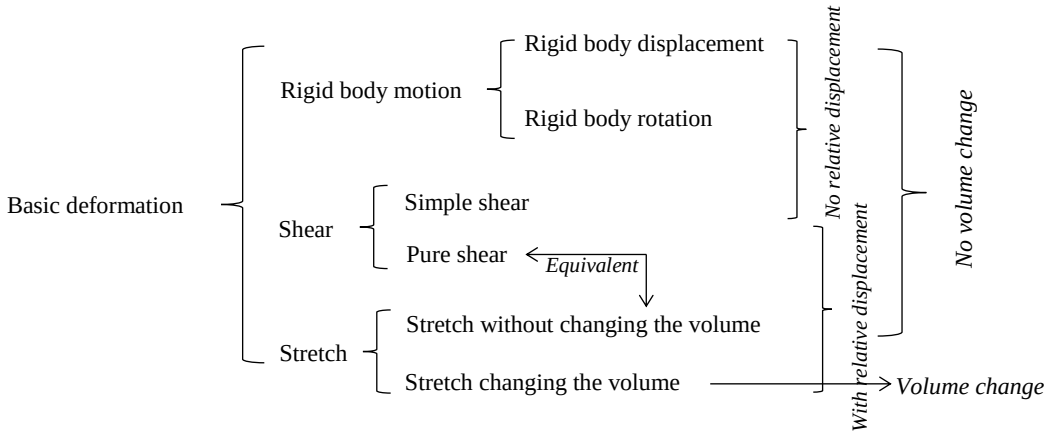

Figure 2.6 Affiliation relationship of the basic types of deformation

2.3 Strain Ellipse

The term of strain enables us to analyze the level of deformation of structure regardless of the size effect. The strain is usually defined as:

$$\varepsilon = \frac{\Delta l}{l_0} = \frac{l - l_0}{l_0} = \frac{l}{l_0} - 1 \tag{2.7}$$

where ε is the strain, l_0 is the initial length of a line, l is the final length of the line, and Δl is the change in length of the line.

Homogeneous strain means the changes in size and shape at every point are identical, which is mathematically preferred in practice. In two dimensions, any homogenous strain can result in (1) originally straight lines remaining straight, and (2) parallel lines remaining parallel[4]. Taking the simple shear for example, it can be illustrated as shown in Fig.2.7. A unit circle (r=1) is set up in the structure before deforming. Any initial point (x, y) on the circle can be rewritten as:

$$x^2 + y^2 = 1^2 \tag{2.8}$$

When the simple shear strain is applied, the new coordinate (x', y') of the point can be rewritten as:

$$x' = x - \gamma y \tag{2.9}$$

$$y' = y \tag{2.10}$$

where γ is the shear strain.

From Eqs. (2.9) and (2.10), we can have:

$$x = x' + \gamma y \tag{2.11}$$

$$y = y' \tag{2.12}$$

Substituting Eqs. (2.11) and (2.12) into Eq. (2.8), we would have:

$$(x' + \gamma y')^2 + y'^2 = 1^2 \tag{2.13}$$

or
$$x'^2 + 2\gamma x'y' + (1 + \gamma^2)y'^2 = 1^2 \tag{2.14}$$

Eq. (2.14) indicates that it is an ellipse after deformation. The symmetric axes of ellipse are inclined to the coordinate axes respectively. As shown in Fig.2.7 (b), the longest and shortest axes of the ellipse are the directions of the principal strains, which are always perpendicular to each other. The magnitude of half of the two major ellipse axes can be expressed respectively as:

$$S_1 = l/l_0 = 1 + \varepsilon_1 \tag{2.15}$$

$$S_3 = l/l_0 = 1 + \varepsilon_3 \tag{2.15}$$

where S_1 is the stretch of the longest major axis of ellipse, S_3 is the stretch (shortening) of the shortest axis of ellipse, ε_1 and ε_3 are two principal strains respectively.

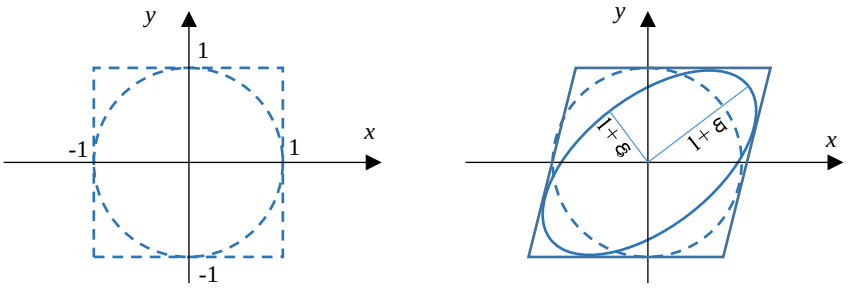

(a) Undeformed (b) Deformed

Figure 2.7 Transformation from a circle to an ellipse under the condition of homogeneous strain

Generally, if the structure is strained homogeneously, the circle would be deformed to be an ellipse. In practice, the structure is not always deformed homogeneously. So the heterogeneously strained body can be divided into several small domains where the strains are homogeneous. Similarly in three dimensions, the unit sphere of strain becomes an ellipsoid under the condition of homogeneous strain.

2.4 Mechanical Methods for Deformation Measurement

A number of basic mechanical structures are easy to be found in the industrial machines or vehicles, which facilitate our daily life greatly. Some of the structures, such as the lever and pulley, have been utilized for thousands of years. We now review the basic mechanical structures and reconsider their possible applications in the field of measurement. Basically the deformations are detected by the relative displacement measurement between two points. The representative structures that have the possibility to be used to sense the deformation are summarized in Table 2.1. They fall into four categories, including direct approach, relay, enlargement and transformation. The mechanical elements of link, circle, wheel and rigid bar etc. are involved in our choices. Among them, (a), (c), (d), (f) and their modifications will be described in detail in the following chapters. The others are introduced briefly in this section.

The feature of the direct approach is how to visualize the measured displacement. The method (b) makes use of the new polymer materials whose color changes according to the body stretch. The polymer is blended with small amount of fluorescent dye by melt processing. The material manifests different color in response of deformation due to the mechanochromic effect of the special dye[7,8]. This is a promising technique for more accurate visualization of the deformation as long as the sensitivity of the emission is improved.

The light path in (e) can be used to measure the displacement remotely, where the object is out of touch. The laser pointer is a good device in a simple visualization of deformation because the coherent light beam can stay narrow within a considerable distance.

The method (g) takes advantage of the incompressible characteristics of liquid. The liquid is filled in the cylindrical container with two sections of different diameters, just like a syringe. When the liquid in the large cylinder is pushed into the small one by the plunger, the movement of the free surface will be larger than that of the plunger, depending on the ratio of the two diameters.

Table 2.1 basic mechanical structures for sensing the deformation

Types	Before	After	Related chapter
Direct approach	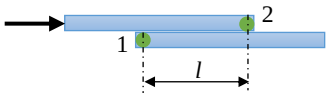 (a) Sliding/ relative movement	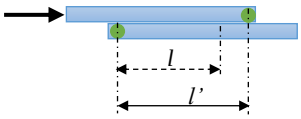	Chapter 5
	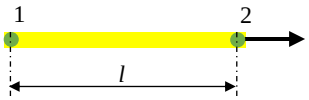 (b) Stretch/expanding with color change	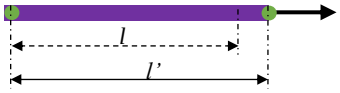	
Relay	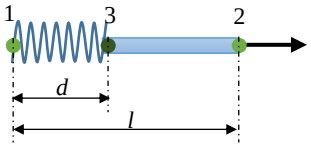 (c) Elongation *Transmit point 3 is introduced.*	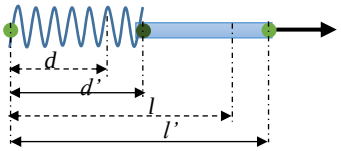 *d'-d=l'-l*	Chapter 6
Transformation	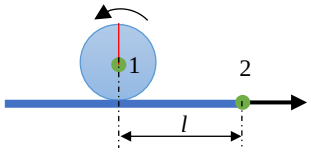 (d) Rotation	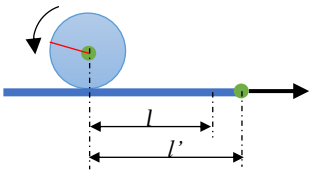	Chapter 3
	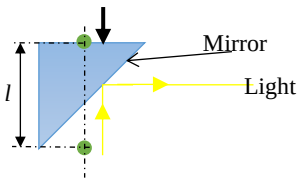 (e) Light path	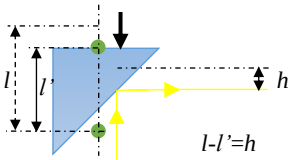 *l-l'=h*	
Amplification	 (f) Scissor/Single lever	 *L'-L=n(l'-l)*	Chapter 4
	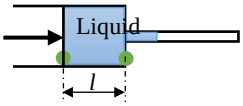 (g) Constant volume	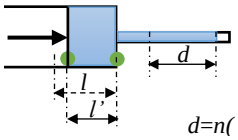 *d=n(l-l')*	

2.5 Accuracy, Precision and Resolution[9,10]

When evaluating the quality of the measurement with a sensor, two terms, accuracy and precision, are often mentioned. Precision is the extent to which the measured values differ from one another. It shows the repeatability of the results of same measurements under an unchangeable condition.

Accuracy is the measure of closeness of measured values to the true value. It should be compared with a standard. The precision of a sensor is affected by the variation of the measurement like random error. The accuracy is affected by the random error as well as the precision.

Resolution is the capacity to distinct the difference clearly in measurement. For an analog measurement, it means the smallest value that can be reliably observed. A sensor can have a high resolution with a poor accuracy because the accuracy is limited to the related calibration standard for measurement. A high quality measurement is obtained on the base of high precision, resolution and accuracy.

2.6 Summaries

The deformation can be decomposed to several basic types. The measurement of displacement is commonly used to identify the deformation though it is not a perfect way. The mechanical structures possible to sense the deformation is discussed briefly. The movement of rotation and sliding are mainly utilized in these structures. The research is carried out by reconsidering these mechanism. The terms for evaluating the quality of measurement with the sensors are clarified. In addition, a standard to determine the reference device for accuracy analysis is introduced. The development of new mechanical technologies is guided by these fundamentals introduced in this chapter.

References for Chapter 2

1. Lai Michael, Krempl Erhard and Rubin David: Introduction to Continuum Mechanics (4e), *Butterworth-Heinemann*, 2009
2. Takashi Kyoya: Continuum mechanics notes, *Morikita Publishing*, 2008 (in Japanese)
3. Pan Bing, Qian Kemao, Xie Huimin and Asundi Anand: Two-dimensional digital image correlation for in-plane displacement and strain measurement: a review, *Meas. Sci. Technol*, Vol.20 pp.1-17, 2009
4. Ramsay John G. and Huber Martin I.: The techniques of modern structural geology, Volume 1: Strian analysis, *Academic Press, Inc.*, 1983
5. Sakurai Shunsuke,: An evaluation technique of displacement measurements in tunnels, *Journals of JSCE*, Vol. 317, pp93-100, 1982
6. Price Neville J. and Cosgrove John W.: Analysis of Geological Structures, *Cambridge University Press*, 1990
7. Lavrenova A., Holtz A., Simon Y. C. and Weder C.: Deformation-Induced Color Changes in Melt-Processed Polyamide 12 Blends, Macromolecular Materials and Engineering 2016, 301 (5), 549–554.
8. Crenshaw Brent R., Burnworth Mark, Khariwala Devang, Hiltner Anne, Mather Patrick T., Simha Robert and Weder Christoph: Deformation-Induced Color Changes in Mechanochromic Polyethylene Blends, *Macromolecules*, Vol.40 (7), pp.2400-2408, 2007
9. Steigenberger Peter, Seitz Manuela, Bockmann Sarah, Tesmer Volker, Hugentobler Urs: Precision and accuracy of GPS-derived station displacements, *Physics and Chemistry of the Earth* Vol.53-54, pp.72–79, 2012
10. Source: http://www.firsttenangstroms.com/faq/Resolution.html (Oct., 2016)
11. Yamaguchi Toru, Eguchi Tyutomi, Osamuta Teruo and Ibayashi Hiroshi: Introduction to the measurement techniques for the technicians on the field, *Japanese Standards Association*, 2008 (in Japanese)

CHAPTER 3: VISUALIZATION OF RELATIVE DISPLACEMENT AS NEEDLE ROTATION

3.1 Preliminaries

In order to describe deformation, people often resort to the displacement. Two issues are raised in the measurement of displacement, including (1) how to sense it and (2) how to represent the measured data. Since the contact measurement of displacement between two points is reliable, the representation of measured result has been a matter of topic concern in this research. So far, different colors of light from LEDs are mainly used in the sensors developed to visualize many kinds of changes[1]. The electric devices for measurement are getting more and more advanced by taking in the new sensing technologies. The weak point lies in that they can generally work depending on the electricity or battery. Therefore, it is necessary to devise new technologies to visualize the displacement in a mechanical way. The mechanical structures investigated in the previous chapter are possible to fulfill the purpose. Some of those structures are selected to visualize the displacements with different accuracy required for measurement. This chapter will present the first trial to visualize the displacement at the millimeter level by the movement of rotation[2].

3.2 Description of The Method

The first deformation sensor is a device which is able to measure the relative displacement between two arbitrary points and show the result by the rotation of the indicator simultaneously on site. As shown in Fig. 3.1, it consists of two main components. The first component is the thread with high stiffness in tension and good flexibility in bend that can mobilize a pulley to rotate when a relative displacement occurs between the two points connected by the thread. The pulley is to translate the linear displacement into the rotation, and its diameter determines the sensitivity of the measurement with respect to the displacement. The details of the pulley are shown in Fig. 3.2. The second component is the indicator, here represented as the needle, which is attached on the side of the pulley for visualization of the measured displacement. The length of the needle is 150mm. The tension of the thread rotating around the pulley is provided by the weight or spring. A plastic board with gradation is positioned behind the indicator so that the value of

displacement can be read directly (Fig. 3.3). The board is subdivided into colored sectors according to necessary safety levels.

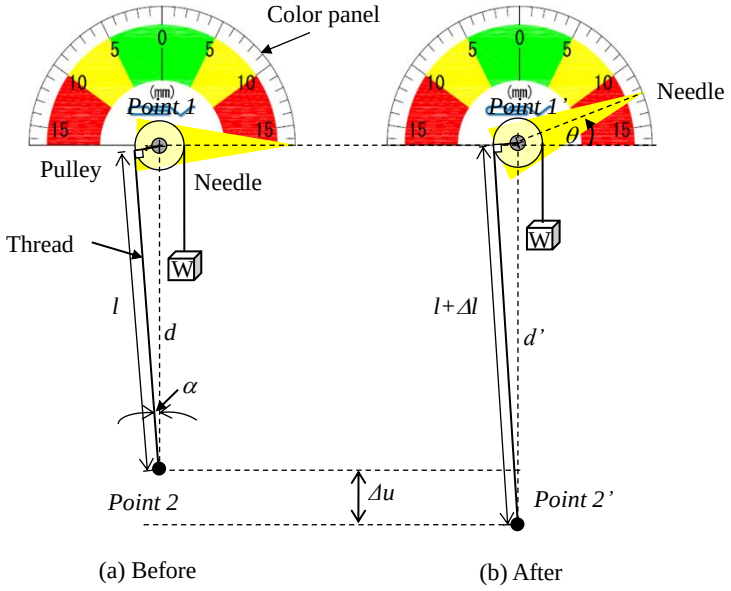

Figure 3.1 Layout of the deformation sensor

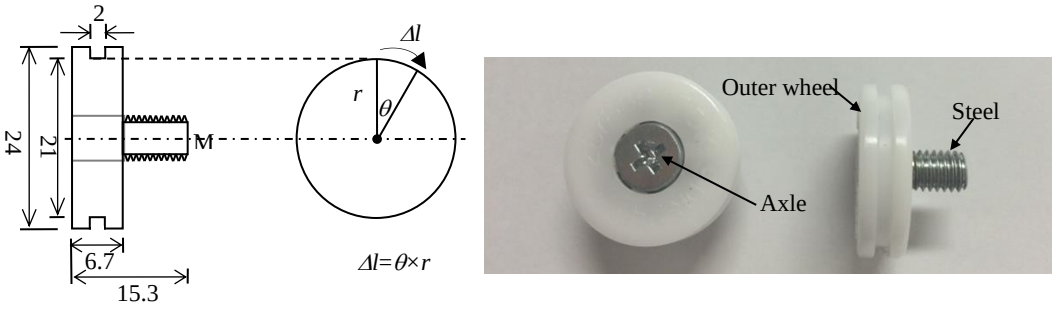

(a)Size of pulley (unit: mm) (b)Photo of pulley

Figure 3.2 Details of the pulley

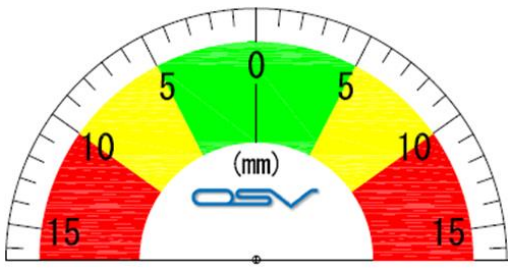

Figure 3.3 Example of the plastic color board

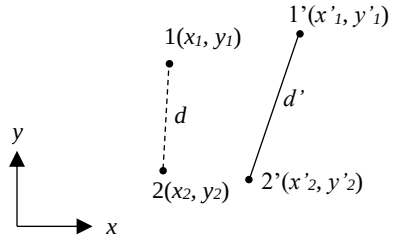

Figure 3.4 Relative displacement between two points

As shown in Fig. 3.4, given two points 1(x_1, y_1) and 2(x_2, y_2), the distance (*d*) between points 1 and 2 can be expressed as:

$$d = \sqrt{(x_1 - x_2)^2 + (y_1 - y_2)^2} \tag{3.1}$$

After deforming, the new coordinates of the two points become 1'(x_1', y_1') and 2'(x_2', y_2') respectively. And the distance *d'* between the two points is given by:

$$d' = \sqrt{(x_1' - x_2')^2 + (y_1' - y_2')^2}. \tag{3.2}$$

Therefore, the relative displacement *Δu* between the two points can be given by:

$$\Delta u = d' - d. \tag{3.3}$$

Paralleling Line (*1'2'*) with Line(*12*) by rotating Line(*1'2'*) as shown in Fig.3.1, the relative distance *Δu* will be the same. Whatever state of Line(*1'2'*) is due to the structure deformation, this kind of parallel translation always works. In order to measure the movement of points 1 and 2, the pulley of the sensor is set up at point 1 which can be regarded as the unmovable. Whichever one is chosen as the unmovable point is up to the users. The thread goes around the circumference of the pulley, with one end connected to point 2 and the other end connected to a weight. In Fig.3.1 point 2 moves along the line parallel with Line (*12*). The relationship between the relative displacement *Δu* and the arc length *Δl* of rotation of pulley is derived as follows:

$$l^2 + r^2 = d^2 \tag{3.4a}$$

$$(l + \Delta l)^2 + r^2 = (d + u)^2 \tag{3.4b}$$

Eliminate *r* from Equations (3.4a) and (3.4b) to obtain a new Equation (3.4c):

$$u^2 + 2du - (\Delta l^2 + 2\Delta l \cdot l) = 0 \tag{3.4c}$$

solve for *u* in Equation (1c):

$$u = \sqrt{\Delta l^2 + 2\Delta l \cdot l + d^2} - d \tag{3.4d}$$

since:

$$l = d \cdot cos\ \alpha \tag{3.4e}$$

then:

$$u = \sqrt{\Delta l^2 + 2\Delta l \cdot d \cdot \cos\alpha + d^2} - d \tag{3.4f}$$

as α gets close to 1, we will have:

$$\cos\alpha \approx 1 \tag{3.4g}$$

whence:

$$u \approx \sqrt{\Delta l^2 + 2\Delta l \cdot d + d^2} - d \tag{3.4h}$$

finally:

$$u \approx \Delta l \tag{3.4i}$$

where *Δu* is the relative displacement between two points, *d* is the distance between two points, *r* is the radius of pulley, *l* is the length of the tangent line, *Δl* is the arc length of rotation of pulley, α is the intersection angle between the tangent line of thread and the line that goes through points 1 and 2.

The results of theoretical error analysis with respect to different distance *d* between two points are shown in Fig. 3.5. The relative error ratio is expressed as:

$$Relative\ error\ ratio = \frac{\Delta l - \Delta u}{\Delta u} \times 100\% \tag{3.5}$$

where *Δu* represents the actual displacement between two points, *Δl* represents the measured displacement by the mechanical sensor in Fig. 3.1.

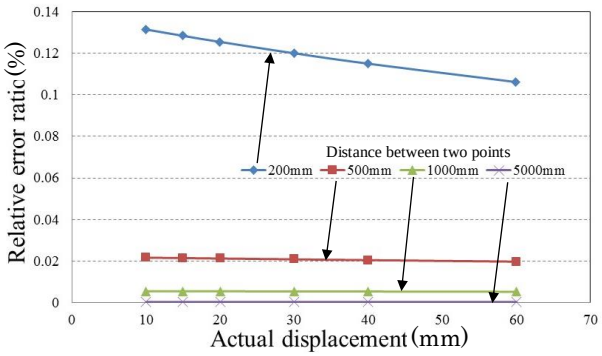

Figure 3.5 Error analysis

It can be figured out that the longer the distance between two points is (α close to 0), the more accurate the measured result is. Even in case of the distance of 200mm between two points, the relative error ratio is less than 0.14%. In addition, the relative error ratio decreases as the relative displacement between two points increases. All the approximate relationship between the actual displacement and the measured value between two points is based on the assumption of infinitesimal of angle α. Therefore, the measured displacement by the sensor can be accepted as the actual displacement between two points.

The deformation of structure is measured and visualized by the rotation of the indicator (or needle). From experience, the movement ω of tip of the indicator as small as 2mm can be well identified by eyesight[3]. The relationship of measured displacement Δu, radius of pulley r, rotation angle θ, ω and length of needle s can be expressed as:

$$\Delta u = r \times \theta = r \times (\omega / s) \tag{3.6}$$

It shows that smaller "r", larger "s" can result in higher measurement accuracy. In this research, we have r=10.5mm, ω=2mm and s=150mm, so, Δu =0.14mm. It means that a relative displacement of 0.14mm can be visualized by this method theoretically.

It should be noted in Fig. 3.4 that structure deformation may happen while the relative displacement Δu between the two points remains zero. In this case, the deformation cannot be visualized by this sensor.

3.3 Fundamental Experiments

3.3.1 Material of components

The sensor is made up of the components which can be found easily in the market. The reliability of the sensor depends largely on the property of the material of its components. A plastic pulley with a diameter of 21mm (Fig. 3.2) is adopted in this research. Its axle is made of steel. And the outer wheel of the pulley is made of polyoxymethylene which is an engineering material used in precision parts requiring high stiffness and excellent dimensional stability. The property of polyoxymethylene is shown in Table 3.1. It could be thought the influence of deformation of pulley would be negligible during the experiment in this research. The very important component is the thread which connects the two measuring points. The thread requires very high stiffness that ensures a complete displacement translation between two points.

Table 3.1 Property of polyoxymethylene[4]

Parameters	Density [g/cm^3]	Compressive strength [MPa]	Young's modulus [MPa]
Values	1.420	31	3500

The aramid fiber is chosen as the thread. As shown in Table 3.2, the aramid thread is the product which is light weight, has high strength, high modulus, and good chemical and thermal stability.

Table 3.2 Property of the aramid thread used in the test[5]

Parameters	Diameter	Density	Elastic modulus	Extensibility	Coefficient of thermal expansion(<150℃)
	[mm]	[g/cm^3]	[MPa]	[%]	[cm/cm/°C]
Values	0.69	1.44	70500	4.8	4.0×10^{-6}

3.3.2 A tensile test

The laboratory test is performed to determine the creep feature and the tensile ratio of the aramid thread under different weight loads (9.8N and 19.6N) as shown in Fig. 3.6. The tensile load is applied to the aramid thread at one end while the other end is fixed from a solid point at the steel block. The elongation of the aramid thread is recorded against the applied load at an interval of about 24 hours. This experiment was terminated in five days when there was no apparent change in length of the thread any more.

As shown in Fig. 3.7, the aramid threads exhibit different extension characteristics with respect to the applied loads during the first three days. After that, the elongation of the thread is too small to be sensed, which allows us to deem that the aramid thread is in a stable state. Table 3.3 shows the results of the tensile test. The extensibility of the aramid thread increases as the load increases. The maximum extensibility is 0.079% under the load of 19.6N while it is 0.048% under the load of 9.8N.

In case of monitoring of concrete crack, if two points within a distance of less than 500mm are connected by the aramid thread under the load of less than 4.9N, the elongation of the thread would be less than 0.15mm (calculation based on linear relationship with the load of 9.8N), which is hard to be identified by human eye. For the measurement of convergence displacement in a tunnel, the length of the thread is so large (e.g., 8,000mm) that the elongation of aramid thread due to applied weight should be taken account of in the error analysis.

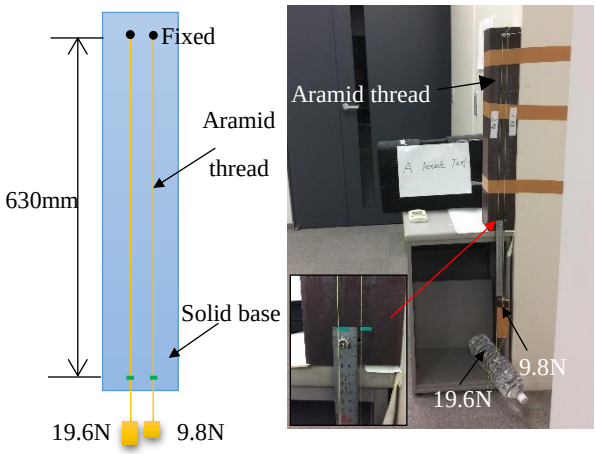

(a) Sketch of the test (b) Photo of the test

Figure 3.6 Layout of the tensile test in the laboratory

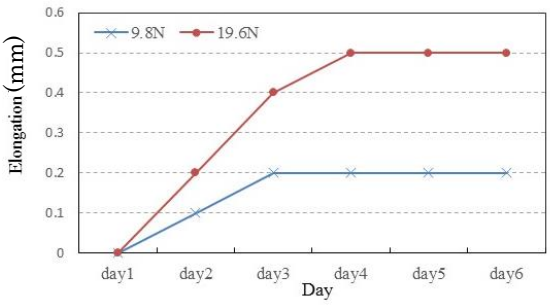

Figure 3.7 Elongation of the aramid thread against time

Table 3.3 Results of the tensile test

Parameters	Case1	Case2
Weight [N]	9.8	19.6
Temperature [°C]	23.6~24.3	
Moisture [%]	46~65	
Period of time [day]	5	
Length [mm]	630	630
Stretch [mm]	0.2	0.5
Extensibility	0.048%	0.079%

3.3.3 Critical force tests

In order to minimize the extensibility effect of the aramid thread, it is better to keep its tension smaller. On the other hand, at tunnel construction site, some unexpected contact with the needle or thread may happen to mobilize the pulley to rotate with a slip relative to the thread, making the measured results incorrect. Therefore, the critical force is proposed to determine the proper load, which ensures there is no sliding between the thread and the pulley. The critical force is defined as the force equal to the maximum static frictional force around the circumference of the pulley as shown in Fig. 3.8. In another word, if the unintended external force is less than the critical force, the rotation of pulley mobilized by the thread without sliding can be ensured.

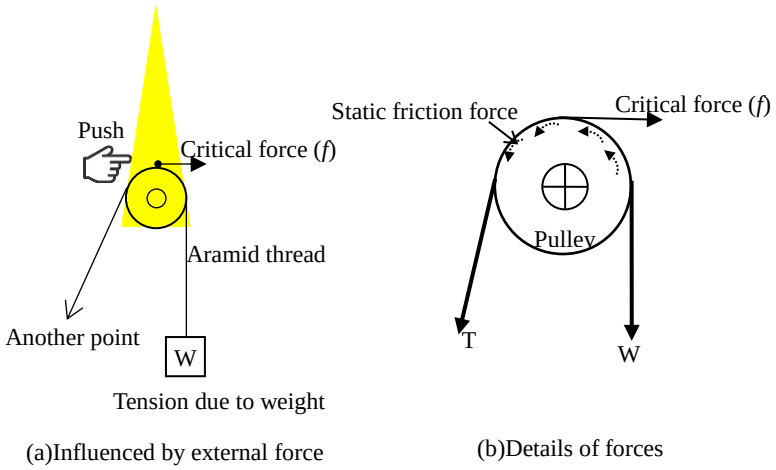

Figure 3.8 Critical force between pulley and thread

A critical force test is carried out under 3 different loads (4.9N, 9.8N and 19.6N) as shown in Fig. 3.9 and Table 3.4. It is similar to the tensile test. The sensor is fixed at a solid point

on the wall that does not move. The aramid thread is set up along the groove of the pulley, within one end fixed from another solid point on the wall. The other end of the thread is loaded by the designated weight. The result of relationship between applied load and critical force is shown in Fig. 3.10. It can be found that the critical force increases in accordance with the increasing weight load. For example, in this experiment, in the case of the load of 4.9N, an equivalent external force of less than 0.5N would not affect the results. Based on this test, a proper weight ought to be decided to provide suitable tension of the thread, of course, not having effect on the deformation of the structure, in the field measurement.

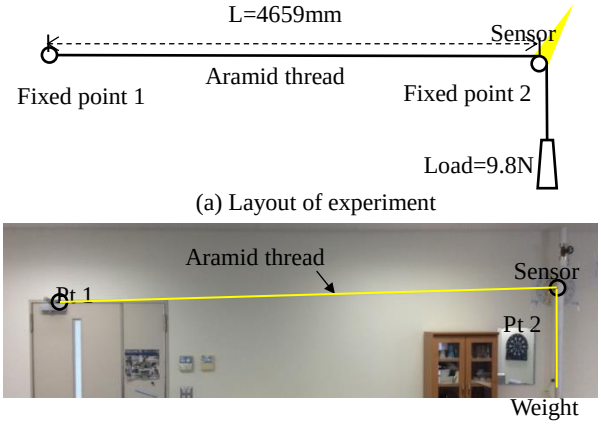

(a) Layout of experiment

(b) Photo

Figure 3.9 The critical force test in the laboratory (Case 5)

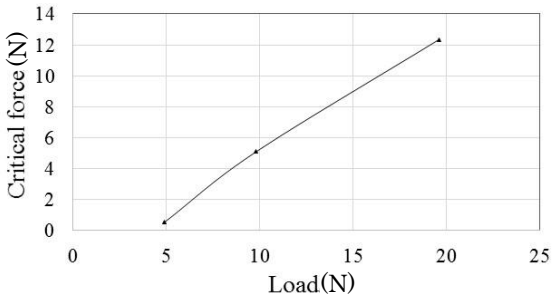

Figure 3.10 Relationship between critical force and load

Table 3.4 Information of critical friction tests

Parameters	Case4	Case5	Case6
Weight [N]	4.9	9.8	19.6
Temperature [°C]	19.6~22.6		
Moisture [%]	33~46		

3.3.4 Analysis of other influence factors

There are some other factors such as the temperature, the wind, the sunlight and the moisture to be in considerations which could influence the measured results of relative displacement during monitoring. The aramid thread in this research has a very small coefficient of thermal expansion under 150°C as shown in Table 3.2, which allows that the effect of temperature change in the tunnel can be negligible. However, this kind of aramid thread is not recommended to be exposed directly in the sunlight or in the environment with high moisture content, where the strength of the thread decreases over time. A further experiment on the influence due to the moisture and sunlight should be carried out in the next study. Nevertheless, by taking some proper protection measures, the sensor is possible to provide a reliable result of the displacement to meet the requirement of monitoring.

It can be conclude that the accuracy of visualization by this method is determined by the sensing part, including the pulley and the connecting thread. Besides, the precision of visualization by this method is related to the resolution of the plastic color board.

3.4 Field Experiments

3.4.1 Project overview

The Hachinoshiri Tunnel is located in the Pref. Yamanashi which is an important part of the Chubu Odan Expressway in Japan. As shown in Fig. 3.11, the tunnel project with the length of 2469m and the typical excavated cross section area of 82m^2 was conducted by New Austrian Tunneling Method (NATM) through various geologies, including the weak ground such as the mudstone. In the weak stratum, some new excavation approaches such as the curved tunnel face and early invert installing methods were adopted to improve the tunneling stability during excavation[6]. However, when the tunnel was excavated through the mudstone stratum, excessive deformations of the linings of the tunnel were encountered with, which made the construction delayed for several months. The results of convergence measurement by Total Station showed a relative displacement in horizontal line increased to 15mm in 24 hours after the prism was set up at one measuring section, and 200 days later its maximum value became 674mm[7]. The mudstone is so weak that its strength ratio (uniaxial compression strength /weight of overburden) is less than 1.1 (Table 3.5). The cracks of the shotcrete could be often seen physically at the sidewall section along the finished tunnel (Fig. 3.12). Although the measurement of deformation had been carried out by Total Station every10m along the tunnel (Fig. 3.13),

it was necessary to enhance the monitoring of tunnel during excavation, especially for the deformation cracks of shotcrete associated likely with the interaction of tunnel and weak ground, in the intervals where not monitored before.

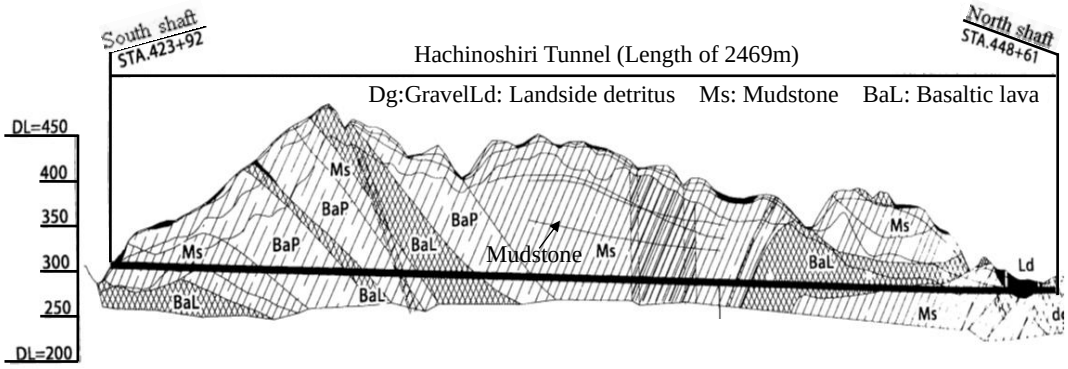

Figure 3.11 Geological profile of Hachinoshiri Tunnel

Figure 3.12 Cracking of the shotcrete

Table 3.5 Geological parameter of the mudstone

Rock type	Unit weight [KN/m^3]	Strength ratio –	Uniaxial strength [×10^{6}N/m^2]
Mudstone	21.6	0.5~1.1	0.26

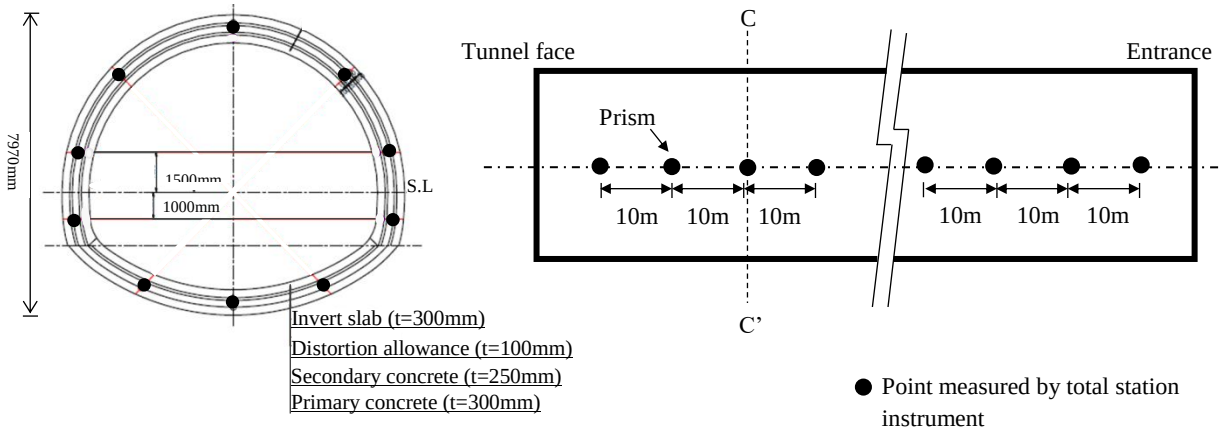

(a)Measured point in the sectional view of tunnel (CC') (b)Measured points by Total Station in longitudinal direction

Figure 3.13 Conventional measurement of tunnel by Total Station (Sectional)

3.4.2 Monitoring instrumentation

The deformation sensors were employed to monitor the tunnel where the conventional measurements were not carried out in the original measurement plan. The measuring points were determined by the veteran engineers. There are no specific rules to decide the interval of the sensors or the number of the sensors. The deformation sensors were set up as early as possible when the state of structure needed to be under additional monitoring. Moreover, the sensors should be set up in avoidance of the touch with the heavy machinery in the tunnel. The monitoring of tunnel structure using the deformation sensors is classified into two categories as follows:

(a) Routine monitoring

As shown in Fig. 3.14, although the tunnel face had passed away from interval *A*, some deformations of tunnel structure were found still ongoing. In order to investigate the state of tunnel structure, the cracks of the lining were monitored by the deformation sensor (Fig. 3.15). And the deformations between the invert and the sidewall of the tunnel were also measured (Fig. 3.16).

At interval *B* with a length of 100m behind the tunnel face, the changes in length of the arch section were monitored in real-time by the deformation sensors as show in Fig. 3.17, so that the instant deformation after tunneling could be known as early as possible.

Fig. 3.18 shows the details of the installation of deformation sensor on the surface of shotcrete. The pulley with the indicator is fixed at the shotcrete by the bolts. As shown in Fig. 3.15, the pulley is set up at point 2. The aramid thread goes along the groove of the pulley, with one end fixed at point 1 and another end fixed by a steel nut (about 0.98N) or 500ml pet bottle (about 4.9N in Fig. 3.17).

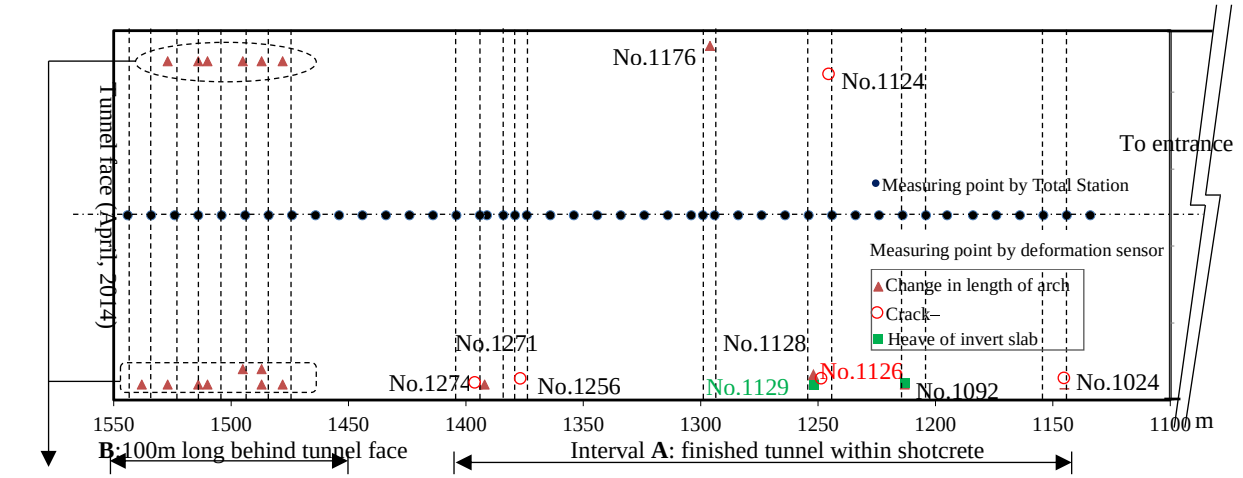

Note: The numbers in the upper box from left are No.1407R, No.1394R, No.1390R, No.1375R, No.1367R, No.1357R
The numbers in the lower box from left are No.1418, No.1407L, No.1394L, No.1375L, No.1367L, No.1367W, No.1357L

Figure 3.14 Measuring points by deformation sensor and Total Station respectively along the tunnel (plane view)

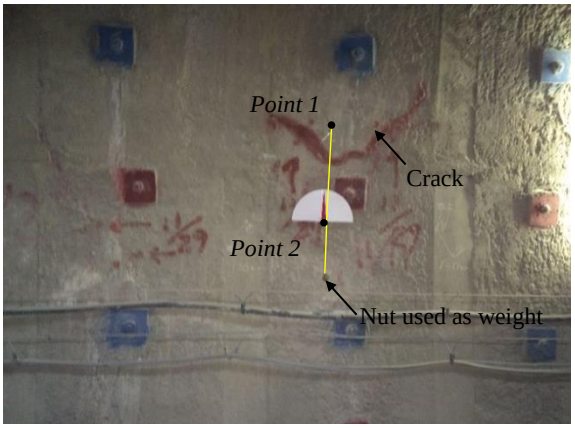

Figure 3.15 Crack monitoring (No.1124)

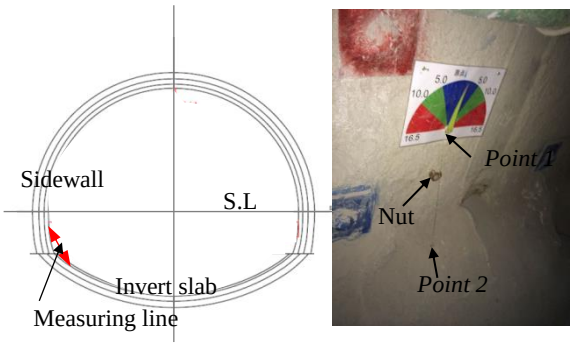

Figure 3.16 Displacement between the invert and the sidewall (No.1129)

Figure 3.17 Monitoring of the change in length of the arch section (No.1375R)

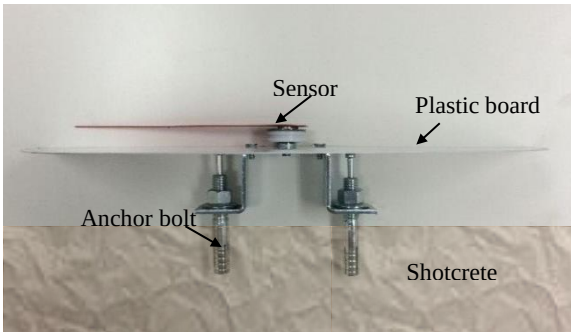

Figure 3.18 Example of installation of deformation sensor

(b) Monitoring during break

There was a one-week break of the excavation during the New Year Festival. It was of importance to know the deformation of the tunnel near the tunnel face before the new

excavation continued. Therefore, the convergence of the tunnel 1m away from the tunnel face was monitored by measuring the vertical and horizontal displacement respectively, which was not usually done during excavation as shown in Fig. 3.19.

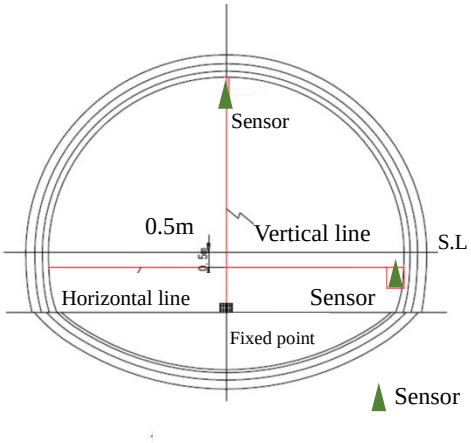

Figure 3.19 Convergence monitoring according to vertical and horizontal displacement (1m behind tunnel face)

3.4.3 Result analysis

(a) Routine monitoring

Fig. 3.20 shows some representative records of the relative displacements measured by the mechanical sensors, including the deformation of cracks, the relative displacement between the sidewall and the invert slab (heaving), and the change in length of arch section of tunnel. Because the details of most measuring points (for example the distance between two points, weight of each nut) were not recorded clearly during the monitoring, it is difficult to modify every value of the relative displacement due to the elongation of the aramid thread. Although the raw data are used in the paragraph, the trend of the changes of displacements would not be affected. It shows that the deformations of tunnel developed rapidly as the monitoring started. About two months later, the displacements became almost unchanged, which indicated the tunnel was in a stable condition.

Fig. 3.21 shows a comparison between the displacements measured by Total Station and the mechanical deformation sensor. The heave of the invert slab was monitored by the mechanical sensor (No.1092). The convergence measurement of the tunnel by Total Station was conducted at the cross section 1m away from the mechanical sensor (No.1092). Although the measuring objects were different, the displacements measured

by these two methods show the same trend, which could present an overall image of the deformation process of the tunnel during construction.

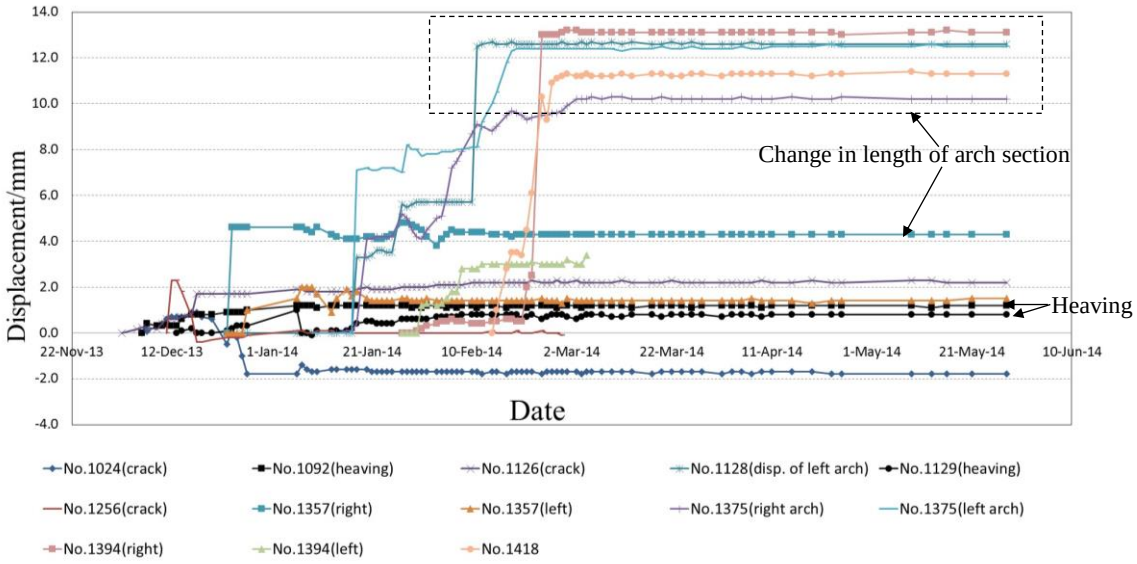

Figure 3.20 Results of the displacement measured by the mechanical sensors

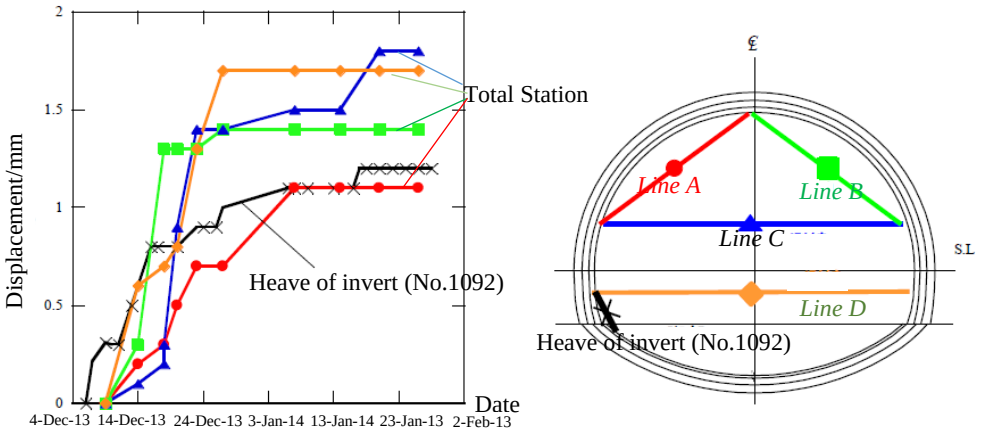

Figure 3.21 Comparison between the displacements measured by Total Station (TD1214) and mechanical deformation sensor (No.1092)

Thus, it is very important to monitor the deformation of the lining during the initial stage of the construction when the deformations develop very rapidly. If an excessive displacement is detected as early as possible, the risk of the tunneling shall be reduced by

taking proper countermeasures.

(b) Monitoring during break

For the monitoring during the New Year Festival, the rotation of needle can be well observed with the naked eyes as shown in Fig. 3.22. Therefore, the convergence displacement by which the stability of the tunnel is evaluated is able to be easily obtained. Table 3.6 presents the results of displacement measurement of convergence. The measured displacements are modified considering the elongation of aramid thread. Take the measurement of horizontal line for example, its length is 12.5m, the weight of load (pet bottle filled with water) is 4.9N, the extensibility is 0.031% (simplified linear relationship based on Table 3.3, so the elongation of the aramid thread would be 3.8mm (12.5×0.031%×1000), thus, the revised displacement of horizontal line is 14.9mm (18.7mm-3.8mm). Based on the visualized deformation, the engineers and workers were able to evaluate the safety level easily as early as possible during tunneling construction.

Table 3.6 Results of convergence measurement

Date	Vertical [mm]		Horizontal [mm]	
28th Dec., 2013	0		0	
6th Jan., 2014	Measured	Modified	Measured	Modified
	12.1	9.7	18.7	14.9

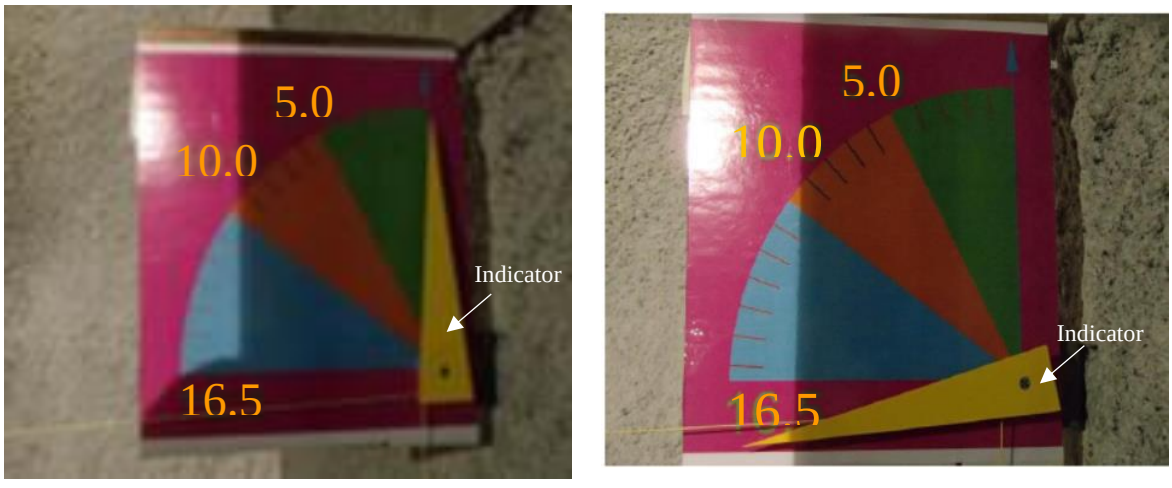

Dec. 28th , 2013

Jan. 6th , 2014

Unit: mm

Figure 3.22 Rotation of the indicator visualizing change of the horizontal displacement

3.5 Discussions

For the measurement during tunneling, the deformation of the tunnel is usually measured by Total Station only at selected sections and there is a delay to report the results of measurement. In order to improve the quality of monitoring, it is better to employ easy-to-use sensors as an auxiliary means for monitoring. The mechanical method without using electric device is expected to measure and visualize the relative displacement between two points in real-time at an acceptable cost, which makes it possible to monitor displacement at many locations during tunneling. Furthermore, the structure of the sensor is very simple so that even the onsite workers can easily repair and modify the sensor when it is broken. Thirdly, since the deformation sensor is easy to be installed on site and works immediately, an earlier acquisition of the deformations of tunnel during construction is able to be achieved. If an unusual displacement is specified early by the mechanical sensor, a precision measurement of the structure with Total Station can be carried out in response.

The aramid thread is used in this research as the connection between two points. Though it has very high elastic Young's modulus, the laboratory experiment proves there exists a little elongation of the thread over time. But the elongation of the thread can be controlled at very low level by choosing a proper light weight. The invar wire, which has been widely utilized in the accurate measurement of displacements in slope failure, would be tried in future research[8].

3.6 Applications

The original intention of the use of the mechanical deformation sensor is to find the deformations of the structure as early as possible and at as many locations as possible. It can be implemented at the area of secondary importance where large deformations might emerge, or progressive deformation of the cracks in shotcrete. As shown in Fig. 3.19, the increase of deformation of cracks can be well visualized by this sensor, and the engineers at the construction site are able to judge whether it necessary to take action to enhance the supporting strength of the tunnel synthetically. It can also work in the area of importance, which is visually blocked by the air duct or construction machine and Total Station cannot be used.

The examples have proved that the proposed method not only fulfills that purpose, but also can be extended to monitor the displacement of much smaller or larger order just by

changing the radius of pulley. Therefore, in practice, not only can the structures during construction be monitored by this deformation sensor, but the old tunnel can adopt it for monitoring of deformation during service time. This method is also applicable in monitoring the movement of the slope, the foundation pit excavation and so on.

3.7 Conclusions

The mechanical method based on the concept of On-Site Visualization is proposed to monitor the relative displacement between two points, such as convergence displacement of tunnel and the cracks of linings. The laboratory and field experiments were carried out to verify the feasibility of this method. The field measurement provides the realistic quantitative and visible evaluation of the onsite performance of the tunnel structure during excavation. Therefore, it is possible to improve the safety management of construction by using this mechanical method.

References for Chapter 3

1. Akutagawa S., Takano K. and Takenaka T.: Development of a new device to translate relative deformation into color of light and its application, *General Convention for Japan Society for Civil Engineers*, Hiroshima, CD-ROM 3-01., 2007. (in Japanese)
2. Zhang Haihua, Akutagawa Shinichi, Aono Yasuhisa and Tsujimura Koji: A mechanical method for deformation measurement and visualization in tunnel construction, *Journal of Japan Society of Civil Engineers*, Ser. F1 (Tunnel Engineering), Vol.72, pp.1-12, 2016
3. Izumi C.: Application and performance evaluation of On-Site Visualization for safety monitoring in overseas project, *Doctoral dissertation,* Kobe University, 2015
4. Source: http:// www.matbase.com (July, 2014)
5. Source: http://www.td-net.co.jp (July, 2014)
6. Sato Jun, Kusumoto Hutoshi, Domon Tsuyoshi, Nishimura Kazuo: Stabilization of tunnel face with curved tunnel face, Journal of Japan Society of Civil Engineers, Ser. F1 (Tunnel Engineering), Vol.71(1), pp.1-13, 2015 (in Japanese)
7. Aono Yasuhisa, Tsukamoto Kohei, Mashita Yoshiaki, Kumasaka Hiroo, Zhang Haihua and Akutagawa Shinichi: Application of the Mechanical deformation sensor to the natural ground which arises large deformation, *Proceedings of 43rd symposium on rock mechanics*, JSCE, pp.210-215, 2015 (in Japanese)
8. Izumi C., Akutagawa S., Zhang H. and Tsujimura K.: The development of low cost Mechanical OSV (On-Site Visualization) and its application on Bai Chay Bridge approach road in Vietnam, *Proceedings of the International Conference on Life-Cycle of Structural System*, Waseda University, pp.649-656, 2014

CHAPTER 4: VISUALIZATION OF SMALL DISPLACEMENT USING PINION ROTATION AND MIRROR REFLECTION

4.1 Introduction

Some scientific instruments like Vernier caliper or micrometers are commonly applied in a precise measurement of small distance, which is difficult to detect directly by naked eyes[1]. Other devices are used to measure the very small displacement by amplifying it to be more visible. For instance, the single lever can be found in an old caliper (see Table 2.1). It is a straightforward way to have the small scale enlarged to be identified in the monitoring of displacement. The useful magnification is limited by the physical length of the lever and position of the fulcrum.

Give an open circumstance, the light is able to travel in a straight line as long as possible, which breaks the limit of instrument size. Hence, the optical reflection is adopted in an attempt to amplify the small displacement like the single lever[2-4]. Basically, the lever system works in the form of rotation, associated with the term of angle. A relevant optical method has been tested to monitor the inclination angle of the slope using a circular mirror. The mirror is set up at the measuring point so that the ground and the mirror can move together. The observer (fixed point) can identify the inclination of the ground by the movement of image of the light-emitting diode (LED) light (fixed point) reflected from the mirror (movable point). We called this method “Single Observation Point” (SOP) [5] because multiple measuring points can be monitored at the same time from only one observation point. Since it is possible to identify the rotational angle by using a mirror, if the relationship between the linear displacement and rotational angle is established, the visualization of displacement can be achieved consequently.

In this chapter, an improved optical method for visualizing small displacement is presented in two steps based on the research of SOP. As shown in Fig. 4.1, the linear relative displacement is firstly converted into the rotation by a rotational structure. Secondly, the rotation angle is monitored visually with a rectangular mirror. As a result, the small relative displacement can be estimated just by judging the width of the shift of the mirrored color stripes. The laboratory experiments were conducted accordingly to

verify the possibility and feasibility of the method. Finally, the application of this optical method is discussed briefly.

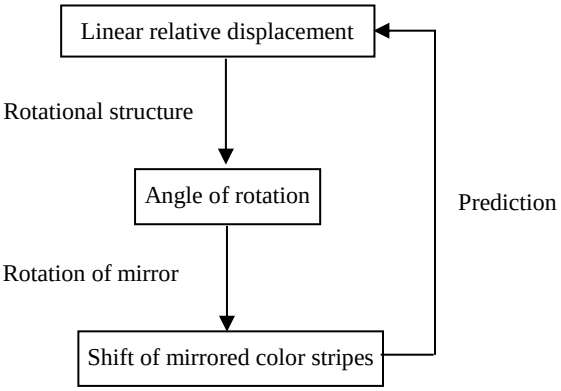

Figure 4.1 Procedure of visualization of small deformation

4.2 Visualization of Rotation Angle

4.2.1 Mechanism of the optical method

The relative displacement monitoring is premised on the basis of a precise measurement of angle. The mirror refection is made use of in a subtle way. A rectangular plane mirror is chosen as shown in Fig. 4.2. In Fig. 4.3, the plane mirror is set up at a distance l (OP) from the observer. The width of the mirror is d (M_1M_2). At the same location of the observer, the width of the zone reflected by the mirror shall be $2d$ (AB) according to the law of reflection. Here, the area reflected by the mirror at a distance is defined as the visible zone. Assume that the mirror rotates around its central axis by the angle θ while the observer keeps stable, the mirrored zone shall shift from AB to A'B' accordingly, whose width remains $2d$ (A'B'). In another word, Line AB can be seen at point P at the initial phase. As the mirror rotates gradually to an angle of θ, the range of the initial visible zone (AB) would be narrowed simultaneously and finally Line AB disappears from the view. Therefore, the rotation could be identified by checking the shift of the mirrored zone. It is noted that the reference in the mirrored zone and the observation point P should be stable during the monitoring.

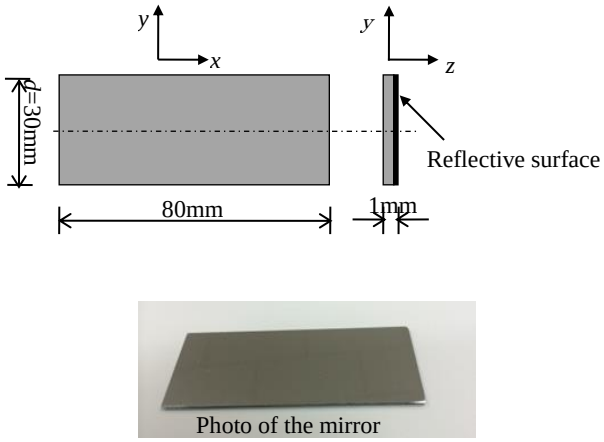

Figure 4.2 A rectangular plane mirror

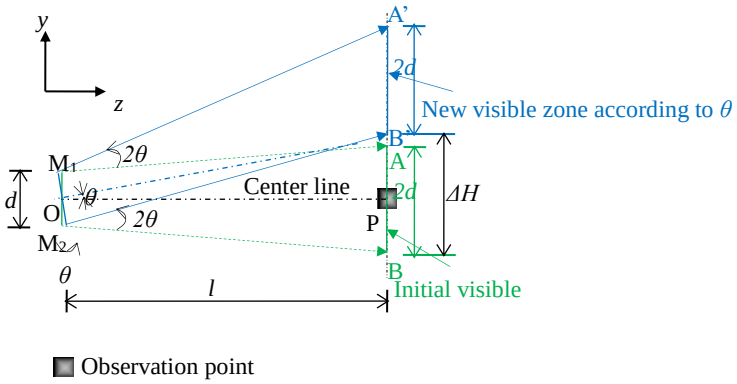

Figure 4.3 Schematic of light reflection from the mirror (*yz*-plane)

A panel with blue, red, yellow and green stripes is designed as the reference in the mirrored zone as shown in Fig. 4.4. Each of the color stripes has a width of 2*d*, equal to the width of the visible zone from the mirror. At first, the green stripe is adjusted to fill the range of the visible zone completely. If the mirror begins to rotate to angle of θ in the *yz*-plane, the reflected image of the panel will shift from green stripe to yellow stripe, to red stripe, and to blue stripe as shown in Fig. 4.5. The relationship of a complete shift of one stripe (ΔH=2*d* in Fig. 4.3), the relationship of the rotation angle, the distance between the mirror and the observation point can be expressed as follows:

$$2\theta \times l = 2d \tag{4.1}$$

$$\theta = d/l \tag{4.2}$$

where d is the width of mirror, θ is the rotation angle, and l is the distance between the mirror and the observation point.

It is found that a larger l and a smaller d could result in a more precise measurement of the rotation angle. However, the visibility of the reflected image of the panel would be poor if a very high precision was to be pursued. A proper size of the mirror and the observation distance should be determined for a better visibility with respect to the specific condition of monitoring. Since the size of the mirror and the distance from observation are decided case by case, the accuracy of this method should be analyzed in each experiment.

The reason that the observation point and the targeted panel are set up at the same location is mainly that it is easy to adjust of the mirror reflection for observation because the possible direction of the mirror for reflection is able to be judged in advance. The observation point and targeted panel can also be set up at different places so that there is a much complicated mathematical relationship between rotation angle of mirror and the width of mirrored stripes.

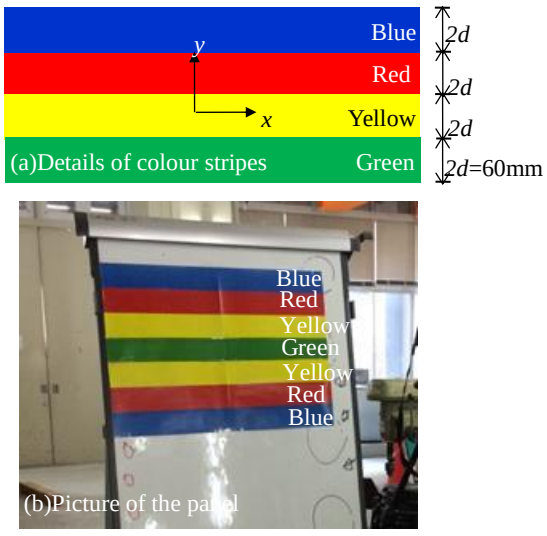

Figure 4.4 Color panel as the reference

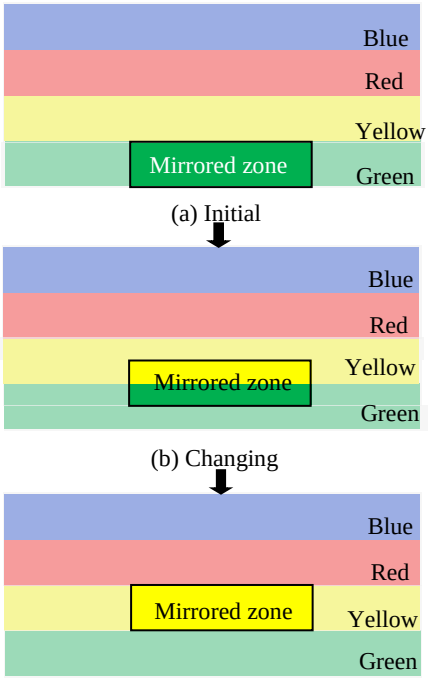

Figure 4.5 Shift of the color stripe reflected from the mirror

4.2.2 Fundamental experiment

An experiment of simply supported beam was carried out under different center loads, employing the optical method to monitor the rotation angle of the beam. The visibility and sensitivity of the method for rotation measurement could be checked. As shown in Fig. 4.6, the aluminum beam is simply supported by the rollers at its ends A and E. A series of loads is applied separately at point D in the vertical direction of *y*-axis. The color panel is set up along the extension Line AF of the beam, 11.21m away from point A. The observation point is close to the color panel, which is perpendicular to Line AF. As shown in Fig. 4.7, a digital camera at the observation point is used to record the reflected image of the color panel. The material parameters of the aluminum beam are shown in Table 4.1. Three mirrors are set up at points A, B and C in the beam's neutral plane in order to monitor the angles of rotation at the corresponding points. The defections of the beam at points B, C and D are measured by the linear variable differential transformers (LVDT).

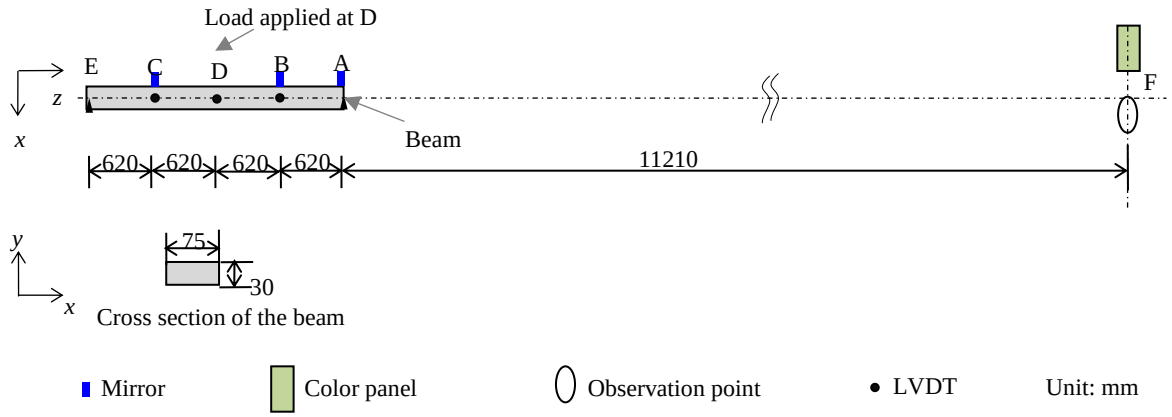

Figure 4.6 Experimental setup and instrumentation

Table 4.1 Parameters of aluminum beam

Beam size			Young's Modulus, E	Moment of Inertia, I [m^4]
Span [m]	Width [m]	Height[m]	[N/m^2]	
2.480	0.075	0.030	7.0×10^{10}	1.688×10^{-7}

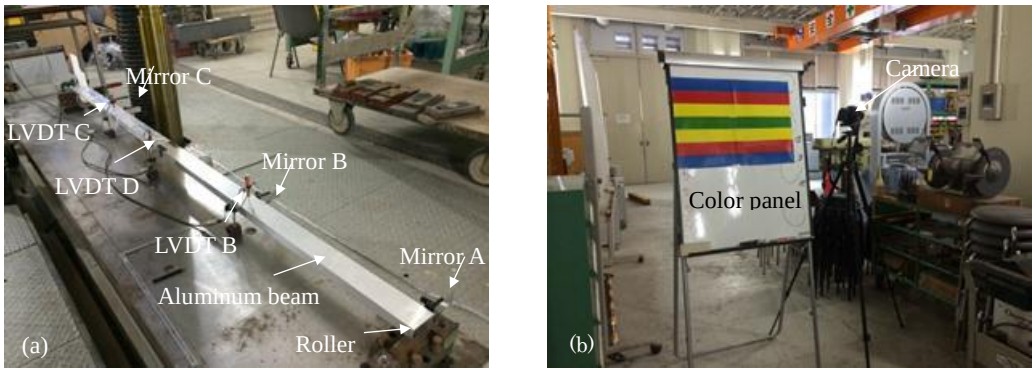

Figure 4.7 A review of the experiment (a) experiment object and (b) observation point and referring panel

4.2.3 Error analysis for visualization of angle

The rotation angles are estimated indirectly from the change of reflected color stripes. As shown in Fig. 4.5, it is easy to tell an exact value of the rotation angle in case of a complete shift of color stripe from Fig. 4.5 (a) to Fig. 4.5 (c). However, it would be difficult to

judge the value of angle in Fig. 4.5 (b) because the percentages of two different colors cannot be identified clearly. Therefore, the error in visualization of angle depends largely on the recognition of reflected color stripes. In another word, a complete shift of the mirrored color stripe determines the accuracy of the method. According to Eq. 4.2, the rotational angles of each mirror corresponding to the complete shift of color stripes are summarized in Table 4.2. The shift of the same color stripe in the three mirrors suggests a bit different rotation angle because the distance between the mirror and each observation point is different. Take the monitoring of point A for example, it is found that every 0.15 degree of angle could be visualized clearly by this method.

Table 4.2 Rotation angles estimated from different mirrors according to a complete shift of color stripe

Mirror	Distance between mirror and observation point [m]	Green [degree]	Yellow [degree]	Red [degree]	Blue [degree]
A	11.21	0	0.15	0.30	0.45
B	11.83	0	0.14	0.28	0.42
C	13.07	0	0.13	0.26	0.39

4.2.4 Result analysis

A load of 9.8N, 98N, 196N and 294N in series is applied to the aluminum beam at its midpoint D. Table 3 shows the comparison of the deflections between the experimental results from LVDTs and those obtained from theory. As shown in Fig. 4.8, the theoretical deflection at any point, *Z*, along the span of the center loaded simply supported aluminum beam can be calculated using[6]:

$$\delta_z = \frac{PL^3}{48EI}\left(\frac{3Z}{L} - \frac{4Z^3}{L^3}\right) \quad \text{for } 0 \le Z \le \frac{L}{2} \tag{4.3}$$

where δ_z is the deflection at the point *Z*, *Z* is the distance from the left support of the beam, *P* is the applied load at the center of the beam, *L* is the span of the beam, *E* is the Modulus of elasticity, and *I* is area moment of inertia of cross section.

The relative error ε_a is expressed as:

$$\varepsilon_a = \frac{Measured\ value\ (LVDT) - Theoretical\ value}{Theoretical\ value} \times 100. \tag{4.4}$$

From Table 4.3, it confirms the aluminum beam remains elastic under the centrally applied loads, which allows for the comparison of the rotation angles between theoretical value and experimental results from the mirror.

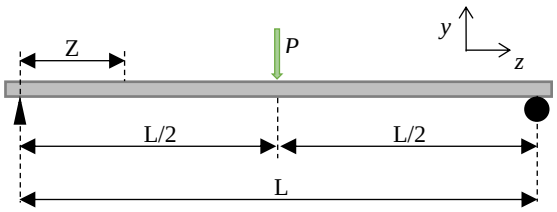

Figure 4.8 A simply supported beam with a load at the center

Table 4.3 Deflection of the beam

Applied load [N]	Deflection in the direction of *y*-axis [mm]								
	B			C			D		
	Theo. value	Measured value (LVDT)	Relative error ε_a [%]	Theo. value	Measured value(LVDT)	Relative error ε_a [%]	Theo. value	Measured value(LVDT)	Relative error ε_a [%]
9.8	0.181	0.175	3.4	0.181	0.171	5.6	0.264	0.250	5.1
98	1.812	1.822	0.5	1.812	1.830	1.0	2.636	2.597	1.5
196	3.625	3.668	1.2	3.625	3.678	1.5	5.272	5.210	1.2
294	5.437	5.516	1.4	5.437	5.520	1.5	7.908	7.822	1.1

The reflected images of color stripe are recorded by the camera as shown in Fig. 4.9. It can be found that the reflected color stripes shift accordingly as the load increases. The results of estimated angle from the mirror are shown in Table 4.4, along with the theoretical values. The estimated value of rotation angle from the mirror is calculated using Eq. 4.2. And the theoretical value of rotation angle can be given by:

$$\varphi_z = \frac{P}{16EI}(L^2 - 4Z^2) \quad \text{for } 0 \le Z \le \frac{L}{2} \tag{4.5}$$

where φ_z is the angle of deflection at point *z*.

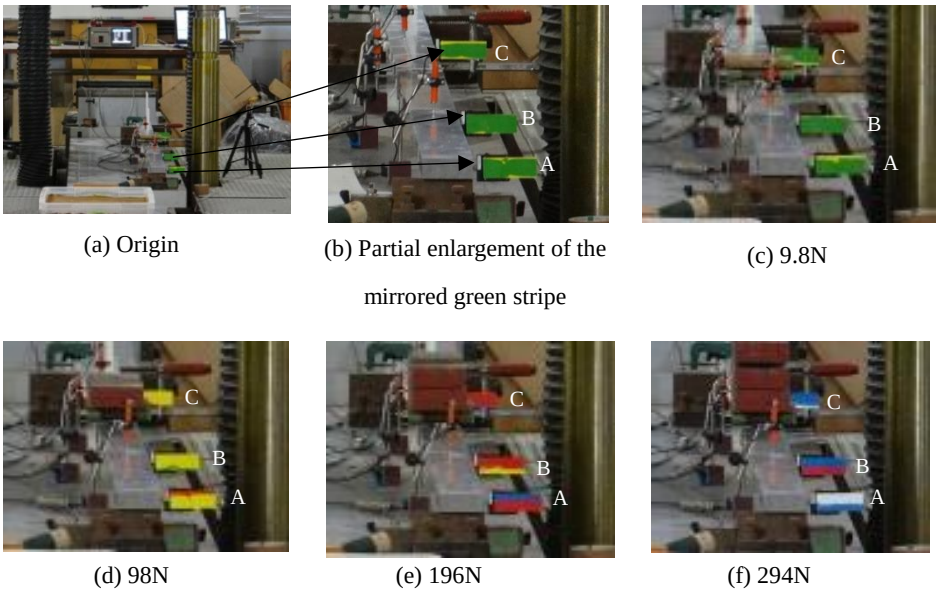

(a) Origin (b) Partial enlargement of the mirrored green stripe (c) 9.8N

(d) 98N (e) 196N (f) 294N

Figure 4.9 Reflected color stripes from the mirror

Table 4.4 Rotation angles estimated from the mirror and the corresponding theoretical value

Applied Load[N]	Rotation angle [degree]								
	A			B			C		
	Theo. value	Estimated value	Relative error ε_b [%]	Theo. value	Estimated value	Relative error ε_b [%]	Theo. value	Estimated value	Relative error ε_b [%]
9.8	0.018	0.020	11.1	0.014	0.015	7.14	0.014	0.015	7.14
98	0.183	0.192	4.92	0.137	0.144	5.11	0.137	0.145	5.84
196	0.366	0.376	2.73	0.274	0.255	-6.93	0.274	0.265	-3.28
294	0.548	0.568	3.64	0.411	0.371	-9.73	0.411	0.421	2.43

The relative error ε_b is given by:

$$\varepsilon_b = \frac{Measured\ value\ (LVDT) - Theoretical\ value}{Theoretical\ value} \times 100 \qquad (4.6)$$

At the supports (points A and E), there are only rotations while the deflections are zero. Note that the deflections at the measuring points B and C will influence the final results of rotation angle. For example, the deflection at point B is 5.5mm under the load of 294N. The proportion of effect γ due to the deflection can be given by:

$$\gamma = \frac{2u}{v} \times 100 = \frac{2u}{w+2u} \times 100 \quad (4.7a)$$

where u is the offset of the mirror in the direction of x-axis, equal to the deflection at the measuring point of the beam, v is the true total amount of the shift of reflected image from the mirror, and w is the measured total amount of the shift of reflected image from the mirror.

Thus, at the measuring point B, we can have:

$$\gamma = \frac{2\times5.5}{153+2\times5.5} \times 100 = 6.7(\%) \quad (4.7b)$$

When the deflection of point B is 0.17mm at the loading of 9.8N, the proportion of effect γ is about 0.17×2/6=5.7 %. Hence, the effect could be ignored when the displacement of the mirror is very small. In this case, a small angle of rotation could be measured and visualized appropriately by the mirror.

4.3 Visualization of a Small Displacement

4.3.1 Mechanism of the small displacement sensor

A linear displacement can be transformed into the arc curve by the rotational structure, such as the pulley, as shown in Fig. 4.10. The rotation angle is able to be attained by the optical method which is tested in section 4.2. Combining these two functions, a mechanical displacement sensor is proposed to monitor the relative displacement between two points. The relative displacement can be detected and transformed into rotation in several ways, including the wire-pulley type and the rigid rack-pinion type as shown in Fig. 4.11. For pulley-wire type, the relative displacement is measured in the direction of line of points 1 and 2. For rack-pinion type, the relative displacement is measured along the axis of the rack. The mirror is fixed on the rotational structure so that both of them could have an identical angle of rotation.

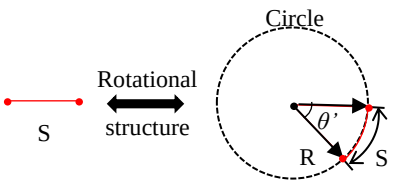

(a) Straight line (b) Arc of a circle curve

Figure 4.10 Displacement transformation between an arc and the line

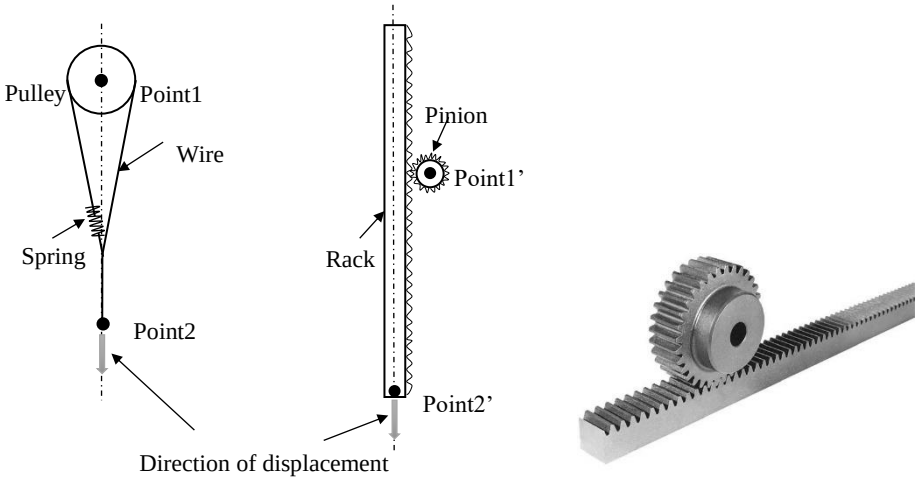

(a) Wire-pulley type (b) Rack-pinion type (c) Photo of rack-pinion

Figure 4.11 Different rotational structures for displacement transformation

The relationship between relative displacement and rotation angle is given by:

$$S=R\times\theta' \tag{4.8}$$

$$\theta'=S/R \tag{4.9}$$

where S is a relative displacement between two points, θ' is the rotation angle of rotational structure, and R is radius of rotational structure.

Since the mirror has the same rotation angle as the rotational structure, we have:

$$\theta=\theta' \tag{4.10}$$

In case of a full shift of one color stripe reflected from the mirror, from Eqns. 4.2 and 4.5, we can derive that:

$$\theta = d/l = S/R \tag{4.11}$$

$$S= R\times d/l \tag{4.12}$$

where d is the width of mirror, and l is the distance between mirror and observation point.

It is therefore found that the precision of this mechanical displacement sensor is determined by the width d of mirror, the radius R of axis of rotational structure and the

distance *l* between mirror and observation point.

4.3.2 Experimental design

There are two structures for transforming the linear displacement into the rotation as discussed in section 4.3.1. The idea using the pulley and wire has been introduced in Chapter 3 to visualize the relative displacement of mountain tunnel linings[7]. In this research, a structure of rack-pinion type is adopted because it seems to be a more reliable way to detect a small relative displacement between two points. A similar experiment of simply supported beam under different loads was carried out to verify the feasibility of the displacement sensor as shown in Fig. 4.12. A load of 0.98N, 1.96N, 2.94N, 3.92N, and 4.9N in series is applied at the center of the beam. The deflection at midpoint D is monitored by this mechanical displacement sensor as shown in Fig. 4.13. In this section, the information about the mechanical displacement sensor using the mirror would be mainly dealt with. The observation distance of Line DF is 10m. The radius of the pinion is 7.96mm. The displacements estimated from the mirror D corresponding to the full shift of each color stripe are summarized in Table 4.5 according to Eq. 4.12. It is found that every 0.02mm could be visualized clearly by the mirror D.

Table 4.5 Displacement value estimated from mirror D according to a complete shift of reflected color stripe

Mirror	Distance between mirror and observation point [m]	Green [mm]	Yellow [mm]	Red [mm]	Blue [mm]
D	10.00	0	0.02	0.04	0.07

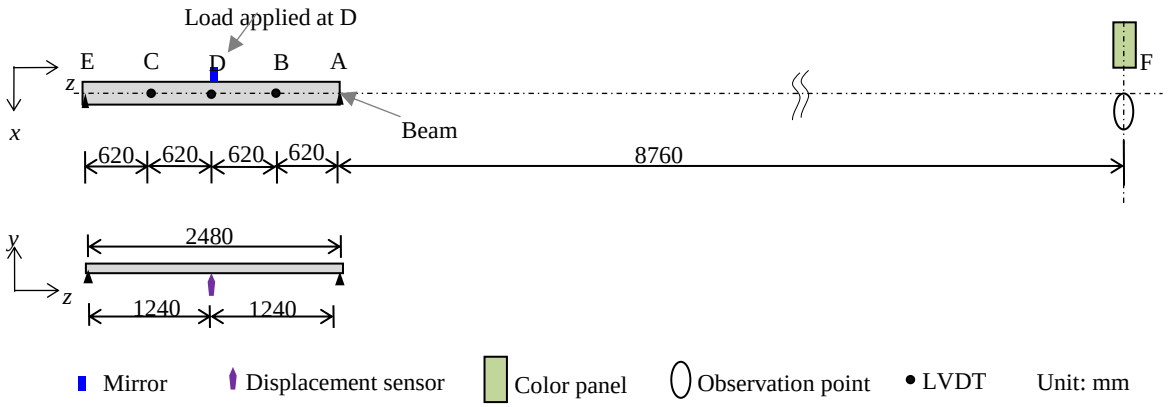

Figure 4.12 Experimental setup and instrumentation using displacement sensor

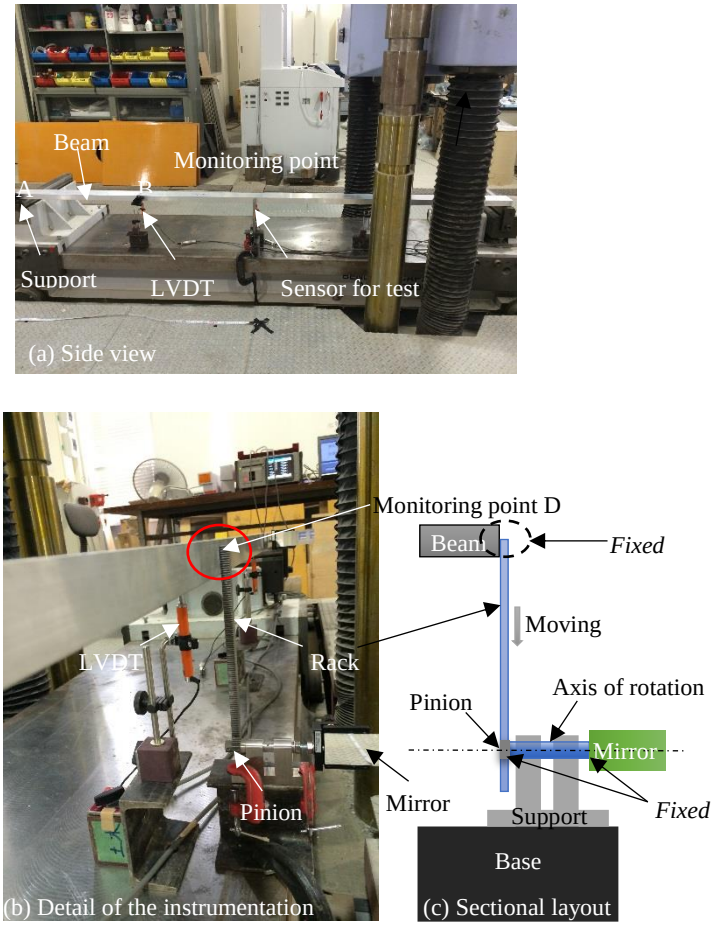

Figure 4.13 Photos of the simply supported beam monitored by the displacement sensor

4.3.3 Result analysis

The mirror is set up at the station which stays stable during monitoring. Therefore, the mirror is mobilized to rotate by the rack without any offset when the displacement occurs. The reflected images of the color stripes are recorded by the camera as shown in Fig. 4.14. The reflected color stripes from the mirror shift corresponding to applied loads. As soon as the load of 4.9N is applied, the deflection is too large to be measured by the sensor.

The results of displacements by the proposed sensor and LVDT are shown in Table 4.6. The estimated value of deflection at midpoint D is calculated using Eq. 4.12. The relative error ε_c is expressed as:

$$\varepsilon_c = \frac{Estimated(Sensor) - Measured(LVDT)}{Measured(LVDT)} \times 100 \quad (4.13)$$

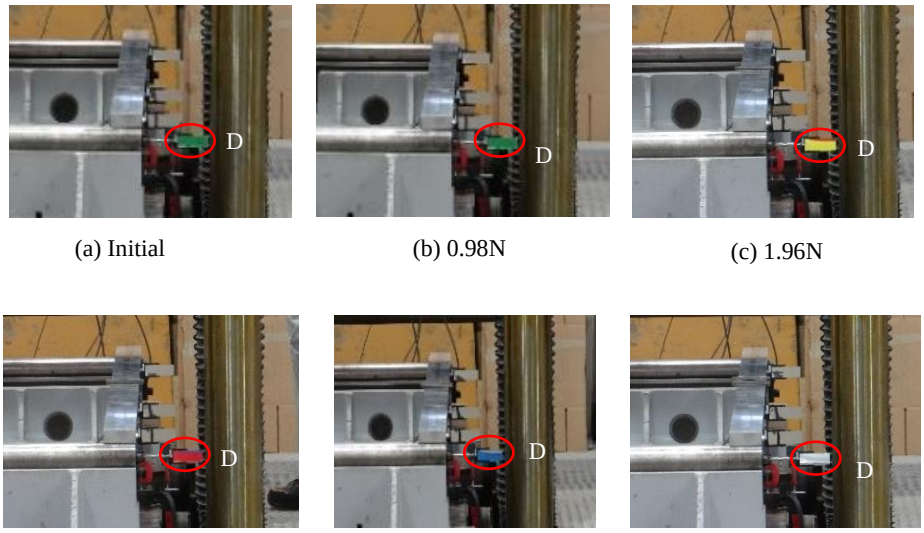

(a) Initial (b) 0.98N (c) 1.96N

(d) 2.94N (e) 3.92N (f) 4.9N

Figure 4.14 Reflected stripe from the mirror under different load

We can find that the measured values by LVDT are not in accordance with the theoretical values, which suggests this is not an ideal simply supported beam experiment in case of very small loads. The loading method, the weight of measuring devices, the supports etc. might have much influence on the final results. Therefore, the measured values by the displacement sensor are analyzed in comparison with those measured by LVDTs. The results in Table 4.6 show that a small displacement can be visualized approximately by this mechanical displacement sensor using the mirror with a resolution of 0.02mm.

Table 4.6 Deflection of the beam at midpoint D of the beam

Deflection at midpoint D [mm]	Applied load [N]				
	0.98	1.96	2.94	3.92	4.90
Estimated value by sensor	0.010	0.029	0.050	0.081	-
Measured value by LVDT	0.009	0.035	0.055	0.110	0.112
Theoretical value	0.026	0.052	0.079	0.105	0.131
Relative error ε_c [%]	11.1	-17.1	-9.1	-26.1	-

4.4 Remarks on Accuracy and Precision of Visualization of Displacement

The accuracy of this method is mainly determined by the detection of the linear displacement, which is transformed into the rotational movement. Therefore, a high-quality pinion-rack system is required.

For the precision analysis. The main factor is the rotation angle visualized by the mirror. The use of precision manufactured mirror is highly recommended. Otherwise, the edge of the mirrored color stripe might not be straight, making it hard to identify the rotation angle correctly, like the image as shown in Fig. 4.14 (c). The temperature of the surroundings also has some effect on the mirror's properties. A stable room temperature is preferred during monitoring.

The second factor is the resolution of displacement visualized by this method. The observer is able to find the small displacement just by identifying the change of the reflected color stripes from the mirror. As shown in Fig. 4.5, every complete shift of color stripe indicates a displacement of about 0.02mm while the monitoring distance between the observer and the mirror is 10m. The value of double color stripes can be estimated by the linear interpolation between the data of corresponding color stripes. Higher resolution or sensitivity of the method can be achieved by means of a longer monitoring distance l and finer color stripes. It might weaken the visibility of reflected image of the color stripes from the mirror. A telescope could be used as an auxiliary measure during measurement.

Finally, the observer is required to monitor the mirror at the same point every time. Since the small displacement can be identified in this mechanical method, any tiny influence during monitoring could lead to a large relative error in the measured result.

4.5 Potential Applications

The method for small displacement monitoring can be carried out without using electricity, which makes it attractive in the long-term safety management of the structures. Based on the results of the above experiments, the field test in a tunnel is going to be conducted in the near future as shown in Fig. 4.15. It is thought to be a promising method to be applied in monitoring cracks (a resolution of 0.1~0.2mm is required for monitoring[8]) in underground structures, movement of the rock slope, supporting structure in mining engineering, where small relative displacements inevitably occur.

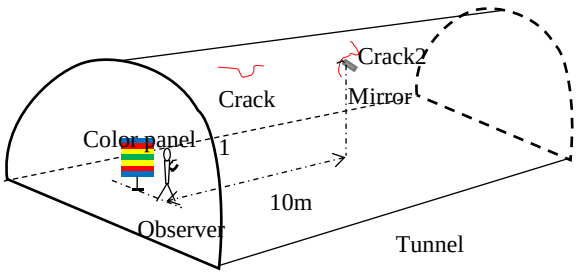

Figure 4.15 A diagram of crack monitoring using the proposed method in the tunnel

4.6 Conclusions

A mechanical method is introduced to monitor and visualize small linear displacements in structures based on the concept of On-Site Visualization. Its mechanism lies in that linear displacement is transformed into the angle of rotation, which is identified by making use of the mirror reflection law. The results of laboratory experiments show the feasibility of visualization of the rotation angle and small displacement. The factors influencing the accuracy and precision of this method are discussed briefly, which should be taken into account in practice.

References for Chapter 4

1. Kawai Toshihide: An introduction to the usage of measuring tools-Visual books, Nikkan Kogyo Shimbun, 2008 (In Japanese)
2. Sirohi Rajpal S., Kothiyal Mahendra P.: Optical Components, systems, and measurement techniques, *Marcel Dekker, Inc.*, 1990
3. Lorrain Oaul: An optical lever for measuring very small rotational oscillations, *Optics and lasers in Engineering*, Vol.15(3), pp.197-20, 1991
4. Hogan J. M., Hammer J., Chiow S. W., Dickerson S., Johnson D. M. S., Kovachy T., Sugarbaker A. and Kasevich M. A.: Precision angle sensor using an optical lever inside a Sagnac interferometer, *Optics Letters*, Vol. 36(9), pp.1698-1700, 2011
5. Akutagawa S., Nakata K., Nishio A. and Yamada H.: Single observation point method for measurement and real-time visualization of inclination using a mirror for rock engineering projects, *8th Asian Rock Mechanics Symposium*, Japan, Sapporo pp.2433-2441, 2014
6. Sakimoto Tatsuro: Structural mechanics, *Morikita Publishing Co., Ltd*, 2007 (In Japanese)
7. Akutagawa S., Zhang H., Terashima M. and Tsujimura K.: A mechanical method for monitoring and visualization of deformations of tunnel structures, *8th Asian Rock Mechanics Symposium*, Japan, Sapporo, pp. 2309-2316, 2014
8. Ito T., Baba K., Shiroma H., Yoshita I. and Nakagawa K.: Investigation of cracks in lining concrete and estimation on the exfoliation of concrete pieces, *Journal of JSCE*, Vol.2004, No.763 pp.87-93, 2004 (in Japanese)

CHAPTER 5: VISUALIZATION OF BEAM DEFORMATION DUE TO TEMPERATURE CHANGE USING A THIN BAR

5.1 Problem Statement

The deformation of structure happens due to the 1) applied load or 2) temperature change. In the first, deformation is described by the relative displacement between two discrete points which can be visualized as the movement of rotation. The temperature change in the second case usually introduces thermal deformation in the structures[1]. If the temperature-induced deformation in structure is permitted freely, the structure would expand or contract, corresponding to the positive or negative change in temperature. At the same time, the internal stress would not occur. If the structure is constrained strictly, the thermal stress would be developed while the change in length is difficult to identify. The stress-strain behavior of the structure is quite different from that of the normal structure under loading. That is to say, the stress of structure cannot be deduced easily by the measurement of thermal deformation.

The thermal deformation is possible to put the structures that are sensitive to the temperature change in danger. In underground construction, the axial forces of steel strut (beam) used in the foundation pit vary especially during a summer day even though the excavation is stopped[2,3]. The force reaches the maximum value during the noon while drops to the lowest in the night. The main cause of variation of force of the struts is exactly the temperature change[4,5]. Therefore, in order to prevent the maximum strut forces from exceeding the designed value, it is of importance to monitor the axial force of the strut as well as its deformation.

As for monitoring the force, the common way is to use a load cell in practical measurement. We have known that it is difficult to estimate the strut force just by measuring the thermal deformation of the strut. So the mechanical methods to measure the relative displacement between two points in the previous two chapters can’t apply to this case so as to evaluate the stress directly. Another issue related to monitoring the deformation is that the thermal deformation is very small, which requires a high accuracy of the measurement.

5.2 A Solution for Relating Deformation to Force

Ideally, the thermal force of strut in an excavation can be obtained in two steps by using the principle of superposition as shown in Fig. 5.1. First, the free thermal deformation (elongation) in Fig 5.1 (b) is calculated as[6]:

$$\Delta x = \alpha \times \Delta T \times L \tag{5.1}$$

where Δx is the thermal elongation of strut, α is the coefficient of linear thermal expansion, and ΔT is the change in temperature, and L is the strut span.

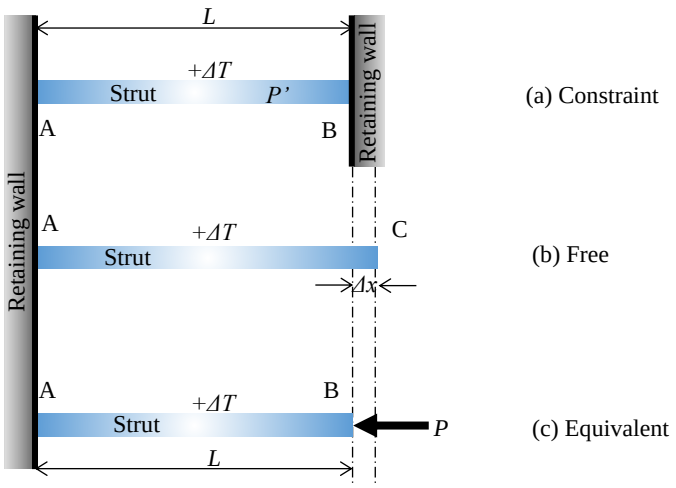

Figure 5.1 Thermal deformation in a retaining wall and strut system

Then, an external supporting force is applied at free end B of the strut (Fig. 5.1 (c)) to restore the strut to the original position on the constrained condition subjected to the temperature change (Fig. 5.1 (a)). The compression should be Δx. So the axial force of strut with both ends constraint can be given by:

$$P = EA(\Delta x/L) = EA(\alpha \Delta T) \tag{5.2}$$

where P is the axial force of strut, E is the elastic modulus, and A is the cross sectional area of the strut. The internal force developed in the strut due to the constraint by the retaining wall can be expressed as:

$$P' = P = EA(\Delta x/L) \tag{5.3}$$

where *P'* is the thermal axial force of strut.

Therefore, the relation between the deformation and axial force is established theoretically. It is possible to compute the axial force of strut by measuring the deformation *Δx*.

5.3 Mechanism of Small Displacement Sensor

Since the thermal deformation of a free beam is very small, the relative displacement between two nearby points in the body is much smaller. It is difficult to visualize the small displacement clearly by the rotational structures like the pulley. There should be some improvement to the rotational structure in such case of small displacement visualization. A segment of the beam can result in a larger thermal deformation than that between two points near to each other. Furthermore, the rotational structure with a small-diameter axis performs much sensitively to the linear movement.

Therefore, a mechanical sensor is designed as shown in Fig. 5.2 for visualizing small displacement. The thin steel bar with a radius *r* is sandwiched between two rigid beams. A plastic mini-flag is attached perpendicularly at one end of the bar with the length *l* .When a relative movement occurs between the two beams, the thin bar would be mobilized to rotate with an angle *θ*. The relationship between the displacement and rotation angle can be expressed as:

$$d = r \times \theta \tag{5.4}$$

where *d* is the linear relative displacement (movement), *r* is radius of the thin bar (needle), and *θ* is the rotational angle. For example, assuming *d* =0.1mm and *r* =0.5mm, the angle of *θ* will be 11.5°, which could be recognized by the rotation of the flag (*l* =60mm) attached on the steel bar. The values can be read directly from the board with scales behind the flag.

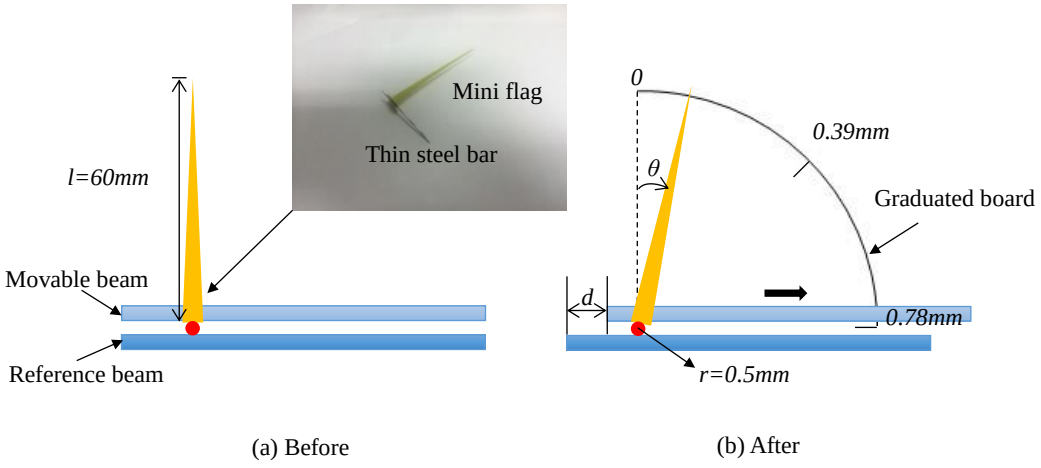

Figure 5.2 Mechanism of the displacement visualization by mechanical sensor

5.4 Experiment Description and Result Analysis

Two types of experiments were presented in order to verify the feasibility of the sensor for small displacement visualization in the following two sections respectively. The first one is designed to test the monitoring of small displacement by this proposed sensor. The other is to test the visualization of small thermal deformation by the sensor.

5.4.1 Experiment of a simply supported beam

(I) Experiment

An experiment of a simply supported beam was conducted under different center loads as shown in Figs. 5.3 and 5.4. The aluminum beam is supported by the rollers at both ends. The material parameters of the main aluminum beam are presented in Table 5.1. Under the loading at the center C, the upper side of the aluminum beam is in a state of compression, while the opposite side is in tension. In order to monitor the deformations (change in length of AC) at the top and bottom of the beam subjected to different center loads, another two aluminum beams used as the references are set up on the two sides of the main beam respectively. Each reference beam has one end fixed at point C. The length of reference beam could be regarded as the same when bending together with the main aluminum beam. The mechanical sensor is set up between the main beam and the reference one. The deformations at the upper side of the beam are also checked by a dial indicator. The deflections at points B, C and D are measured by linear variable differential

transformers (LVDT).

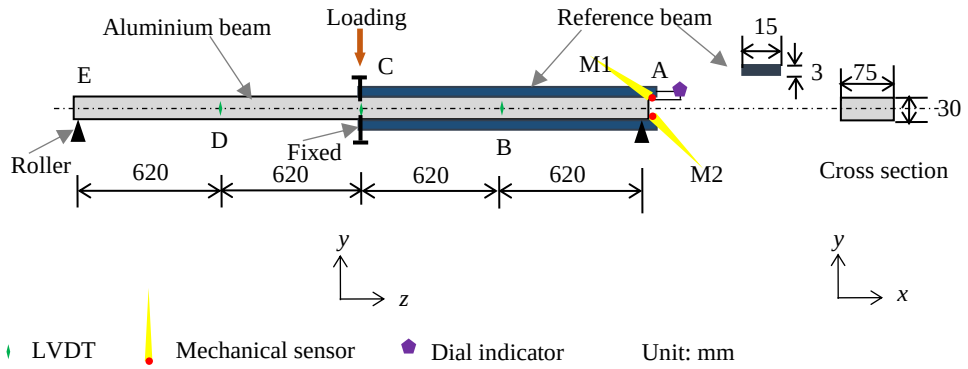

Figure 5.3 Layout of the experiment of the simply supported beam

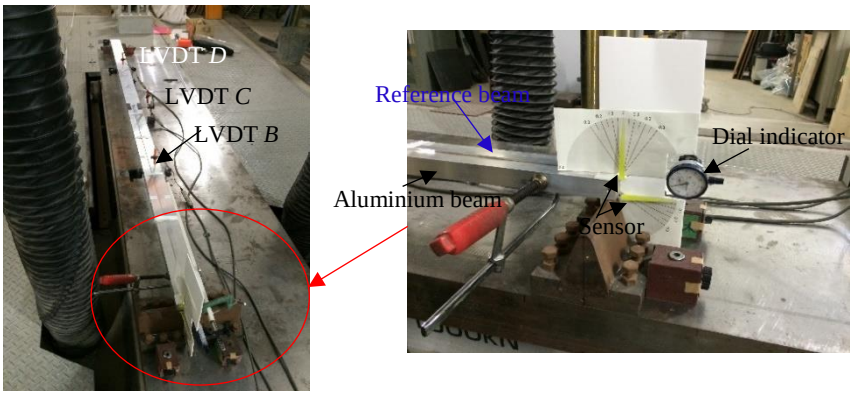

Figure 5.4 A view of the experiment

Table 5.1 Parameters of aluminum beam

Beam size			Young's Modulus, E	Moment of inertia, I
Span [m]	Width [m]	Height [m]	[N/m^2]	[m^4]
2.480	0.075	0.030	7.0×10^{10}	1.68×10^{-7}

(II) Result analysis

A load of 9.8N, 98N, 196N and 294N in series is applied at the center of the aluminum beam. A comparison of the deflections between the experiment results measured by LVDTs and those calculated from theory is shown in Table 5.2[7] (the same as that of Table

4.3, only the marking numbers are different). It can be found that results from experiment and theory agree very well, which suggests that the aluminum beam stays elastic under the center loadings. Thus it allows a comparison of the change in length of AC between the experimental and theoretical results.

Table 5.2 Deflection of the beam

	Deflection in the direction of *y*-axis [mm]								
Applied	D			B			C		
Load[N]	Theo. value	Measured value	Relative error[%]	Theo. value	Measured value	Relative error[%]	Theo. value	Measured value	Relative error[%]
9.8	0.181	0.175	3.4	0.181	0.171	5.6	0.264	0.250	5.1
98	1.812	1.822	0.5	1.812	1.830	1.0	2.636	2.597	1.5
196	3.625	3.668	1.2	3.625	3.678	1.5	5.272	5.210	1.2
294	5.437	5.516	1.4	5.437	5.520	1.5	7.908	7.822	1.1

Fig. 5.5 shows the records of the visualization of relative displacements by the mechanical sensors under different center loads. At first, the relative displacement is too small to be detected when the load is 9.8N. Then, the sensors react to rotate as soon as the heavier load is applied. Moreover, the readings of the relative displacements from the two mechanical sensors are in agreement with those from the dial indicator. Thus, the results from upper mechanical sensor (M1) will be adopted in the next comparisons.

The measured values as shown in Table 5.3 are read directly from Fig. 5.5 with an accuracy of 0.05mm. It shows that the mechanical sensor can give an acceptable result of the small relative displacements, comparing with the theoretical value. The feasibility of the sensor for small displacement visualization is proved.

Table 5.3 Compression of the upper side of the beam

Applied load [N]	Theoretic value [mm]	Measured value [mm]
9.8	0.004784	-
98	0.047836	0.04
196	0.095673	0.10
294	0.143509	0.15

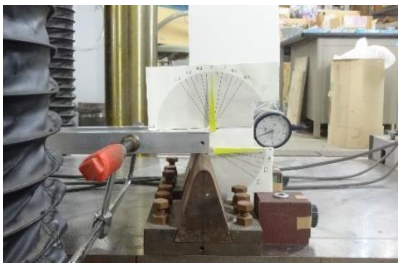

(a) Load of 9.8N: *d* is too small to be read

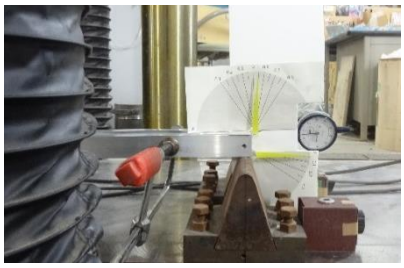

(b) Load of 98N: *d*=0.04mm

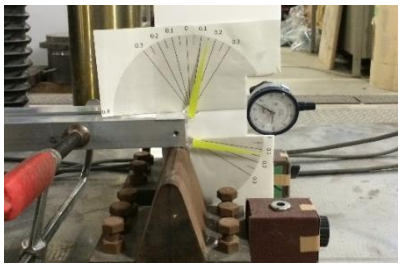

(c) Load of 196N: *d*=0.10mm

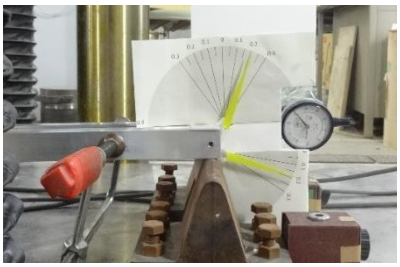

(d) Load of 294N: *d*=0.15mm

Figure 5.5 Results of relative displacements measured by the mechanical sensor and dial indicator

5.4.2 Experiment of thermal expansion

(I) Experiment

A thermal expansion experiment was designed to investigate the deformation of metals by using the proposed sensor as shown in Fig. 5.6. A steel block is used to model the retaining wall of the excavation, which serves as the constraint of the aluminum beam during thermal expansion. An aluminum beam (basal beam), simulating the strut of the excavation, is fixed at its both ends by the stainless bolts on the steel block. There is another aluminum beam (free beam) with one end fixed on the basal beam. The free beam has the same cross section as the basal one. The steel block and aluminum beams expand with the increasing temperature. Since their linear coefficients of the thermal expansion are different (Table 5.4), the aluminum beam shall have a larger expansion than the steel theoretically. For the two aluminum beams, because the basal beam is fixed at two ends at the steel block while the other is fixed at only one end, they are supposed to behave differently even if the change in environment temperature is the same.

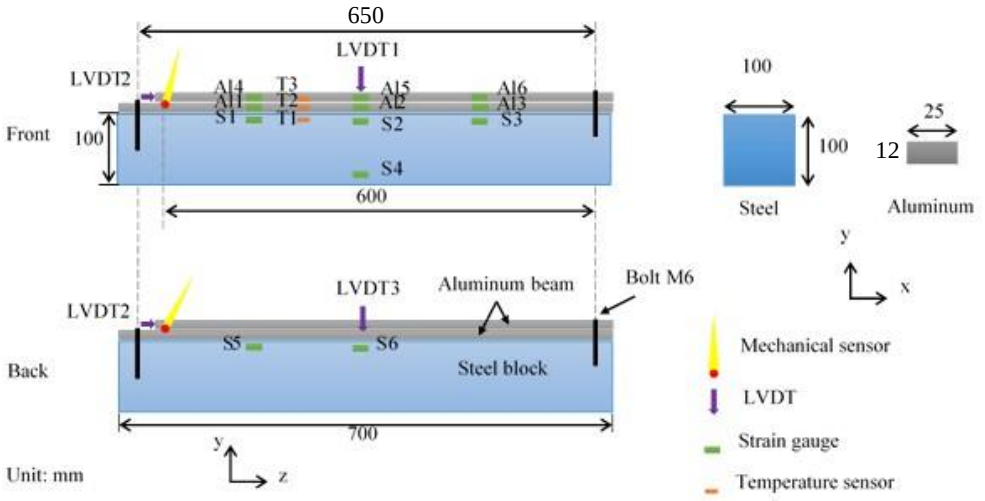

Figure 5.6 Layout of the thermal expansion experiment

Table 5.4 Parameters of the metals

Metal	Length [mm]	Width [mm]	Height [mm]	Coefficient of thermal expansion [10^{-6}/°C] at 20°C
Steel block	700	100	100	10.5
Aluminum beam (basal)	700	25	12	23.9
Aluminum beam (free)	650	25	12	23.9

The mechanical sensor sandwiched between the two aluminum beams is set up to visualize their relative displacements as the temperature changes. In order to increase the rotation frictional force between the sensor and the beams, a load of 6.4N (650g) is applied at the left end of the free beam (Fig. 5.7). In addition, the strain gauges are used to measure the strain of the steel block and the two aluminum beams (Fig. 5.6). The movement at the center of the two aluminum beams in the vertical direction is measured by two LVDTs respectively with reference of the steel block. The movement at the free end of aluminum beam is monitored by LVDT2, which is expected to be used as a reference of the mechanical sensor. The surface temperatures of the steel block and aluminum beams are collected by the thermocouple sensors. A digital thermometer is positioned 10cm above the concrete pavement to record the air temperature during the experiment.

(a) Front view (b) Auxiliary for increasing the friction

Figure 5.7 Experimental setup for the thermal expansion of aluminum beam

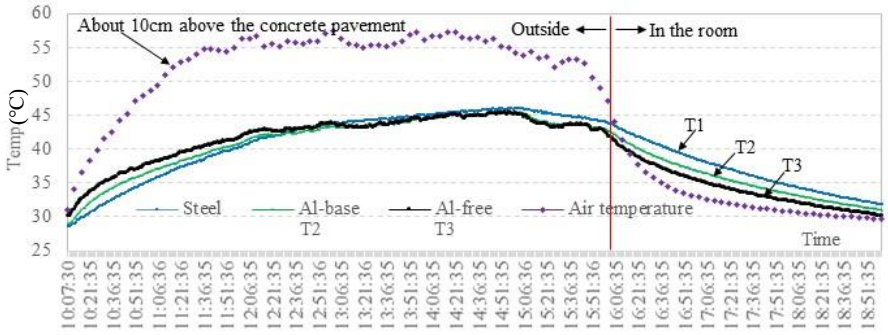

Figure 5.8 Surface temperature of the metals along with the air temperature (Aug. 4th, 2015, Kobe)

The experiment was conducted on a fine day in August of 2015. It started from 10:05 in the morning. All the experimental materials were exposed directly in the sunshine as shown in Fig. 5.6. At 16:00 when the sunlight became weak, the experiment site was shifted into the laboratory. The measured data were recorded automatically at an interval of 1min until 19:00. Fig. 5.8 shows the surface temperature of the steel block and aluminum beams changes along with the air temperature. The air temperature rise accelerated as soon as the experiment began, leveled up from 12:00, and then the peak temperature occurred at about 14:00 in the afternoon. It should be noted that sine the thermometer was set up 10cm above the concrete pavement outside, the value of peak air temperature would be higher than that of the weather broadcast. The surface temperature of the metals reached a peak from 14:30 to 15:00. As soon as the experiment was shifted

to the laboratory room at 16:00, the air temperature dropped dramatically, while the surface temperature of the medals dropped gradually and at last it tended towards the room temperature.

(II) Result analysis

The visualization of the relative displacements were recorded at an interval of about 30mins. Fig. 5.9 presents the typical results. It can be found that the maximum relative displacement between the aluminum beams occurred between 15:00 to 16:00. After the experiment continued in the laboratory room, the measured relative displacement decreased slowly. The yellow flag rotated in a clockwise direction, which suggests that the basal aluminum beam has a tendency to move left relative to the free beam due to the increasing temperature.

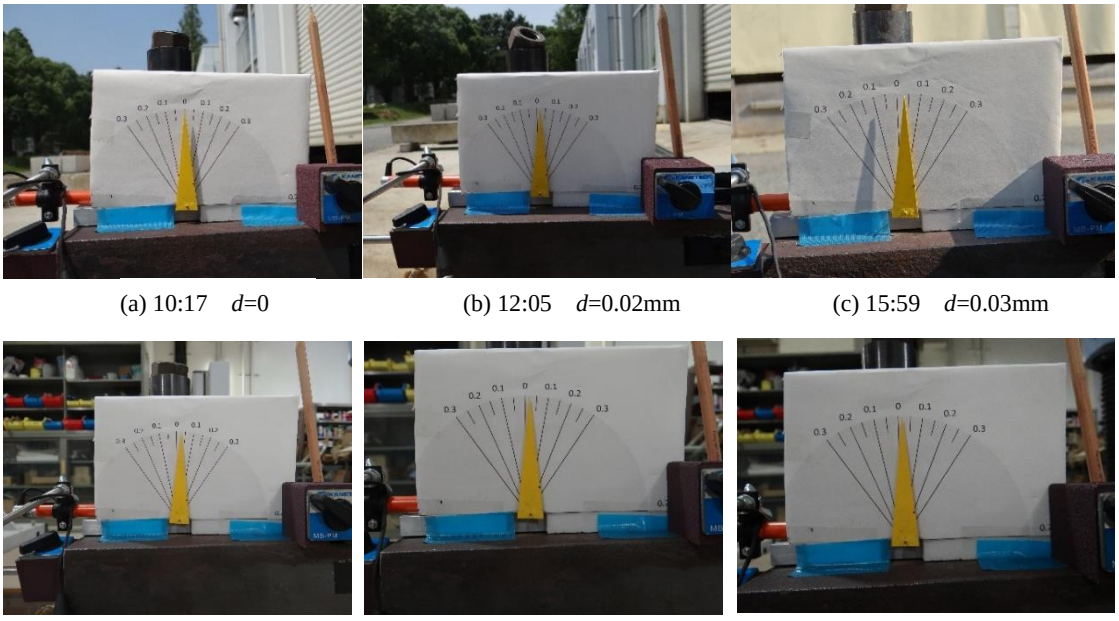

(a) 10:17 d=0 (b) 12:05 d=0.02mm (c) 15:59 d=0.03mm

(d) 17:01 d=0.025mm (e) 18:15 d=0.02mm (f) 19:03 d=0.02mm

Note: d is the relative displacement between the two aluminum beams

Figure 5.9 Visualization of relative displacements between two aluminum beams

From Fig. 5.10, we can see that at most of the same time the positive strain of the aluminum beams is larger than that of the steel block, which proves the aluminum extends more than the steel. The strains of the two aluminum beams are quite close, which means the constraint condition of the basal beam has only a little effect on the development of

its strain. All the strains of the metals dropped sharply as soon as the experiment was moved into the room at 16:00. Here, an interesting phenomenon was observed that the strains of metals dropped to be negative. The fact that the room temperature was lower than the air temperature at the start of experiment might be a main cause of this result.

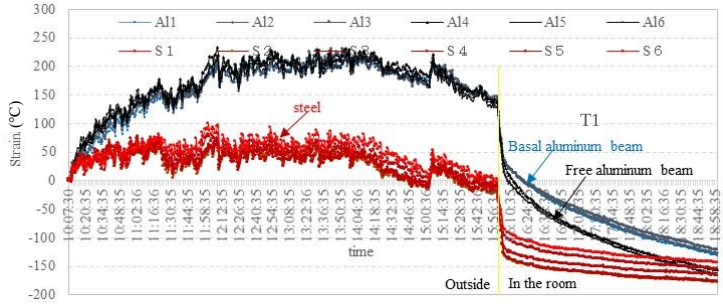

Figure 5.10 Strain of the steel block and aluminum beams

Fig. 5.11 shows the heaving of the two aluminum beams happened. The heaving of the basal aluminum beam is larger than that of the free beam at any given time during the experiment.

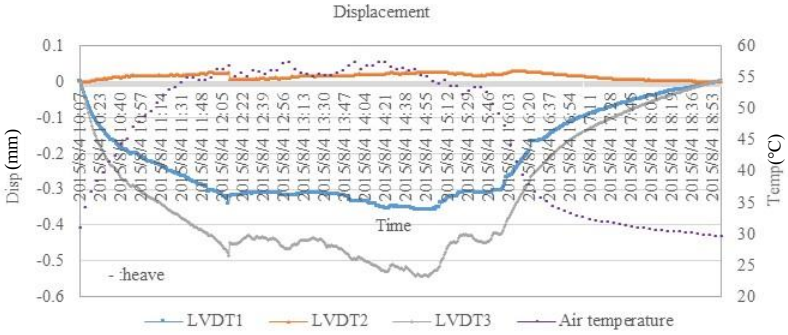

Figure 5.11 Relative displacements measured by LVDTs

Therefore, the deformation mechanism of this experiment could be speculated about as shown in Fig. 5.12. All the metals expand as the temperature increases. For the basal aluminum beam, it expands more than the steel block while having both ends fixed on the steel block. As a result, the basal aluminum beam is forced to heave subjected to the increasing temperature at its center. Since the free aluminum beam is fixed at one end with the basal one, they would have the same rotation angle at the fixed end, causing the free beam rising up at its free end (left end). Thanks to the additional weight applied at the left end of the free beam (Fig. 5.7), the sensor could remain nipped exactly between

the two beams. So it is easy to understand the heave of the free beam is smaller than that of the basal beam at the midpoint, resulting in the clockwise rotation of flag.

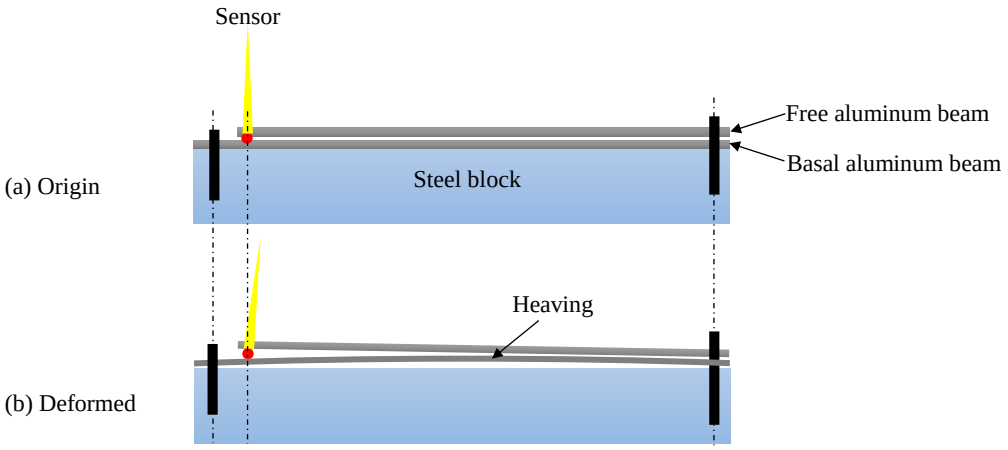

Figure 5.12 Estimate of deformation process due to temperature change

Fig. 5.13 shows the displacements measured by the mechanical sensor and those measured by LVDT2 at the end of free beam. The displacements measured by these two methods are not the same. The displacement measured by LVDT2 is the horizontal component of the superposition of the relative expansion of free aluminum beam and circular movement of free end due to the rotation of free beam. On the other hand, the displacement between the two aluminum beams measured by mechanical sensor results mainly from the special pattern of deformation of the two beam.

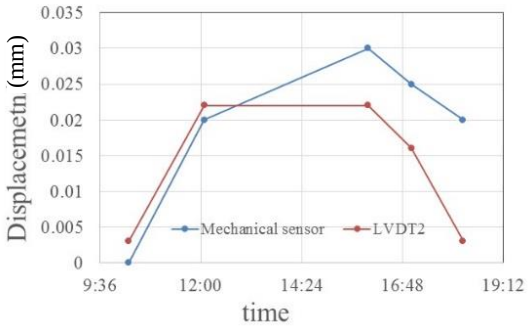

Figure 5.13 Displacement results

5.5 Discussions

The constraint condition has much effect on the performance of the aluminum beam subjected to the temperature change. In the above thermal experiment, since there exists the manufacturing error in the bolt holes, it is difficult to form perfect rigid constraints on both ends of the basal aluminum beam. As a result, a special pattern of deformation was observed in the case of temperature change. The proposed sensor is able to visualize this kind of deformation by simple rotation as long as the thin bar keeps sandwiched between the two beams.

In order to estimate the axial force of strut induced by the temperature change, the rigid constraint on both ends is required to prevent the basal beam from heaving. The monitoring method by the proposed sensor is similar to the above experiment as shown in Fig. 5.14. It is noted that the free beam should be made of the same material as the strut. Based on the visualized value of elongation of the free beam, the ideal thermal axial force is possible to be calculated by using Eq. 5.3.

In practical excavation engineering, there are many influence factors to consider for estimating thermal axial force while using this simple deformation sensor. The very important fact is that the retaining wall would usually deform under the acting force generated from the struts. Hence, the steel strut would be initially expand freely, after some free elongation, the ongoing expansion would be restrained. For another, although the length of the strut is usually large, it only needs to select one part of the strut along the longitude axis for monitoring using the proposed sensor. By the systematic monitoring of the deformation of the excavation with other measuring instruments, the proposed method is possible to be applied for estimating the thermal force of strut approximately.

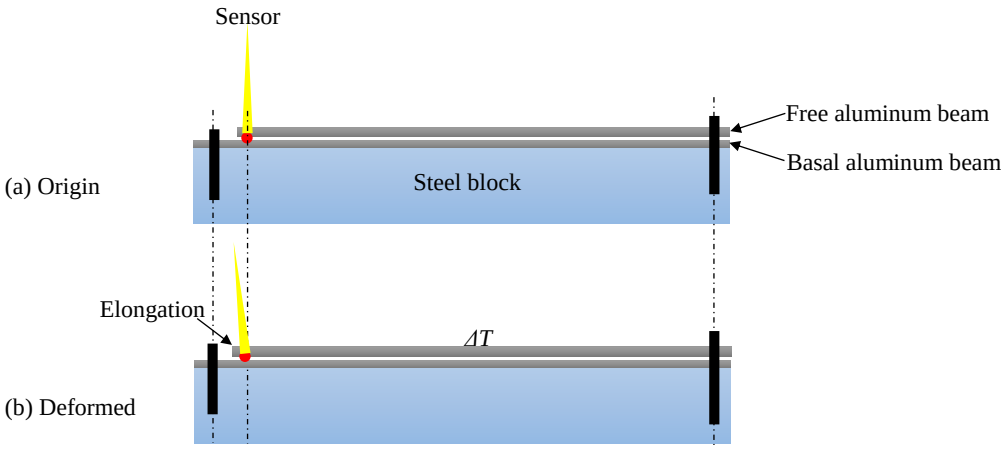

Figure 5.14 Ideal thermal deformation monitoring by the proposed sensor

5.6 Conclusions

A mechanical sensor is introduced to visualize a small thermal displacement by means of transforming the displacement into the movement of rotation at low cost. Two laboratory experiments were carried out to verify the feasibility of this method. Compared with the theoretical values in the first experiment, it could be found that the mechanical method offers an acceptable measurement of small displacement. For the experiment of thermal expansion, a much smaller displacement was detected and visualized by the mechanical sensor. Combined with other measurements by LVDTs and dial indicator, the deformation process of the designed structure in response to an increase in temperature is estimated. Therefore, it is possible to estimate the thermal axial force by just monitoring the same deformation using the proposed sensor. Because this sensor is sensitive to small displacement, it also has the probability to be applied to monitor the concrete cracks such as in the safety management of old tunnels.

References for Chapter 5

1. Brown M. E.: Introduction to thermal analysis, *Kluwer*, 2001
2. Standard specifications for tunneling -2006: Open cut, *JSCE*, 2006 (In Japanese)
3. Design of vertical shaft for shielding construction, *JSCE*, 2015
4. Kihara Osamu, Horigo Kazutaka and Takaya Tomokazu: Temperature stress of short strut subject to preloading, *51st proceedings of JSCE*, Vol.51(B), pp.420-421, 1996 (In Japanese)
5. Ishida Takahiro and Namikawa Kenzi: Behavior of Shaft Excavation with Concentrated Steel Strut, *The 37th Japan National Conference on Geotechnical Engineering*, Osaka, pp.1589-1590, 2002 (In Japanese)
6. Sakimoto Tatsuro: Structural mechanics, *Morikita Publishing*, 2007 (In Japanese)
7. Zhang H., Akutagawa S.: A mechanical method for monitoring and data-visualization of small deformations in underground structures, 9th International Symposium on Field Measurements in Geomechanics, Australia, Sydney, pp.329-338, 2015

CHAPTER 6: VISUALIZATION OF THE DIRECTION OF PRINCIPAL STRAIN

6.1 Introduction

Three mechanical methods for deformation monitoring have been introduced in the previous 3 chapters respectively in order for a direct understanding of the structure performances. Furthermore, for a comprehensive investigation into the mechanical properties of the structures, it is necessary to measure the local strain so that the corresponding stress can be deduced by using the elastic modulus. There have been various technologies developed for strain measurement. For example, in order to measure the inner strain of the reinforced concrete beam, the reinforcing bar stress transducers or strain gauges are applied. Generally, the surface strains are usually measured by the electrical strain gauges[1]. However, there exist the wiring works between the gauges and the data loggers, which makes it inconvenient during construction. Another notable Fiber Bragg Grating (FBG) optical sensing technology is able to obtain the strains at multiple points in the structure with less cables, while the spectrometers used to detect the wavelength shifts are expensive and complex[2-5]. A nondestructive method using magnetic anisotropy sensor is able to measure the stress or strain of the steel anchors directly but with a low degree of accuracy. The moiré effect can be alternatively used to measure the displacement or strain. The strain is determined by processing the moiré fringes, which are developed by superposing the reference fine gratings and the master gratings. The master gratings are usually fixed on the surface of the deformed objects. More specifically, the normal strain and shear strain can be obtained by using the moiré fringe analysis in terms of the uniform displacement and rotation. It is regarded as a promising visualization technique for strain monitoring for the simple optical setup and acceptable sensitivity[6-8].

The displacement is generally measured between two designated points on the surface of structure, and the strain at a point is defined as the derivative related to displacement. The state of stress, which is complicated under different loadings, is analyzed mainly by means of the measurement of strains. In order to know the strains in multi-directions, especially the principal strains at a point, it needs to measure the strains at least in three directions simultaneously. The digital photogrammetry technology has been developed to show a full-field strain vector contour by processing the image of the structures, such as

the Digital Image Correlation (DIC) method[9-11]. The accuracy of measurement is governed largely by the photographic distance, the intensity of illumination, the precision of the camera lens and so on. Hence it is difficult to achieve a high accurate measurement of surface strain in structures outdoors. Now an improved DIC method using the Line Scanner Camera is utilized to sense the strain in arbitrary direction at any point with a high level of accuracy. As the uniform light is provided by the affiliated light source near the scanner, the measurement can be carried out outdoors regardless of the ambient light. It, nevertheless, costs time to conduct the image analysis. The strain marker technique was introduced conceptually about 30years ago in order to determine the principle strain on a rock face directly[12-13]. It relied on the observation of the change in the objects of known shape and size, like a circle or ellipse. The size of the deformed marker is manually measured by ordinary methods. Furthermore, it is assumed that the strain marker has the same deformation property of the rock, to which the marker is attached. Because it is difficult to find the suitable marker in practice, the closeness of the strain of the marker and the measured rock should be discussed. Though there is little advancement in this technique for decades, its idea still has some inspiration and would be referred to in this chapter.

A simple method is proposed to visualize the direction of the principal strain in a domain of structure in real-time. The mechanism and key structures of the sensor is introduced. A model sensor is manufactured which works well as a demonstration. The main factors which influence the sensitivity of the visualization are analyzed. The fundamental experiments were conducted to verify the validity of the method. Finally, the improvement work is described briefly.

6.2 Determination of Principal Strain

In this chapter, the homogeneous strain is assumed within a considerable domain of the structure. The two-dimensional problem of strain is mainly dealt with for simplicity. The three-dimensional state of strain can be obtained by analyzing the strains in three orthotropic planes at a point. The state of plane strain is illustrated by Mohr circle as shown in Fig. 6.1. If at least three normal strains at A, B and D directions are measured under the loading condition, the principal strains can be calculated by several approaches.

It is known that the principal strains exist where the shear strains are zeros. The major principal strain represents the largest deformation in the same direction at that point. The measurement of strain is essentially the measurement of displacement. So, if the largest

(or smallest) relative displacement is identified, the major principal strain at a point can be determined accordingly, including the magnitude and orientation. The minor principal strain is thought to be of the perpendicular direction of the major principal strain.

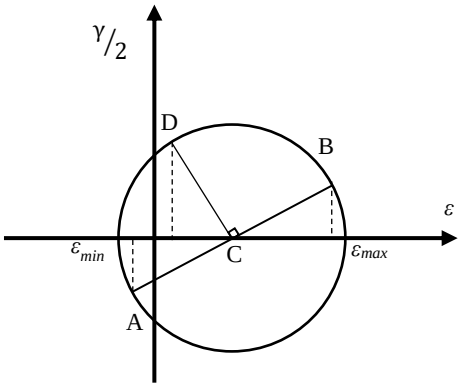

Figure 6.1 Mohr circle of strain

Let us consider a standard circle located on the surface of the structure in the state of homogeneous strain. When the structure is loaded in the elastic state, the circle would be deformed to an ellipse, which has been illustrated in Chapter 2. There shall be a longest distance between two points on the ellipse as shown in Fig. 6.2. If the longest distance is identified in the deformed configuration, the principal strain is supposed to be obtained, including the scalar and orientation. This chapter introduces a mechanical method for visualization of the direction of principal strains. This proposed method is quite different from the single strain gauge method or the three strain gauges method. The direction of principal strain is identified directly by finding the longest distance (major axis) automatically between two points along the circumference of ellipse zone.

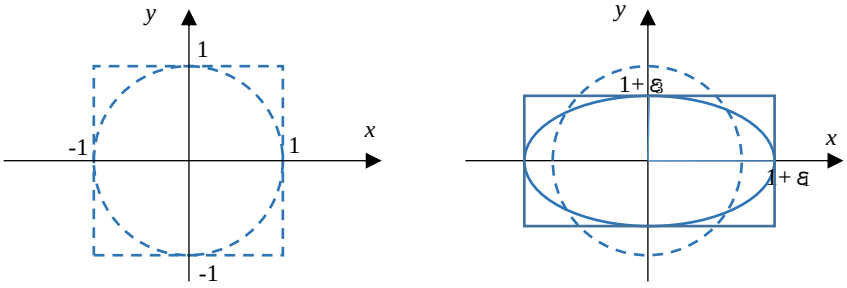

(a) Undeformed (b) Deformed

Figure 6.2 An ellipse deformed from a unit circle due to homogeneous deformation

6.3 Description of The Sensor

6.3.1 Components of the sensor

The mechanical sensor consists of two important members, as shown in Fig. 6.3. One is the ideal standard circular ring. It can be manufactured in advance. Then the ring is attached on the surface of structure, so that they would have the identical deformations under the loading condition, similar to the strain markers used in the measurement of rock strain. Alternatively, the ring can be formed directly on the surface of structure for monitoring by drilling a hole. The other is the extendable rod, with two pulleys on both ends. The extendibility is provided by the two springs installed along the piston rod between two cylinders. The extendable rod is assembled inside the ring by mounting the two pulleys along the rail track at the inner side of ring. Therefore, the extendable rod is able to rotate freely along the rail. It is noted that the extendable rod is designed to be symmetrical in order to reduce its self-weight effect during monitoring[15]. In this research, the sensor is aimed to visualize the orientation of principal strain automatically. The magnitude of principal strain is easy to obtain by applying the electrical function for measuring the change in length of the rotational rod finally.

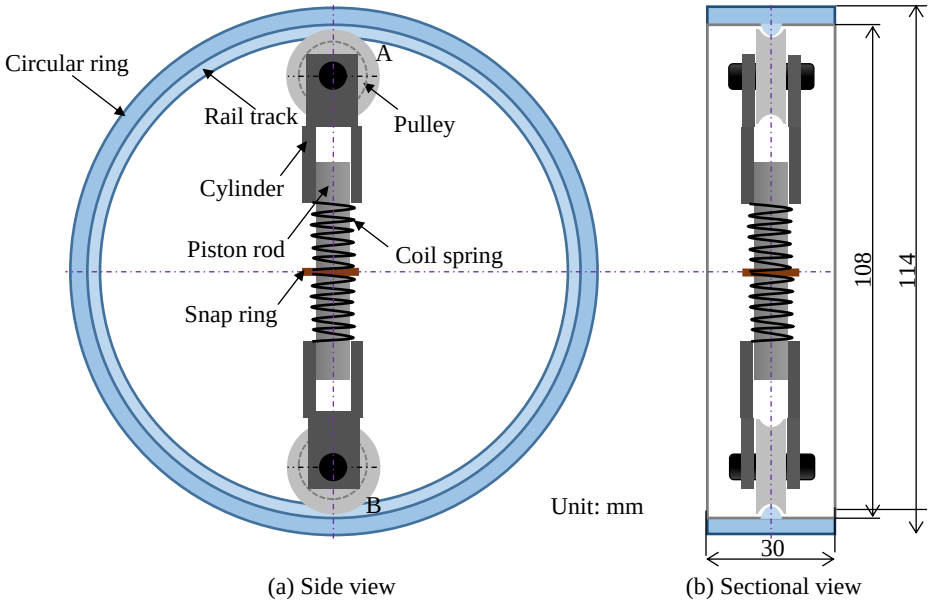

Figure 6.3 Layout of the sensor

6.3.2 Investigation into self-weight of rod

A sample of sensor is made in order to verify the feasibility of this idea to visualize the direction of principal strains as shown in Fig. 6.4. The gray circular ring is made of polyvinyl chloride (PVC, Young's modulus: 2800Mpa). The extendable rod is made up

of several elements, including two plastic pulleys. Two rods are prepared with different weights as in shown Fig. 6.4 (c) and Table 6.1.

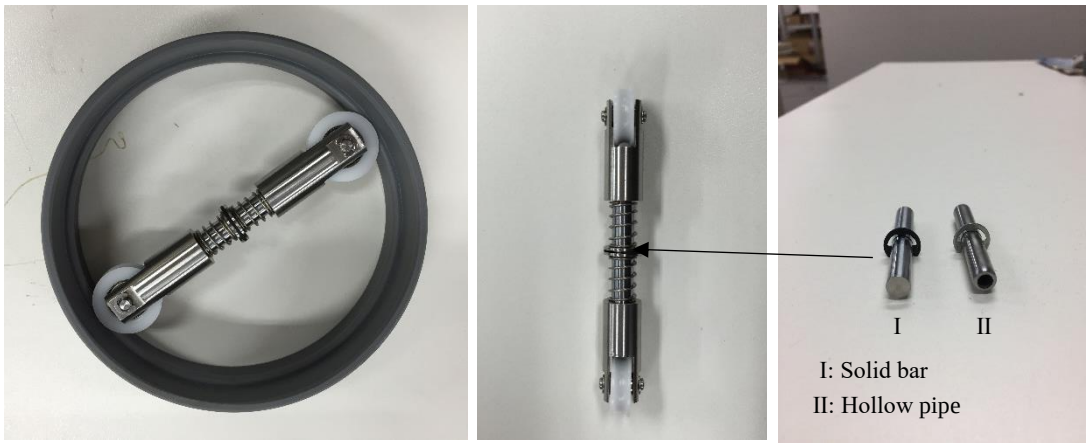

(a) Assembly of sensor (b) Extendable rod (c) Two kinds of piston rods

Figure 6.4 The sample of sensor

Table 6.1 Self-weight of the components of extendable rod

Component		Pulley	Piston rod	Cylinder	Coil spring	Snap ring	Washer
Sensor I	Weight [N]	0.051	0.196	0.250	0.007	0.004	0.008
	Quantity	2	1	2	2	1	2
	Total weight (N)	0.830 (84.69g)					
Sensor II	Weight [N]	0.051	0.114	0.250	0.007	0.004	0.008
	Quantity	2	1	2	2	1	2
	Total weight (N)	0.748 (76.36g)					

6.3.3 Investigation into friction

There are two kinds of frictions in the sensor. One is the rotational friction around the pulley axle as shown in Fig. 6.5 (a). The other is the rolling friction between the pulley and rail track. The pulley rotates by using the smooth balls which can roll freely between the inner and outer surface. The friction exists when the balls are rolling, though the oil or grease is used to reduce the friction. The friction torque of the pulley is investigated by means of a small experiment as shown in Fig. 6.5 (b). The wire is fixed along the groove of pulley, with two ends loaded by the weight of W_1 and W_2 respectively. At first, W_1 and W_2 are the same. Then, W_2 is increased by adding the water gradually. As the pulley starts to rotate, the experiment is finished. The rotational friction torque in this research is defined as the value when the pulley is mobilized to rotate from static under the loading.

As for sensor I, the experiment are conducted in four cases and the results are shown in Table 6.2 and Fig. 6.6. The weight of wire is negligible in the experiment. The load applied to the pulley is calculated by:

$$W_{load} = 2W_1 \tag{6.1}$$

where W_{load} is the load applied to the pulley, and W_1 is the weight conneted to the wire.

The friction torque is calculated by:

$$M_f = W_{water} \times r = (W_2 - W_1)r \tag{6.2}$$

where M_f is the rotational friction torque, W_{water} is the weight of water, r is the radius of pulley, W_1 is the weight connected to one end of wire, and W_2 is the weight connected to the other end of wire.

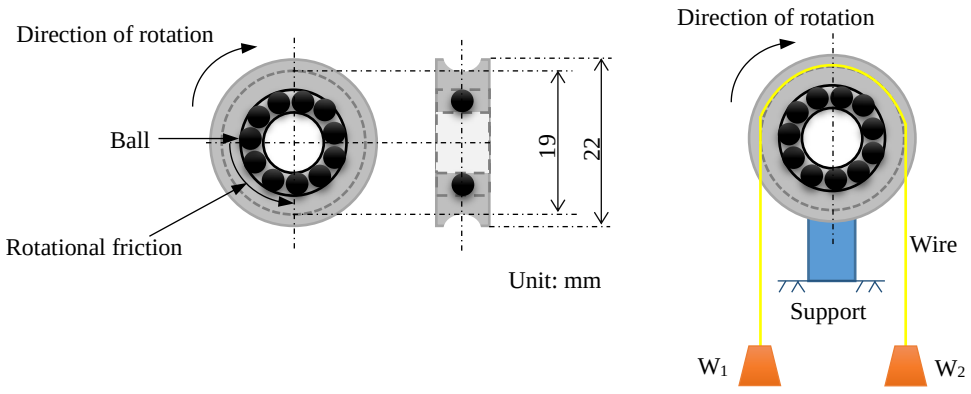

(a) Details of the pulley

(b) Experimental setup

Figure 6.5 Experiment for investigation of the rotational friction of pulley

From Fig. 6.6, it is also found that there exists the inherent friction of pulley even if there is no load applied to the pulley. The friction torque increases as the applied loads grow. The coefficient of rotatinal friction can be given by:

$$c_r = (M_f - 0.175)/(W_{load} \times r) \tag{6.3}$$

where c_r is the coefficient of rotational friction of pulley. Hence, c_r of this kind of pulley is about 0.00689.

To measure the rolling friction between the pulley and rail track is not an easy thing. It would be talked about by comparing three types of rings whose radius of rail tracks are 1.8mm, 2.0mm and 2.5mm respectively in section 6.6. What we can keep in mind is that the rolling friction has a linear proportional relationship with the applied load.

Table 6.2 Results of the experiment for investigation of the friction torque (sensor I)

Cases	W_1 [N]	W_{load} [N]	W_2 [N]	W_{water} [N]	M_f [N·mm]
Case1	0.75	1.49	0.78	0.03	0.28
Case2	1.36	2.71	1.39	0.04	0.34
Case3	1.96	3.92	2.00	0.05	0.44
Case4	2.56	5.12	2.61	0.05	0.51

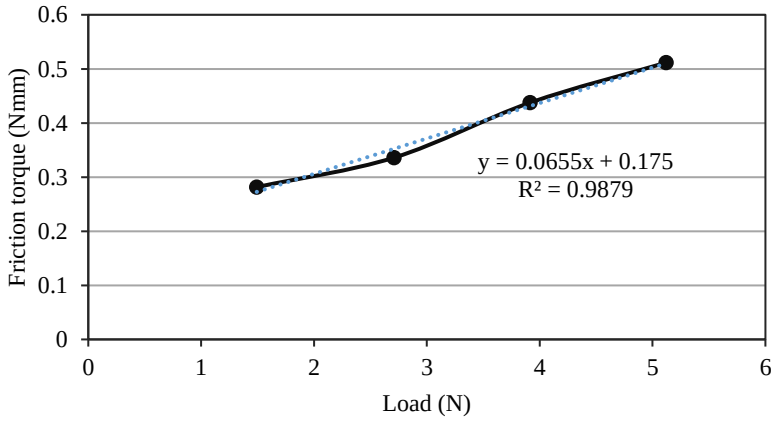

Figure 6.6 Relationship between the load and friction torque (sensor I)

6.4 Mechanism of the sensor

When the extendable rod is mounted inside the ideal circular ring, it can remain stable at any positions as shown in Fig. 6.7. The equilibrium equations including the resultant force and the moment of rod are expressed respectively as:

$$\sum F_i = 0 \tag{6.4}$$

$$\sum M_i = 0 \tag{6.5}$$

where F_i represents different force that occurs in the sensor, and M_i stands for different moment of rod.

In fact it is in the state of equilibrium, subjected to the self-weight of rod, resistance force against the ring, the force due to the spring and the frictions. In order for a better understanding of the mechanism of visualization during deformation, the analysis model is simplified without considering the friction and self-weight as shown in Fig. 6.8. The effect of friction and self-weight will be dealt with in section 6.6. It is assumed that there is just the contract but no rotation of extendable rod when the ring is deformed to be an ellipse. In addition, it is a symmetric system. Hence, the resultant force acting on the rod can be written as:

$$\sum F_i' = N' + F' = 0 \tag{6.6}$$

where *N'* is the resistance force against the ring after deforming, and *F'* is the spring force, which can be written as:

$$F' = k\delta l_0 = k(L - l) \tag{6.7}$$

where *k* is the spring constant 0.503N/mm, δl_0 is the compression of the spring, *L* is the free length 93mm of extendable rod between two axles, and *l* is the length of rod compressed in the ring.

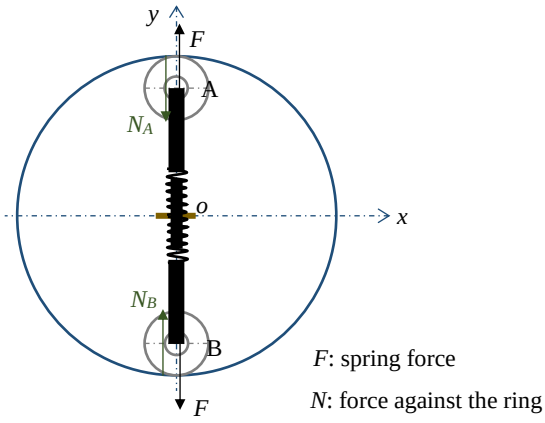

Figure 6.7 Initial state of the sensor

The moment of rod about O can be written as:

$$\sum M_i' = 2 \times (N' \times b) = 2N'b \tag{6.8}$$

where M_i' is the different rotational moment, *N'* is the resistance force against the ring after deforming, *b* is the distance from center O to the line of resistance force *N'*.

Then, the extendable rod is forced to rotate due to the moment. It would stop where the moment recovers to be zero. As for the ellipse shape after deforming, there is no positon but the major axis (longest) where there is no moment of the rod. So the extendable rod would stop at the major axis of ellipse, which shows the longest distance between two points around the circumstance of ring. The position of rod indicates the direction of one of principal strains. The direction of the other principal strain is orthogonal to the visualized direction.

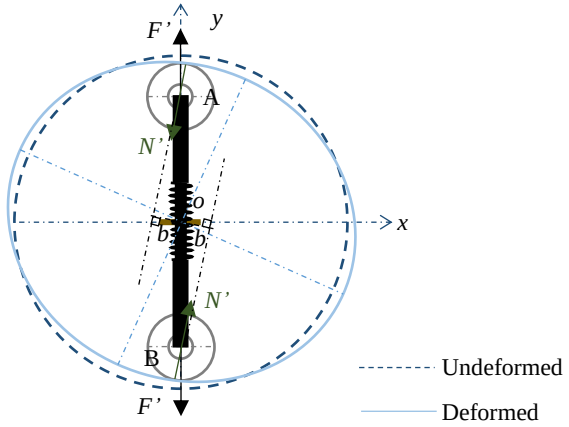

Figure 6.8 Ellipse derived from the circle assuming the rod stays in the same direction

6.5 Sensitivity and Accuracy Analysis

6.5.1 Effect of friction

Assuming that there are only frictions but no weight of the sensor, the analysis model can be regarded as symmetric, which allows analyzing half of the structure as shown in Fig. 6.9. For the pulley B, when the ring is in the deformed state, the moment about point B can be written as:

$$\sum M_i^B = F_B' \times d - M_f^B = F_B' d - M_f^B \tag{6.9}$$

where M_i^B is different moment about point B, F_B' is the spring force after deforming, d is the distance from point B to the line of F_B', and M_f^B is the rotational friction torque of pulley, which can be calculated by:

$$M_f^B = 0.0655 N_B' + 0.175 \tag{6.10}$$

which is the fitting formula obtained from Fig. 6.6. In Eq. (6.10), N_B', which is the load from the ring applied on the pulley B, can be assumed to be equal to F_B' approximately

as long as the deformation is very small. Then, substituting Eq. (6.10) into Eq. (6.9), we will have:

$$\sum M_i^B = F_B' d - (0.0655F_B' + 0.175) = F_B'(d - 0.0655) - 0.175 \qquad (6.11)$$

which shows the moment about point B is finally related to the spring force F_B' after deforming and the distance d from point B to F_B'. If the extendable rod is mobilized to rotate, we shall have $\sum M_i^B \geq 0$. The distance d can be written as:

$$\mathrm{d} \geq 0.175/F_B' + 0.0655 \qquad (6.12)$$

where 0.175 and 0.0655 are the values of inherent characteristics of pulley. The d denotes the deviation of the new contact point between the pulley and ring from the initial axis of extendable rod. It can be used as an index to the sensitivity of visualization of deformation. A small d indicates high sensitivity of the sensor. The relationship between d and F_B' is shown in Fig. 6.10 when the balance of rod is broken from static to motion. The larger spring force is, the smaller d can be. The theoretical minimum value of d is close to 0.0655mm, which is determined by the pulley.

It should be noted that, in fact, the resistance force N_B' against the ring, the rolling friction force f_B and F_B' need to satisfy the force equilibrium equations of pulley B.

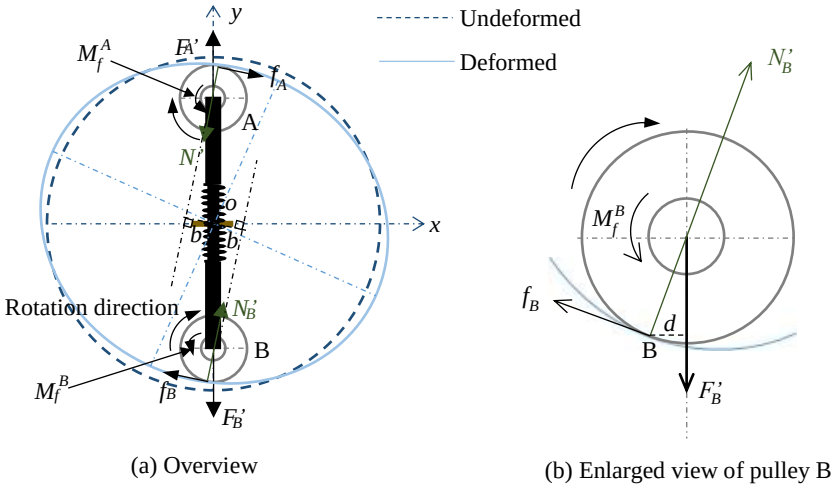

(a) Overview (b) Enlarged view of pulley B

Figure 6.9 Analysis model assuming no rotation of rod (in case of no weight)

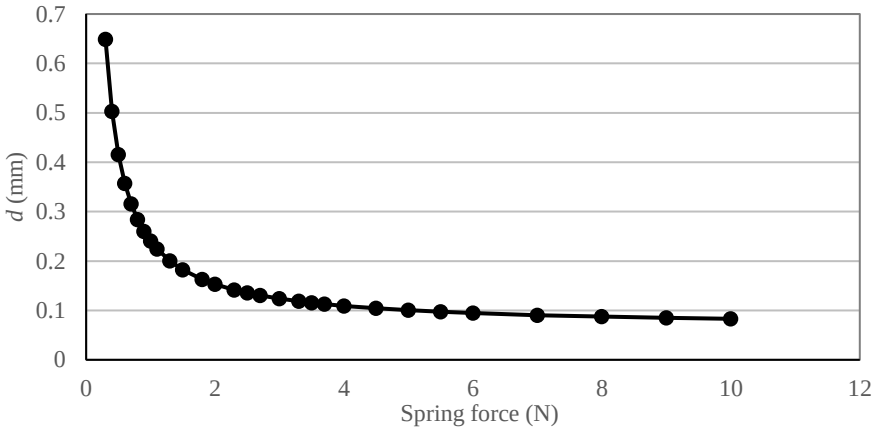

Figure 6.10 Relationship between the spring force F_B' and distance *d*

6.5.2 Effect of radius of pulley

The size of pulley also has effect on the sensitivity of deformation visualization. Taking pulley B again for example, as shown in Fig. 6.11, different size of pulley results in different distance *d*, under the condition of same deformation. Some assumptions should be noted here. The extendable rod is only compressed without rotation. The spring forces corresponding to different sizes of pulleys are the same after deformation. Therefore, we will find that in Fig. 6.11, since:

$$r_1 > r_2 \tag{6.13}$$

we can get:

$$d_1 > d_2 \tag{6.14}$$

where r_1 is the large radius of larger pulley, r_2 is the radius of smaller pulley, d_1 is the distance from B_1 to the line of spring force, and d_2 is the distance from B_2 to the line of spring force. In addition, B_1 is the contact point between larger pulley and the ring, B_2 is the contact point between smaller pulley and the ring.

If the pulley is located at a smooth curve with a short length after deforming, where the curvatures are approximately constant, the relationship between *r* and *d* can be written as:

$$\frac{d_1}{d_2} = \frac{r_1}{r_2} \tag{6.15}$$

which means that the resistance forces (N_{B1}' and N_{B2}') against the two kinds of pulleys

are nearly parallel.

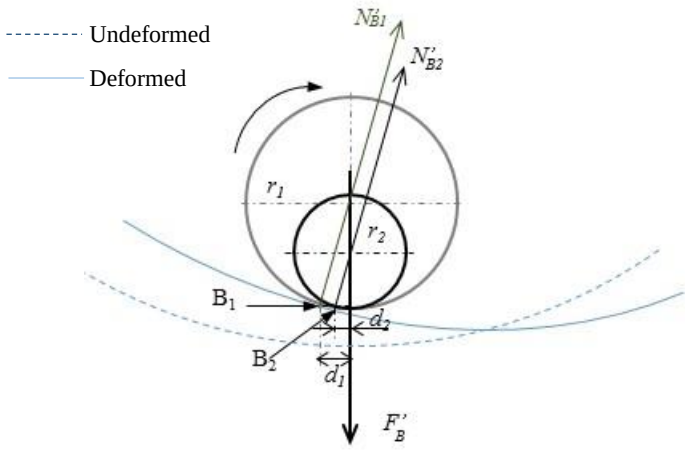

Figure 6.11 Comparison of reaction of different sizes of pulley under the condition of same deformation

6.5.3 Effect of self-weight of rod

The self-weight of extendable rod is another important factor to be considered in the sensitivity and accuracy analysis of visualization. It affects the resistance forces against the ring on both ends of the rod, depending on the status of the plane of ring (horizontal or vertical) as shown in Fig. 6.12. In Fig. 6.12 (a) when the ring is horizontally set up, the self-weight would mainly affect the rolling friction of the sensor, with little influence on the resistance forces against the ring. In such a case, the symmetry of the structure can be utilized and the self-weight can be omitted in the sensibility analysis. When the rod is placed inclined in the vertical ring as shown in Fig. 6.12 (b), the forces against the ring at points A and B would be influenced by the self-weight of rod, which should be taken into consideration. Because of the self-weight, there is a deviation of the extendable rod from the center of the ring, no matter what the ring is, a circle before deforming or an ellipse after deforming.

Since the sensor is designed to visualize the direction of principal strain after deformation, the effect of self-weight of rod would be analyzed in an ellipse after deformation as shown in Fig. 6.13. The analysis would be carried out based on sensor I.

(a) Ring laid horizontally

(b) Ring laid vertically

Figure 6.12 Status of the ring

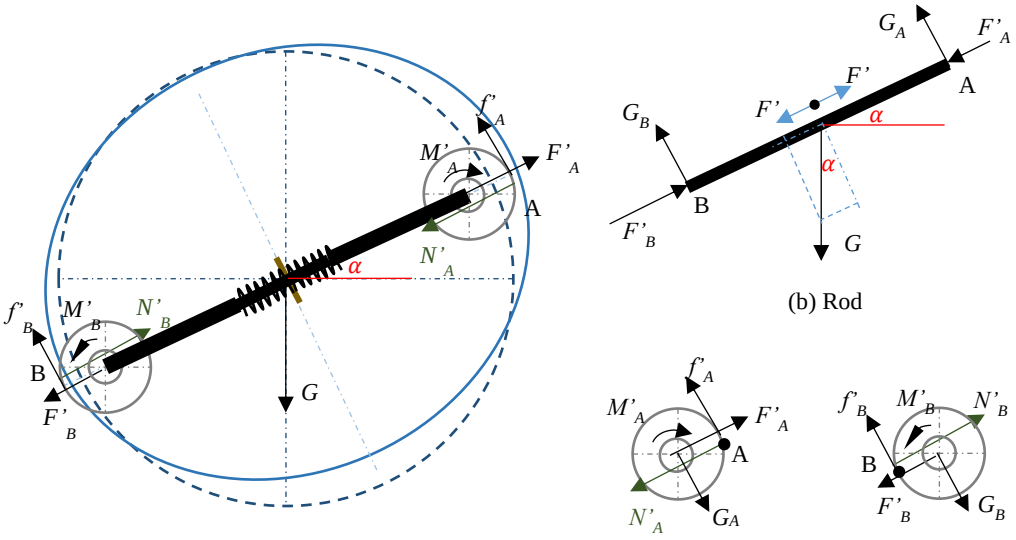

(a) Analysis model in an ellipse

(b) Rod

(c) Pulley A

(d) Pulley B

Figure 6.13 Analysis model in the vertical plane considering the total weight of rod

When the extendable rod is set up inclined at an angle of α as shown in Fig. 6.13 (a), supposing that the rod goes through the center O in a state of balance, from Fig. 6.13 (b), we can have:

$$G_A = G_B = 0.5G\cos\alpha \tag{6.16}$$

$$F'_A = F' - 0.5G\sin\alpha \tag{6.17}$$

$$F'_B = F' + 0.5G \sin\alpha \tag{6.18}$$

$$F'_B - F'_A = G \sin\alpha \tag{6.19}$$

$$F'_B > F'_A \tag{6.20}$$

where $\alpha \in [0, 90°]$ is the inclination angle of rod, which also means the direction of major axis of ellipse, G_A and G_B is the support force from axle of pulley A and B respectively, normal to the rod, F' is the spring force, F'_B is the acting force against the ring at point B, and F'_A is the acting force against the ring at point A.

As for pulley A in Fig. 6.13 (c), the moment against point A can be written as:

$$\sum M_i^A = G_A \times r - M'_A > 0 \tag{6.21}$$

For pulley B in Fig. 6.13 (d), the moment against point B can be written as:

$$\sum M_i^B = G_B \times r - M'_B > 0 \tag{6.22}$$

From Inequality (6.20), it is known that:

$$M'_B > M'_A \tag{6.23}$$

Therefore, it is found that both pulley A and B cannot remain stable due to the unbalanced moment on this hypothesis. The extendable rod would have to go down to gain new balance. From Inequalities (6.20) and (6.23), it is shown that pulley B would regain its balance earlier than pulley A.

Another assumption is made that the extendable rod would stay in a new position parallel to its initial direction when pulley B gets balanced as shown in Fig. 6.14. In Fig. 6.14, h is the deviation of rod from the center of ellipse.

As for the rod, the moment against A can be expressed as:

$$N'_B l_{NB} + f'_B l_{fB} = G l_G^A \tag{6.24}$$

where N'_B is the resistance force against the ring at point A, l_{NB} is the arm of force N'_B, f'_B is the friction force at point B, G is the self-weight of rod, and l^A_G is the arm of self-weight of rod from point A.

As for pulley B, the moment against its axle can be expressed as:

$$f'_B \times r = M'_B = 0.0655N'_B + 0.175 \tag{6.25}$$

In Fig. 6.14 (c), the moment of pulley B against point B can be expressed as:

$$G_B r \cos\beta = F'_B r \sin\beta + M'_B \tag{6.26}$$

where β is the intersectional angle between the N'_B and the rod.

Therefore, from Eqs. (6.16), (6.18), and (6.24)~(6.26), β, f'_B and N'_B can be calculated. Furthermore, the deviation h of the rod can be gained.

The balance equation of force for the rod can be written as:

$$N'_B \sin(\alpha+\beta) + f'_A \cos(\alpha-\beta) + f'_B \cos(\alpha+\beta) = N'_A \sin(\alpha-\beta) + G \tag{6.27}$$

$$N'_B \cos(\alpha+\beta) = f'_A \sin(\alpha-\beta) + f'_B \sin(\alpha+\beta) + N'_A \cos(\alpha-\beta) \tag{6.28}$$

From Eqs. (6.27) and (6.28), N'_A and f'_A can be calculated.

As for the pulley A in Fig. 6.14 (b), its moment against the axle can be checked as:

$$f'_A \times r > M'_A = 0.0655N'_A + 0.175 \tag{6.29}$$

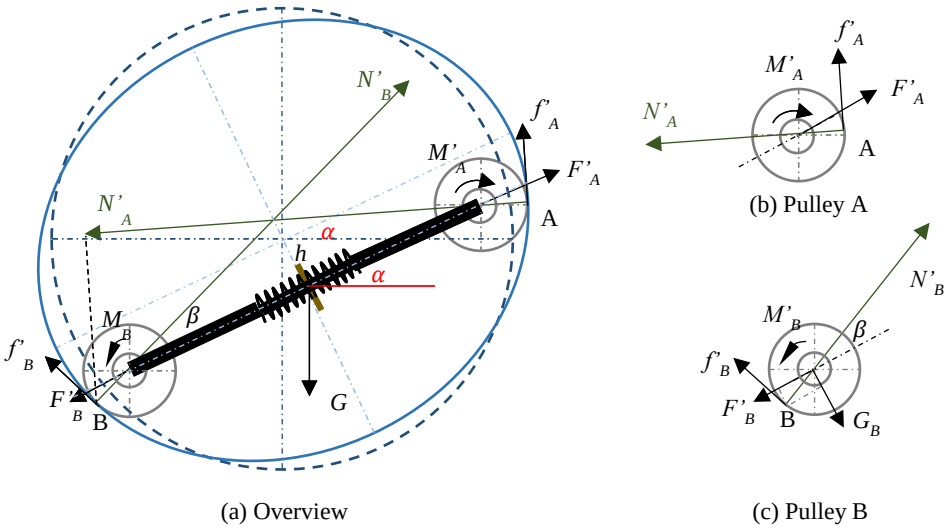

Figure 6.14 New position of rod when pulley B gets balanced

It is found that pulley A is not in a stable state. Hence, the rod would have to go down at the end of A until the pulley A regains balance, while its end B remains still as shown in Fig. 6.15. In Fig. 6.15, we define that:

$$\Delta\alpha = \alpha - \alpha' \tag{6.30}$$

where α' is the new inclination angle of rod after the pulley A gains balance, and $\Delta\alpha$ is the change in inclination angle of rod.

As for pulley A, the moment against its axle can be written as:

$$f_A' \times r = M_A = 0.0655N_A' + 0.175 \tag{6.31}$$

The moment against point A can be expressed as:

$$f_A' \times r + F_A' \times r \sin\beta' = G_A \times r \cos\beta' \tag{6.32}$$

where β' is the new intersectional angle between N'_A and the rod.

As for the rod, the moment against point B can be expressed as:

$$N_A' l_{NA} + f_A' l_{fA} = G l_G^B \tag{6.33}$$

From Eqs. (6.17), (6.31) ~ (6.33), β', f'_A and N'_A can be calculated. Then, the new inclination angle α' can be calculated.

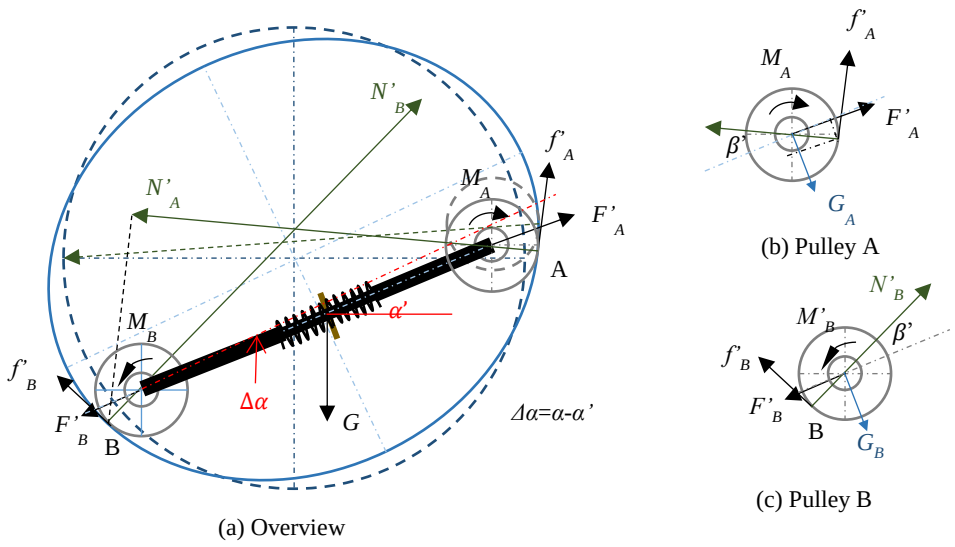

Figure 6.15 New position of rod when both pulley A and B get balanced

Meanwhile, the new $f_B'^*$ and $N_B'^*$ can be calculated.

As shown in Fig. 6.15 (c), the moment of pulley B can be checked.

$$f_B'^* r < 0.0655 N_B'^* + 0.175 = M_B' \tag{6.34}$$

In this case, pulley B is in a stable state, and we can have:

$$M_B' = f_B'^* r \tag{6.35}$$

In a mathematical simulation, the circle (its diameter is 104mm) is deformed to be an ellipse (the length of major axis is 106mm, the length of minor axis is 102mm). The error ζ of the inclination angle α is defined as:

$$\zeta = (\Delta\alpha/\alpha) \times 100 \tag{6.36}$$

The relationship between the error and inclination angle is shown in Fig. 6.16. There is a sudden change of the error when the angle α increases from zero (the rod is in a horizontal direction). It is found that the error decreases as the inclination angle becomes larger and larger. Since the value of error is very small, it can be regarded that the rod has a deviation from the center of ellipse due to self-weight, while the direction of rod is the same as the initial. It also indicates that the accuracy of visualization of the direction of principal strain is acceptable by using this method.

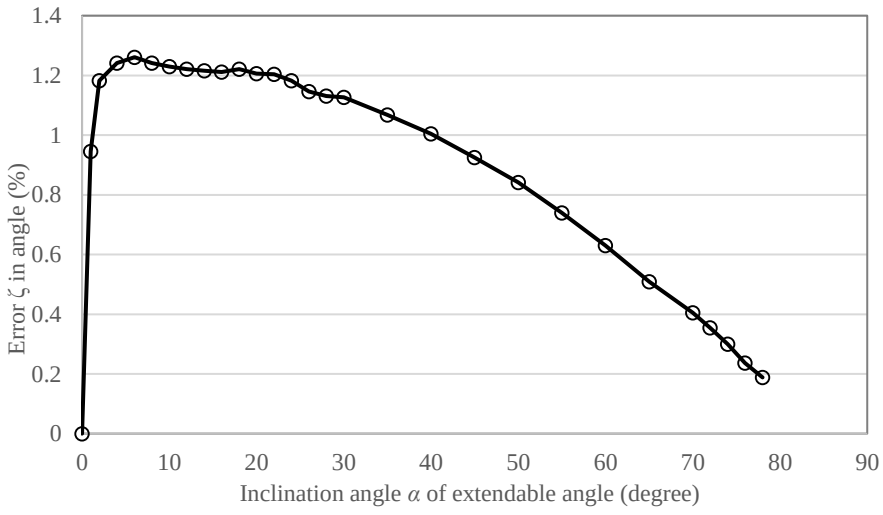

Figure 6.16 Relationship between the error ζ and inclination angle α of rod

Fig. 6.17 shows the relationship between inclination angle α of rod and the deviation h of extendable rod. As the angle of inclination of rod increases, its deviation decreases obviously. The maximum deviation h occurs when the rod is placed horizontally.

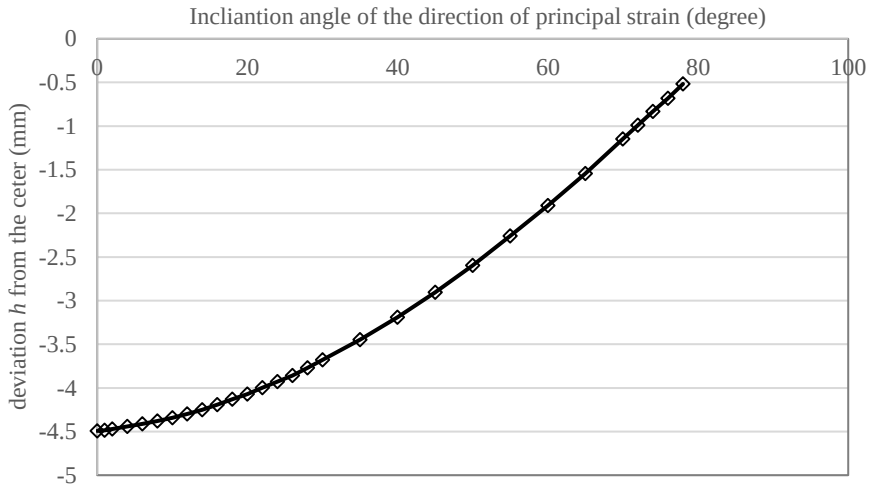

Figure 6.17 Relationship between the inclination angle α and the deviation h of rod

The weight of extendable rod has effect on the deviation h of rod too as shown in Fig. 6.18. The deviation h of rod decreases linearly in accordance to the reduction of its weight. If the weight is reduced to 0.3N, the deviation h of rod would be about 1.44mm. It is suggested that the reduction of the weight of rod is a feasible choice in order to reduce the deviation of rod from the center.

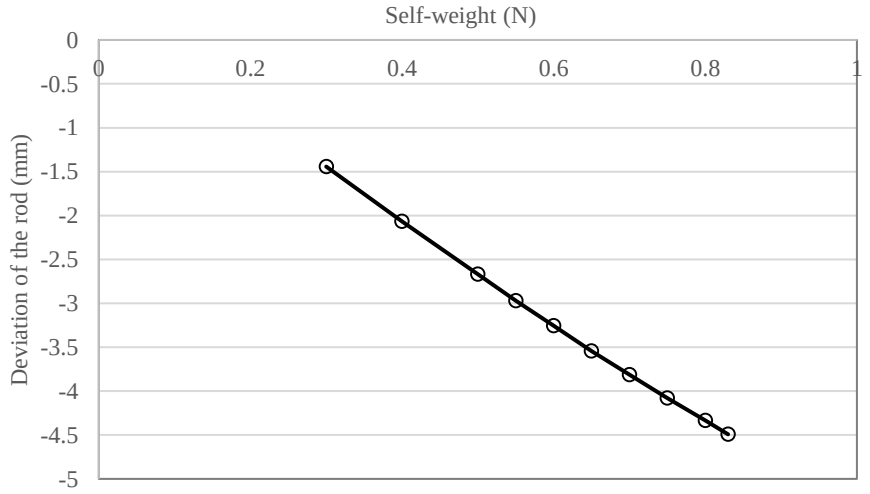

Figure 6.18 Relationship between the weight of rod and its deviation h

Fig. 6.19 shows the relationship between the spring constant *k* and the derivation *h* of the extendable rod. The deviation of rod decreases when the spring constant increases. The deviation can be reduced by increasing the spring constant. However, the effect becomes weaker as the spring constant increases. It is not suggested to use the spring with a larger spring constant because it might have an influence of the monitored object.

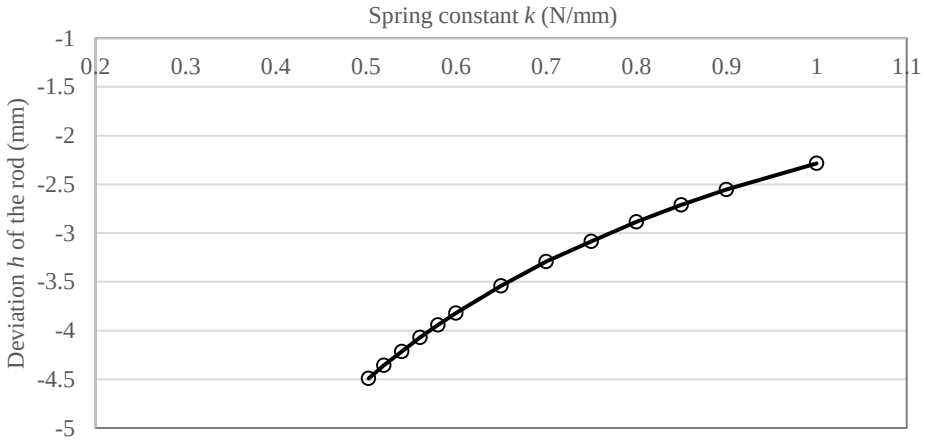

Figure 6.19 Relationship between spring constant *k* and deviation *h* of rod

The deviation of the extendable rod from the center is inevitable during the visualization of magnitude of principal strain because of the existence of the weight of rod. But the effect of self-weight of rod has little effect on the visualization of the direction of principal strain. The deviation of the extendable rod can be reduced by means of the lighter weight of rod or the stronger spring. The rod contains steel and plastic components. The light material or smaller size can result in light weight of the rod. There is still the limit due to the current manufactory techniques. Another approach is to use strong spring, which is very effective. However, in order for an accurate visualization of the principal strain, it is not suggested to increase the spring constant, because the large spring force acting on the ring might change the loading situation of the monitored zone.

6.6 Fundamental Experiments

6.6.1 Experiment design

Three types of rings of same diameters are designed to evaluate the sensitivity of the sensor in terms of different size of rail tracks as shown in Fig. 6.20. Their inner radii are the same of 52mm. The rolling friction between the rail and pulley shall be investigated by comparing the response of the three kinds of rings. Two kinds of rod of different self-

weight (sensor I and II) were tested in the experiments.

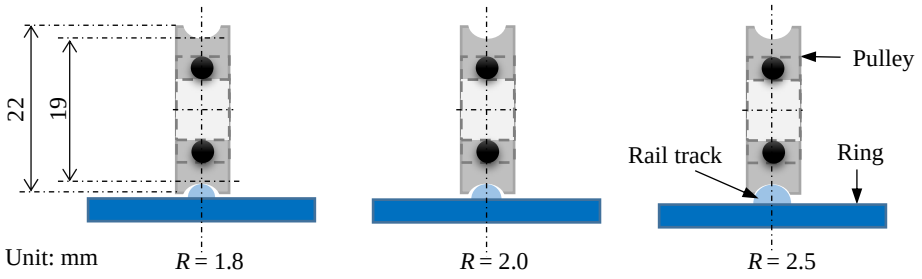

Figure 6.20 Three rings with different radii of rail tracks

The simple uniaxial compression tests were carried out as shown in Fig. 6.21. The ring is set up vertically on the platform of the test equipment. The load is applied directly on the top of the ring at point C_{90}. For each ring, the extendable rod is positioned with an inclination angle α, which shall be 30°, 45° and 60°. The displacements including the vertical displacements at point C_{90}, horizontal displacements at points C_{30} and C_{180} are measured by four LVDTs respectively while the loads are gradually increased. In fact, the vertical displacement at point C_{90} is the average of the two values measured by the two LVDTs at two sides of the ring under the lower surface of movable head. The test would be terminated as the extendable rod starts to rotate.

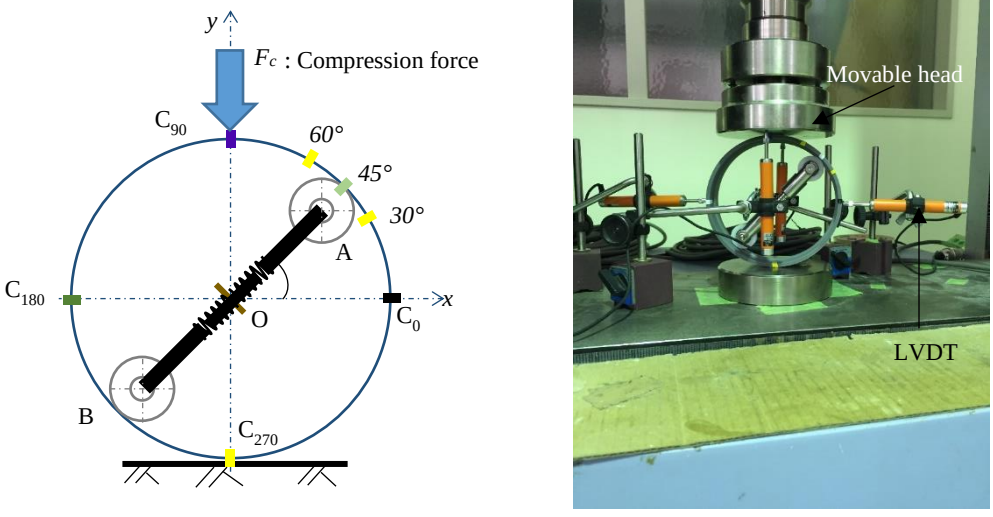

(a) Experiment layout

(b) Photo of experiment

Figure 6.21 Uniaxial compression test (sensor I)

6.6.2Result analysis

As the load is applied at the top of the ring, the ring is deformed to ellipse. Therefore, the line of C_0 and C_{180} would be the major axis of the ellipse, and the distance between C_0 and C_{180} would be the longest in the ellipse. The inclined rod is theoretically supposed to rotate to be horizontal. In fact, the rod just reacted as expected as shown in Fig. 6.22. Figs. 6.23~6.25 show the relationship between displacements and loads before the rod starts to rotate in case of the radius 1.8mm of rail track. The horizontal displacement is defined as the average of relative displacements of point C_0 and C_{180}. It is found that the displacements increases linearly as the growing loads are applied. The maximum vertical displacement of 0.92mm is needed to mobilize the rod when the inclination angle α is 30°.

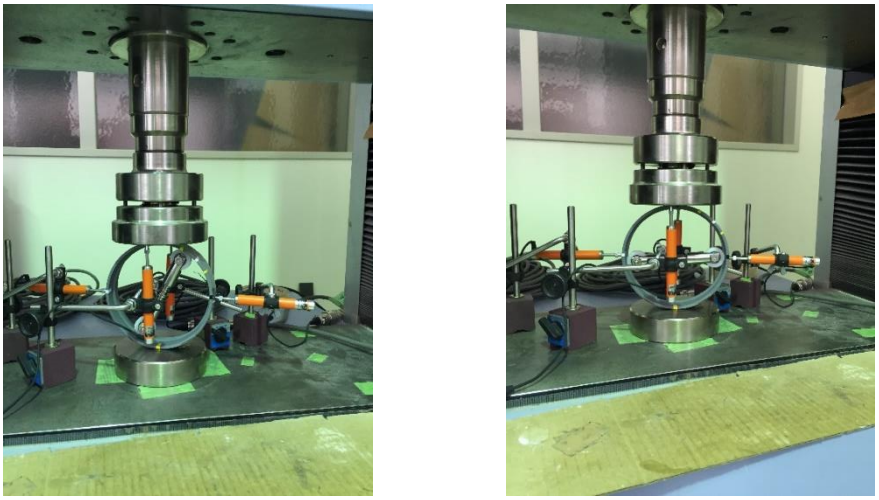

(a) Before Loading (b) After loading

Figure 6.22 Rotation of the rod (sensor I: R=1.8mm, α=60°)

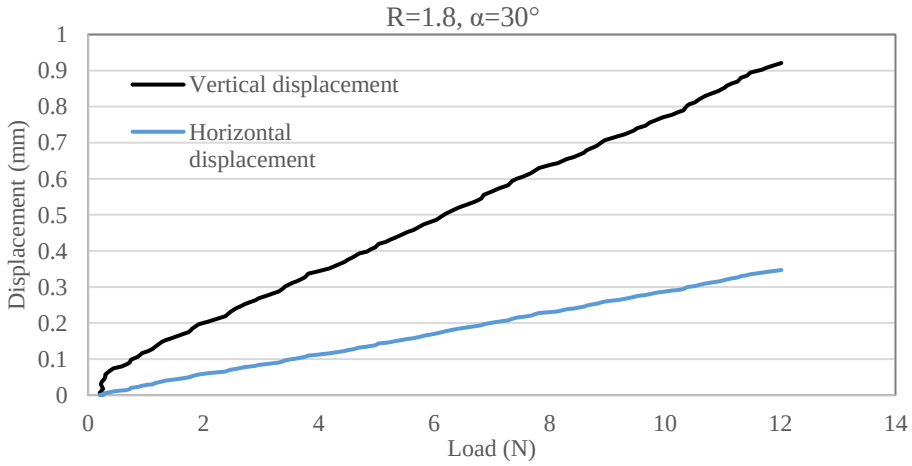

Figure 6.23 Displacements grow with the increase of loads (sensor I: R=1.8mm, α=30°)

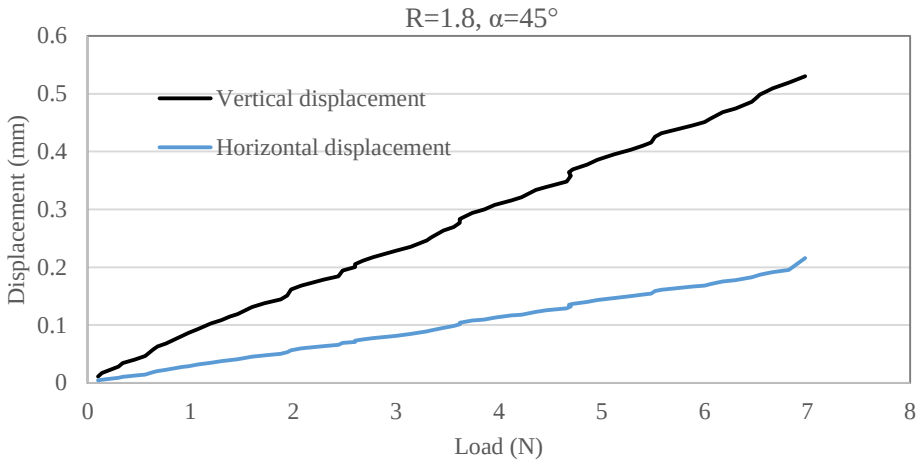

Figure 6.24 Displacements grow with the increase of loads (sensor I: R=1.8mm, α=45°)

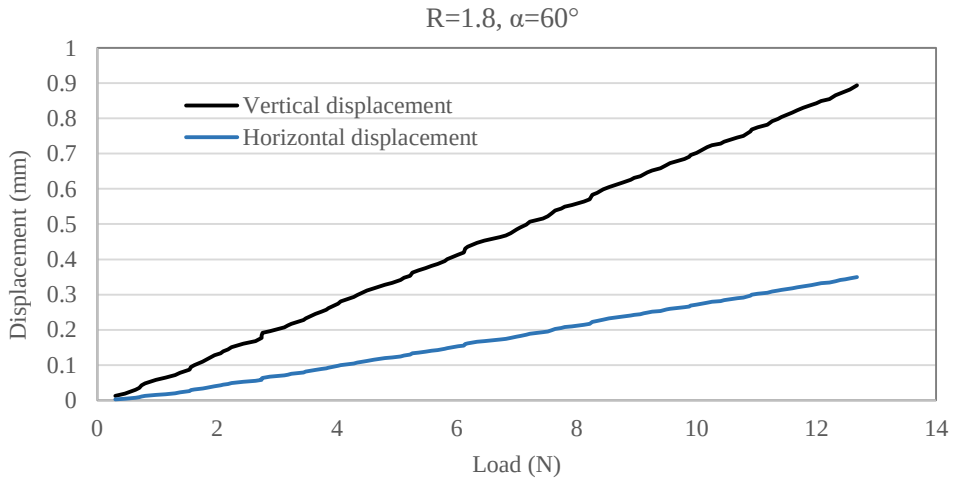

Figure 6.25 Displacements grow with the increase of loads (sensor I: R=1.8mm, α=60°)

Figs. 6.26~6.28 show the relationship between displacements and loads before the rod starts to rotate when the radius of rail track is 2.0mm. The response of the sensor is similar to that of the sensor with the rail radius of 1.8mm. The maximum vertical displacement of 1.67mm is required to make the extendable rod rotate when the inclination angle α of rod is 30°.

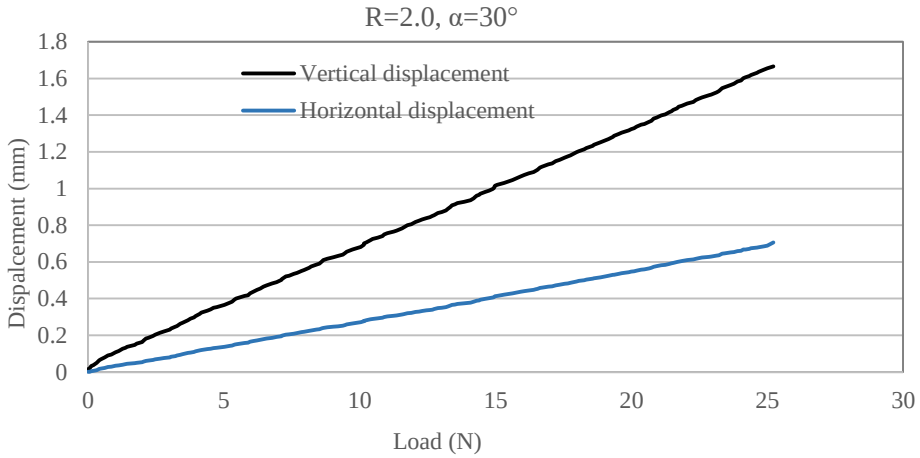

Figure 6.26 Displacements grow with the increase of loads (sensor I: R=2.0mm, α=30°)

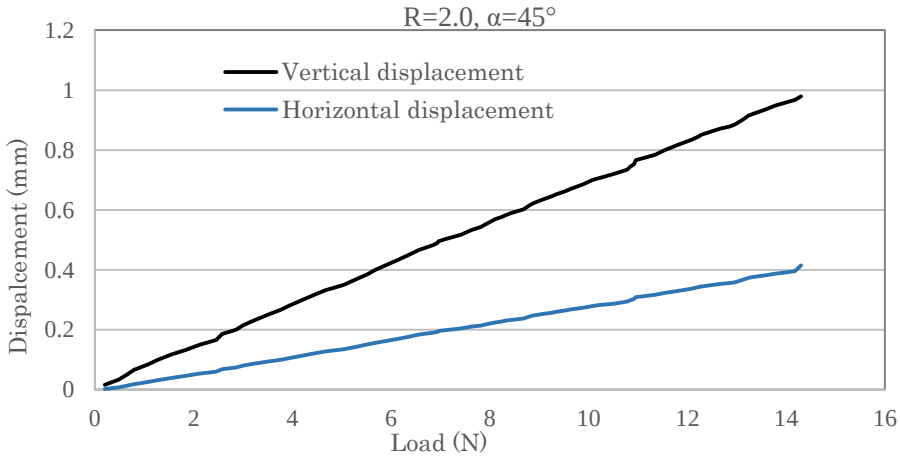

Figure 6.27 Displacements grow with the increase of loads (sensor I: R=2.0mm, α=45°)

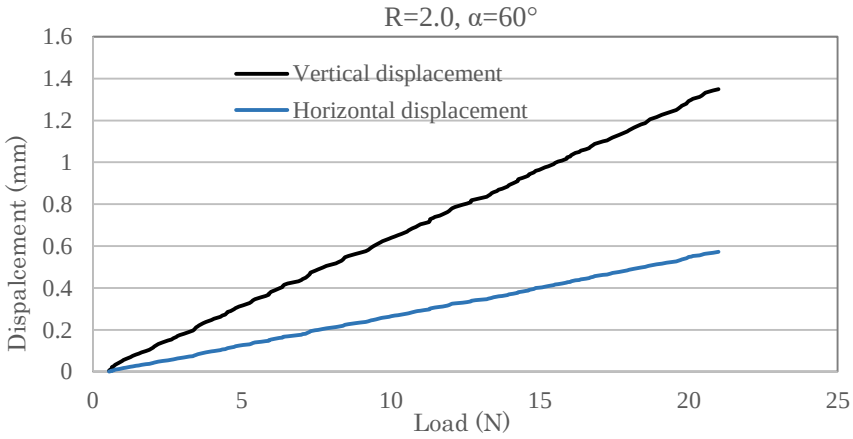

Figure 6.28 Displacements grow with the increase of loads (sensor I: R=2.0mm, α=60°)

Figs. 6.29~6.31 show the relationship between displacements and loads before the rod starts to rotate when the radius of rail track is 2.5mm. The maximum vertical displacement of 0.66mm is required to motivate rod when the inclination angle α is 30°.

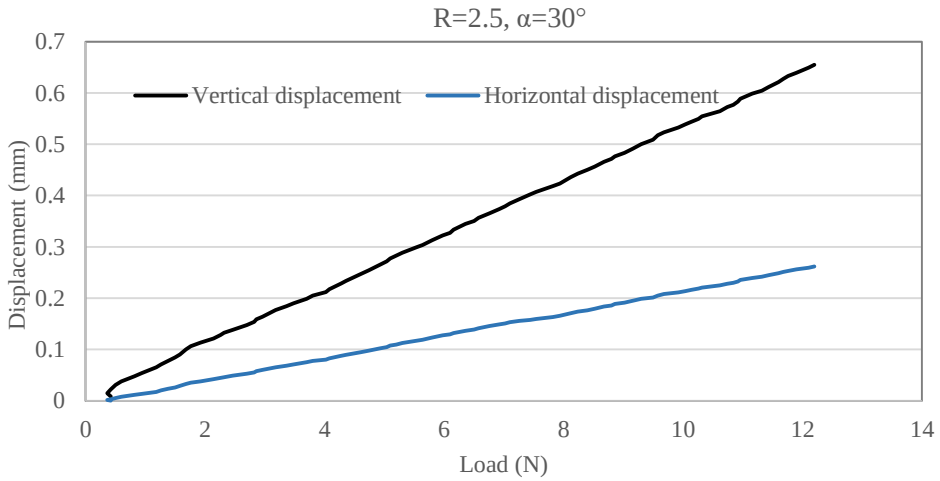

Figure 6.29 Displacements grow with the increase of loads (sensor I: R=2.5mm, α=30°)

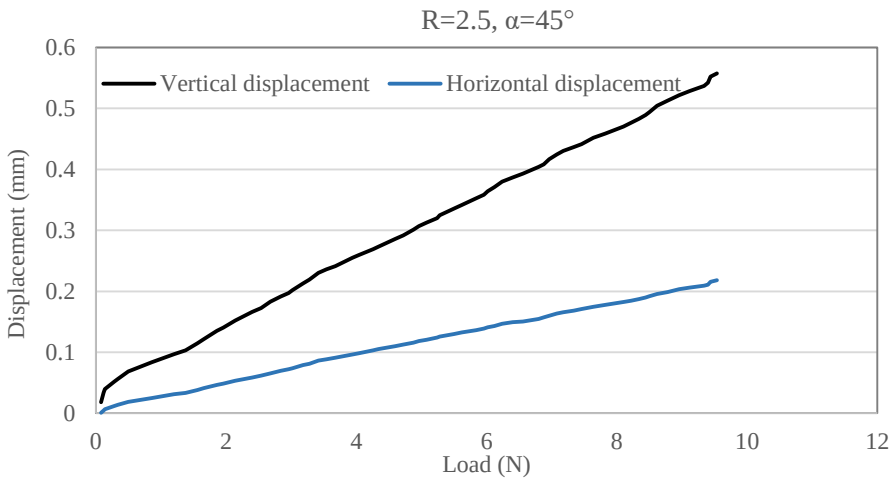

Figure 6.30 Displacements grow with the increase of loads (sensor I: R=2.5mm, α=45°)

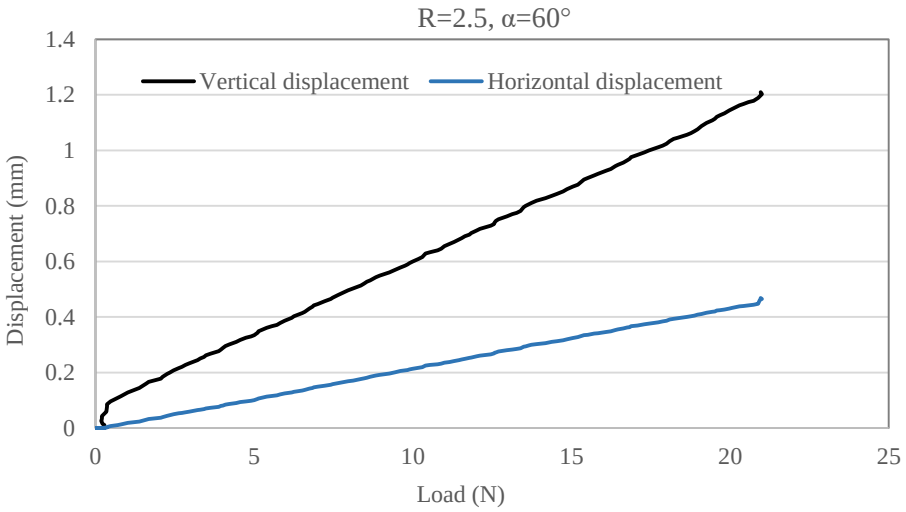

Figure 6.31 Displacements grow with the increase of loads (sensor I: R=2.5mm, α=60°)

The maximum displacements required for mobilization of the two kinds of rods are summarized in Tables 6.3 and 6.4 respectively. The λ is the ratio of the horizontal displacement to vertical displacement. As for sensor I, λ is in the range of about 0.38~0.42. For sensor II, λ is in the range of 0.33~0.42. Fig. 6.32 shows the relationship between inclination angle of rod with the self-weight of 0.83N and maximum required vertical displacement in terms of different rail radius. The maximum displacement is about 1.67mm when the rod is set up with an inclination angle of 30° in the ring with the rail radius of 2.0mm. In another word, a minimum deformation of 1.67mm in the zone of the ring can assure the mobilization of the rod. Furthermore, the sensitivity of this kind of sensor with the rail track radius of 2.0mm can be regarded as 1.67mm. Fig. 6.33 shows the relationship between inclination angle of rod with the self-weight of 0.75N and maximum vertical displacement in terms of different rail radius. The maximum vertical displacement required for mobilizing the rod is 1.09mm when the inclination angle α is 30°.

It is found that the sensitivity of the sensor can be improved by reducing the weight of rod. But it is difficult to judge different radius of rail track has obvious effect on the sensitivity of the sensor. From Figs. 6.32 and 6.33, since the effect of inclination angle of rod was investigated in three cases, it is also difficult to conclude that the initial inclination angle of rod has clear effect on the sensitivity of the sensor.

Table 6.3 Summary of the results of compression tests (sensor I)

R [mm]	Angle α [°]	Required Displacement [mm]		λ=H/V
		Vertical	Horizontal	
1.8	30	0.92	0.35	0.38
	45	0.53	0.21	0.40
	60	0.89	0.35	0.39
2.0	30	1.67	0.71	0.42
	45	0.98	0.42	0.42
	60	1.35	0.57	0.42
2.5	30	0.66	0.26	0.40
	45	0.56	0.22	0.39
	60	1.21	0.47	0.39

Table 6.4 Summary of the results of compression tests (sensor II)

R [mm]	Angle α [°]	Required Displacement [mm]		λ=H/V
		Vertical	Horizontal	
1.8	30	0.53	0.21	0.40
	45	0.43	0.16	0.37
	60	0.86	0.29	0.34
2.0	30	1.09	0.42	0.39
	45	1.00	0.41	0.41
	60	0.89	0.37	0.42
2.5	30	0.76	0.28	0.37
	45	0.45	0.15	0.33
	60	0.67	0.27	0.41

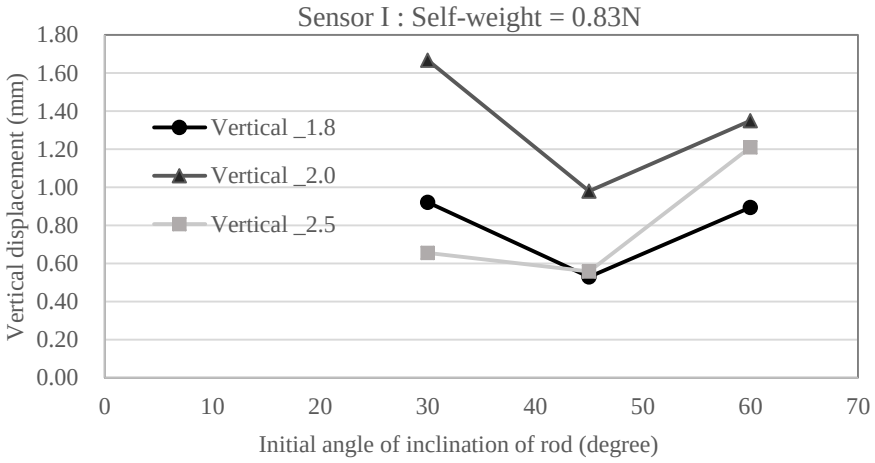

Figure 6.32 Relationship between the inclination angle α and displacement (sensor I)

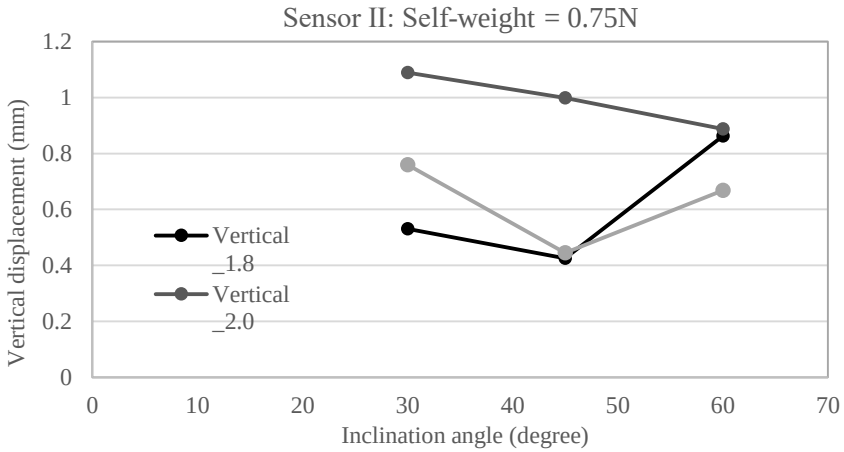

Figure 6.33 Relationship between the inclination angle α and displacement (sensor II)

6.7 Future Work

6.7.1 Improvement for higher sensitivity and accuracy

The simple compression tests have shown the possibility of this kind of sensor for visualization of direction of the longest axis of the ellipse. As for the measurement of strain including its magnitude, a high sensitivity of sensor is necessary. Taking the sensor model (R=2.0mm) in the uniaxial compression test for example, the required deformation which is quite possible to be sensed by sensor II is about 1.09mm. Hence, the compressive strain can be written as:

$$\varepsilon = {}^{\Delta y}/_{y_0} = \frac{1.67mm}{104mm} = 0.01048 = 10480 \times 10^{-6} = 10480\mu \qquad (6.37)$$

where ε is the compressive strain, Δy is the change in length, y_0 is the length of the rod set up in the ring before deforming, and μ is the resolution of strain measurement.

As for the steel generally used in construction in the yielding state, the yielding point strain would be around $1000\mu\varepsilon$[1]. There would be no response of the sensor set up on the steel structure to visualize the principal strain, even though the steel is yielded. Therefore, in order to visualize the principal strain in practice, the sensor should be improved to be able to react under much smaller deformation.

There are several approaches to improve the sensitivity of the sensor, such as lighter weight of extendable rod, elimination of the rotational friction of pulley, stronger spring and so on. The most practicable is to reduce the weight of rod as light as possible and to use the pulleys with a larger diameter. As a result, the deviation of rod can be reduced at the same time. Since the deviation of the rod can be estimated in advance, it is possible to modify the visualized result by compensating the inherent error of the sensor so that the accuracy of visualization of principal strain can be improved.

6.7.2 A simply supported beam experiment

A simply supported beam experiment is to be conducted to verify the feasibility of the sensor. The material of beam is PVC, same as the ring used as the model. The tests in section 6.6 have shown that the radius of rail track in the ring has not obvious effect on the sensitivity of the sensor. So in the new experiment, the radius of rail track is designed as 2.0mm, a medium value. The sensitivity of the sensor II (R=2.0mm) is about 1.09mm in compression. One aim of the improvement of sensor is to increase the sensitivity to less than 0.5mm in compression. By using the improved sensor, the loading experiment is designed as shown in Fig. 6.34. Four cylindrical holes, whose sizes are same as the sample ring, are drilled directly on the side of the PVC beam. The extendable rods are set up inside the four holes in advance. The performance of the sensors in terms of different inclination angle of rods are to be observed as different loads are applied to the center of the beam.

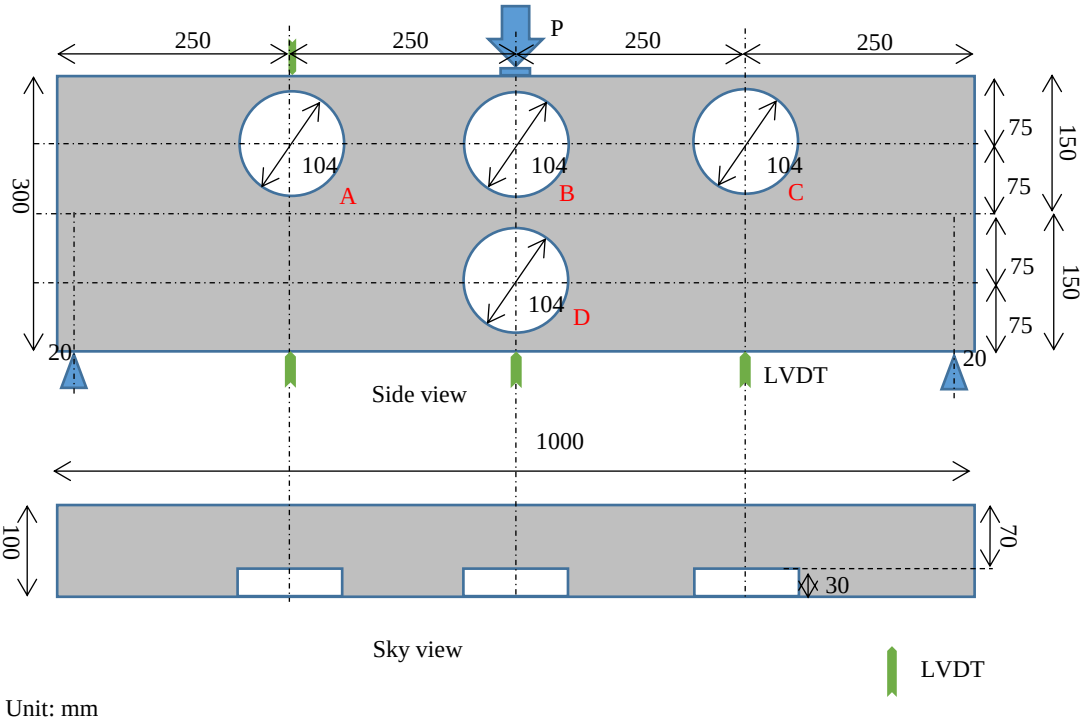

Figure 6.34 Experimental setup

6.7.3 Investigation of the size of circular ring

An assumption is made in this chapter that the circular ring is deformed to be elliptical under the condition of homogeneous deformation. It is not always the homogeneous deformation in a real loaded structure. As is known that the area of the heterogeneous deformation can be subdivided into several domains where are homogeneous. Therefore, it is of importance to determine the size of the domain and the circle. Furthermore, it is necessary to verify the feasibility of sensor in the other case that the circle is deformed to be similar to an ellipse.

6.7.4 Upgraded sensor for visualization of principal strain in 3D

The sample of sensor is possible to visualize the direction of principal strain in plane automatically. The aim of next research is to make a sensor capable of visualizing the principal strain including the scale and direction. Finally, a terminal sensor is pursued to visualize the principal strain in 3-demensions. An image of the sensor can be drawn that the extendable rod works inside a perfect sphere which can be set up in a structure.

6.8 Conclusions

A simple sensor is proposed to visualize the direction of principal strain in plane automatically. The mechanism of the sensor is clarified mainly on the assumption that the circle is deformed to be elliptical under the condition of homogeneous deformation. Directions of principal strains coincide with those of the longest and shortest axes of the ellipse. The feature of the sensor lies in that it measures the deformation not based on two discrete points of the object but the deformation in a circular domain. The main factors affecting the sensitivity and accuracy of the visualization are discussed. It is found the accuracy of visualization of the direction of principal strain is dependent on the effect of the weight of rod. The reduction of the weight of rod is a most possible approach to improve the sensitivity and accuracy of the sensor. The uniaxial compression tests were conducted to verify the possibility of the sensor for visualization of direction of principal strain. The sensitivity of the sensor was investigated experimentally as well. It shows that the sensor can work effectively to visualize the direction of principal strain as expected. Finally, the future work is introduced briefly to improve the sensor so that it can be more effective in practical use.

References for Chapter 6

1. Vaughan John: Application of *B* & *K* equipment to strain measurements, Brüel & Kjaer, 1975
2. Kersey Alan D., Davis Michael A., Patrick Heather J., LeBlanc Michel and Koo K. P.: Fiber Grating Sensors, *Journal of Lightwave Technology*, Vol.15(8), pp.1442-1463, 1997
3. Hill Kenneth O. and Meltz Gerald: Fiber Bragg Grating technology fundamentals and overview, *Journal of Lightwave Technology*, Vol. 15(8), pp. 1263-1276, 1997
4. Song Minho , Lee Sang Bae, Choi Sang Sam and Lee Byoungho: Simultaneous measurement of temperature and strain using two Fiber Bragg Gratings embedded in a glass tube, *Optical Fiber Technology*, Vol.3(2), pp.194-196, 1997
5. Majumder Mousumi, Gangopadhyay Tarun Kumar, Chakraborty Ashim Kumar and Dasgupta Kamal, Bhattacharya D.K.: Fibre Bragg gratings in structural health monitoring—present status and applications, *Sensors and Actuators A: Physical*, Vol.147(1), pp.150–164, 2008
6. Pereira G., McGugan M., Mikkelsen L.P.: Method for independent strain and temperature measurement in polymeric tensile test specimen using embedded FBG sensors, *Polymer Testing*, Vol.50, pp.125-134, 2016
7. Durelli A. J., Parks V. J.: Moiré analysis of strain, *Prentice Hall, Inc.*, New York, NY, 1970
8. Esmaeili Shamsedin, Rasouli Saifollah, Sobouti Farhad and Esmaeili Samodin: A moiré micro strain gauge, *Optics Communications*, Vol.285 pp.2243–2246, 2012
9. Bruck H. A., McNei S. R., Sutton M. A. and Peters W. H.: Digital image correlation using Newton-Raphson method of partial differential correction, *Experimental Mechanics*, Vol.29(3), pp.261–267. 1989
10. Cloud Gary: Optical methods of engineering analysis, *Cambridge University Press*, 1998
11. Hamada Shigeru, Fujisawa Tomoya, Koyama Motomichi, Koga Norimitsu, Nakada Nobuo, Tsuchiyama Toshihiro, Ueda Masaharu and Noguchi Hiroshi: Strain mapping with high spatial resolution across a wide observation range by digital image correlation on plastic replicas, *Materials Characterization*, Vol.98, pp.140–146, 2014
12. Hild F. and Roux S.: Digital Image Correlation: From displacement measurement to identification of elastic properties – A review, strain, Vol.42(2), pp. 69–80, 2006
13. Ramsay John G. and Huber Martin I.: The techniques of modern structural geology, Volume 1: Strian analysis, *Academic Press, Inc.*, 1983
14. Lisle R. J.: Geological Strain Analysis: A manual for the R_f/φ method, *Pergamon*

Press, 1985

15. Akutagawa Shinichi and Zhang Haihua: A system for visualization of principal strain, Patent: NO. KP16-004, *Japan Patent Office*, July, 2016 (Accepted)

CHAPTER 7: CONCLUSIONS AND FUTURE TASKS

7.1 Conclusions

This thesis introduces four simple mechanical methods for monitoring of deformations in structures based on the concept of On-Site Visualization. It focus on two essential aspects of monitoring, including sensing the deformation and visualization of the measured results. Both the load-induced deformation and thermal deformation are dealt with in the research. These methods are presented in the order of capacity of magnitude of the minimum visualized displacements. There is another clue in the arrangement of the thesis. The deformations are described by these methods in the form of relative displacement between two points, the total displacement along a length and a regional change in shape.

A notable feature is that the methods are able to work without consuming electric energy. Since the deformations are detected firstly by mechanical structures, which makes the monitoring reliable even in a harsh environment during construction. On the other hand, because the structure is simple and the common materials are used in these method, the cost can be reduced greatly compared with those utilizing electronic components. The measured results are visualized in the form of movement of indicator or changed images.

Generally, the accuracy of the mechanical methods is determined mainly by the function of sensing. The precision of the monitoring by these methods are affected by the resolution of the reference scales for visualization, the condition of environment, the observers' experiences and so on.

Most important of all, the mechanical methods enable the workers and engineers on site to "see" the safety state of structures directly during constructions, by which the potential danger can be identified in an early stage. In addition, since the methods cost at a relatively low level, which makes it possible to monitor more objects within a limited budget. The methods based on OSV are expected to improve the safety management during construction and in-service period.

The contents and conclusions in each chapter are summarized as follows:

Chapter 1 describes the background and objectives of this research. A brief history of research of On-Site Visualization is introduced. The related devices for measurement of deformations are reviewed.

In Chapter 2, the basic types of deformation of structures under the condition of loadings are analyzed to give a simple relationship between the deformation and displacement. The concept of strain ellipse is derived on condition of homogeneous deformation. The primary mechanical structures used to measure the displacement are also investigated, some of which are incorporated in this research.

In Chapter 3, a mechanical method is proposed to visualize the relative displacement between two discrete points on the surface of structure. A pulley is used to transform the linear displacement to the movement of rotation through the thread connecting the two measured points. The material of the thread needs to be stiff in tension and flexible in bending. A triangular flag attached on one side of the pulley can have the same rotation as the pulley so that the displacement can be read out directly from a reference plastic board. The diameter of the pulley determines the sensitivity of the measurement with respect to displacement. The mechanism of this method is described and the main influence factors of error are also analyzed based on results of the laboratory test. The field experiments were carried out in a NATM construction project to verify the feasibility of this method. It is shown that the sensors incorporating this method were able to visualize the deformations during construction at an acceptable accuracy. Therefore, the safety management of construction is possible to be improved by using this method.

Chapter 4 introduces an optical method to visualize the small displacement with a resolution of about 0.02mm. The optical level is utilized to magnify small displacement. Firstly, the small linear displacement is transformed to the rotational angle by a pulley or pinion-rack system. So an accurate relationship between displacement and angle can be established. Then, the angle is visualized and estimated by the shift of image reflected from a rectangular mirror. As a result, the deformation can be visualized by the image reflected from a mirror. Despite the fact that the deformation is deduced from the image seen by naked eyes, a displacement of as small as 0.1mm is able to be observed by this method. The factors influencing the accuracy and precision of visualization are discussed. The optical method has the potential to apply to the long term monitoring of the deformation of the infrastructures outdoors.

In Chapter 5, the feature of thermal deformation is analyzed comparing with the load-induced deformation. In view of the condition of a beam with both ends fixed, an indirect method is introduced to visualize the thermal deformation so that the corresponding thermal stress can be estimated accordingly. Two same beam are overlapped in the same environment. One is fixed at both ends. The other is set up on top of the first one, with

one end fixed with first beam and another end free. The thermal deformation (difference of the length of two beams) is visualized by a thin bar which is sandwiched between the two beams. That is, the deformation is transformed to the rotation of the bar and its value can be read from the reference board. Since the bar is very thin with a diameter of 1mm, a thermal elongation can be visualized with an accuracy of 0.05mm. The proper friction between the beam and the bar is required to assure there is no slide but the rotation of bar. The laboratory experiment indicates the feasibility to monitor the thermal deformation. The bar-beam sandwiched system also applies to monitor the small deformation in structures, such as the crack.

In Chapter 6, different from the conventional measurement of displacement between two discrete points, a simple sensor is proposed to monitor the regional deformation so that the direction of principal strain in-plane can be visualized automatically. The mechanism of the sensor is described on the assumption that a circle in structure is always deformed to be an ellipse under the condition of homogeneous deformation. Directions of principal strains coincide with those of the longest and shortest axes of the ellipse. The ring, which performs as the initial standard circle, has the rail track in the inner surface so that an extendable rod is able to rotate inside the ring along the rail. During deformation the extendable rod would be mobilized to rotate due to the unbalanced moment and stop at the positon of the major axis of the ellipse where the equilibrium can be regained. Therefore, the direction of one of the principal strains during deformation can be visualized by the status of the rod. The main factors affecting the accuracy and sensitivity of visualization are analyzed. It is found that the reduction of the weight of rod is a very effective approach to improve the sensitivity and accuracy of the sensor. The feasibility of this method to visualize the direction of principal strain is verified by the fundamental experiments. Finally, the future work in the second stage of the research is presented.

7.2 Future Tasks

7.2.1 Improvement of the mechanical sensors

The research work is an important part of the 3rd phase of the development of On-Site Visualization. It aims to provide the construction with cost-effective sensors to monitor different kinds of deformation in real-time, so that the safety management can be improved. Firstly, the methods presented in the thesis are mostly the proof-of-concept. The field experiments are to be continued to determine proper materials and sizes of the sensors which incorporate the ideas of this thesis. Secondly, because the reference scale or color board has much effect on the precision of visualization, it is necessary to

investigate the allowable deformation in different structures so that the color schemes can be correctly established. Finally, the deformation is visualized ignoring the time effect. Sometimes, the rate of deformation is also another parameter to take into account when evaluating the state of deformation in structures. It is a great challenge to add such the function in the sensor that not only the magnitude of the deformation but the rate of deformation can be visualized.

7.2.2 Determination system for OSV application

The OSV devices have been applied in the construction field to monitoring the deformation, inclination, stress of structures and so on. It is proved that the application of OSV can improve the safety management during construction. The concept and effect of OSV have been accepted by the users. In order to evaluate the OSV performance in the construction, Izumi C. suggested an average score system for performance analysis, in terms of index of functionality, visibility and the number of monitored points. There is still a need of an evaluation algorithm to determine the use of OSV devices for monitoring in the planning stage, including what to monitor and how many to monitor. The basic principle when constructing the simulation model lies in that the less cost of OSV monitoring should introduce the maximum achievement in the management of the construction.

7.2.3 Training program incorporating OSV

The performance of OSV in the construction can be efficient only if all the engineers and workers are involved in the monitoring. The development of technologies, application, and usage are dispensable for safety management. The absence of people in the monitoring, especially the engineers and workers, is not permitted. The training programs should be made to enable the workers and engineers onsite to make use of the OSV devices. It is believed that the application of OSV would play a more and more important role in the safety management of constructions in future.

Doctor Thesis, Kobe University

“Development of Mechanical Technologies for Sensing and Visualizing Deformations in Structures”, 113 pages

Submitted on Jan. 20th, 2017

The date of publication is printed in cover of repository version published in Kobe University Repository Kernel.